ABSTRACT

Title of Dissertation: QUASI-PHASEMATCHED ACCELERATION OF ELECTRONS IN A DENSITY MODULATED PLASMA WAVEGUIDE

Sung Jun Yoon, Doctor of Philosophy, 2014

Directed By: Professor Howard M. Milchberg
Department of Electrical and Computer Engineering

Two quasi-phasematching schemes are proposed for efficient acceleration of electrons to relativistic energies using moderate intensity laser pulses. In the first scheme, Direct Laser Acceleration (DLA) in a corrugated plasma waveguide is proposed for acceleration of relativistic electrons with sub-terawatt laser systems, using the laser field directly as the accelerating field. The second scheme uses the fact that a plasma wakefield generated by an intense guided pulse in a corrugated plasma waveguide can accelerate relativistic electrons significantly beyond the well-known dephasing limit. In each case, particle-in-cell (PIC) simulations are used to validate the acceleration concept, demonstrating linear acceleration by either the phase matched laser field or phase-matched wakefield. In the phase matched wakefield case, theory and PIC simulations demonstrate a significant increase in energy gain compared to the standard laser wakefield acceleration (LWFA) scheme.

Corrugated plasma waveguides can be generated by the interaction between an ionizing laser pulse and an atomic cluster flow interrupted by an array of thin wires,. When the collisional mean free path of the clusters is greater than the wire diameter, shadows of the periodically located wires are imparted on the cluster flow, leading to the production of axially modulated plasma waveguides after laser heating of the flow. This occurs when the population ratio of clusters to monomers in the gas is high. At other limit, dominated by gas monomer flow, shock waves generated off the wires by the supersonic gas flow disrupts modulated waveguide generation.

Lastly, we experimentally demonstrate LWFA with ionization injection in a N^{5+} plasma waveguide. It is first shown that the plasma waveguide is almost completely composed of He-like nitrogen (N^{5+}). It is then shown that intense pulse channeling in the plasma waveguide drives stronger wakefields, while the ionization injection process is critical to lowering the laser intensity threshold for self-trapping.

QUASI-PHASEMATCHED ACCELERATION OF ELECTRONS IN A DENSITY MODULATED PLASMA WAVEGUIDE.

By

Sung Jun Yoon

Dissertation submitted to the Faculty of the Graduate School of the
University of Maryland, College Park, in partial fulfillment
of the requirements for the degree of
Doctor of Philosophy
2014

Advisory Committee:
Professor Howard M. Milchberg, Chair
Professor Phillip Sprangle
Professor Julius Goldhar
Dr. John P. Palastro
Professor Konstantinos D. Papadopoulos

Dedication

To God whom I love

Acknowledgements

I confess that this work wouldn't be possible without these people I list below. It was my great privilege to live and work with these great people. First of all, I would like to thank Prof. Howard Milchberg. He is a great mentor not only in science, but also in life. He showed me a great example of a good scientist. I learned the most valuable lessons from him.

I also would like to thank Dr. John Palastro for his guidance in theory and simulations. A lot of my work wouldn't be possible without him. I had so much fun working with him. I am grateful to Dr. Brian Layer and Dr. Yu-hsin Chen, senior graduate students when I first joined the group. They taught me everything about experiments with great patience. I want to thank my fellow students: Jennifer Elle, Andy Goers, and George Hine. We shared many difficult and joyful moments together in the lab. I highly recognize their scientific insights and hard work. I credit Dr. Daniel Gordon for letting me use TurboWAVE and answering all my questions. I am indebted to all the people in the small lab, Dr. Jared Wahlstrand, Sina Zahedpour, Eric Rosenthal, and Nihal Jhajj. I also recognize our undergraduates, Reuven Birnbaum and Linus Feder, for assistance.

Finally, I would like to thank my family. I express my gratitude to my parents for their sacrificial support. Last, but not least, I have to say thank you to my loving wife, Ji Young, for her encouragements and supports, and my daughter, Danielle, for giving me happiness and strength to finish this journey.

Table of Contents

List of Tables

List of Figures

Chapter 1: Introduction

1.1 Charged particle accelerators

1.1.1. Background

During the last century, charged particle accelerators have significantly increased the energy of accelerated particles and in acceleration efficiency [1, 2]. Early designs of accelerators used electrostatic fields to accelerate charged particles and have remained the most widely used type until the present. Charged particles were accelerated between two electrically biased plates, cathode and anode, using high voltages (>kV). The accelerating fields were limited to MeV due to difficulties of producing steady high voltages and high voltage breakdown of the plates. Radio frequency (RF) fields were proposed as an accelerating field to circumvent this limit [3].

There are two main types of RF accelerators, linear accelerators (LINAC) and cyclic accelerators. A LINAC accelerates charged particles along a straight trajectory. The first version of LINAC [4], illustrated in Fig.1.1(a), took a simple form based on a series of metal drift tubes with lengths ($L = \beta\frac{\lambda}{2}$), where L is the length of a tube, λ is the wavelength of the RF field, and β is the ratio of the particle velocity to c. Alternating tubes connected to the RF source have the same polarity. When a charged particle passes through the gap between two neighboring tubes, an electric field with the right polarity is applied between the tubes and accelerates the particle. When

particles are inside the tubes, there is no accelerating field, and particles just drift in the tubes. The particle energy increases continuously as it passes through the drift tubes. However, since the drift tubes act as antennas, there is a loss of RF power through radiation.

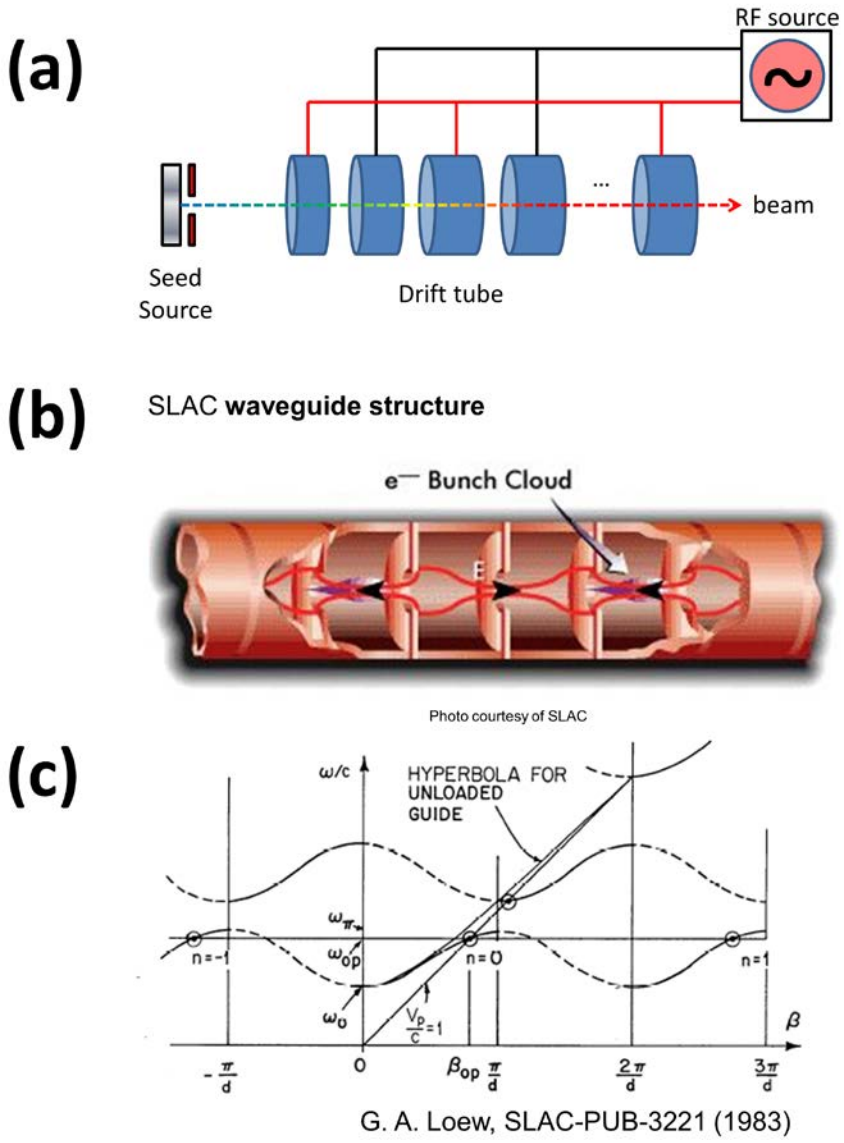

Figure 1.1.(a) Schematic of a drift tube linear accelerator. Each alternating tube is connected in the same polarity from the RF source. Seed source generates charged particles to be accelerated. (b) Cut-view of the copper waveguide, accelerating structure in SLAC, U.S.A. Copper waveguides guide the accelerating RF field, and the periodically loaded disks match the phase velocity of the wave to the particle velocity. (c) Brillouin diagram for a disk-loaded waveguide [5]

Figure 1.1(b) shows the cylindrically symmetric copper waveguide structure with periodically loaded copper disks of the Stanford Linear Accelerator (SLAC). SLAC uses a different scheme from the drift tube LINAC described above. The simplest model of the structure depicted in Fig.1.1(b) is a chain of resonant cavities, where each resonator is coupled to the next through the holes on the periodically loaded disk plates. In the limit that the coupling between the resonators is weak (the hole size on the plate is small), individual RF sources are required to drive each individual cavity, because RF waves cannot propagate to the next resonators. In that case, the phase of the RF sources can be synchronized in a way that the accelerated particle in a resonator enters the next resonator at the accelerating phase of RF field. However, In SLAC, the LINAC is a chain of strongly coupled resonant cavities, because the hole sizes in the copper disks are big compared to the disk size. Each copper disk partially reflects the guided microwave in the cylindrical copper waveguide, and the combination of the forward propagating field and the reflected field can form a standing wave, a resonant condition, if the longitudinal wavenumber, β, of the RF field meets $\beta = n\pi/d$, where d is the periodicity of the copper disks and n is an integer number. The dispersion relation of the disk loaded cylindrical copper waveguide is shown in Fig.1.1(c). As β increases from zero, the dispersion curve initially follows the hyperbolic curve of the unloaded waveguide. However, as β approaches the first resonant condition, π/d, the dispersion curve flattens, providing a crossing point with the $\frac{v_p}{c} = 1$ line. SLAC has multiple stages of these accelerating waveguides to provide different phase velocities of the RF field for

electrons at different ranges of speed. A travelling TM mode microwave is guided in each waveguide and accelerates electrons with its longitudinal component of the electric field on axis. SLAC accelerates electrons up to 50GeV with this structure. However, the maximum acceleration gradient cannot be greater than 10MV/m due to the breakdown of the structure; the total accelerator length has to be about 2 miles long to achieve electron acceleration to 50GeV.

Cyclic accelerators accelerate charged particles with an RF electric field along a circular trajectory. One example is the cyclotron. The typical design of a cyclotron is shown in Fig.1.2. A flat circular vacuum chamber is enclosed by two magnets, setting up a uniform static magnetic field perpendicular to the plane of the "D" shaped electrodes, called dees.

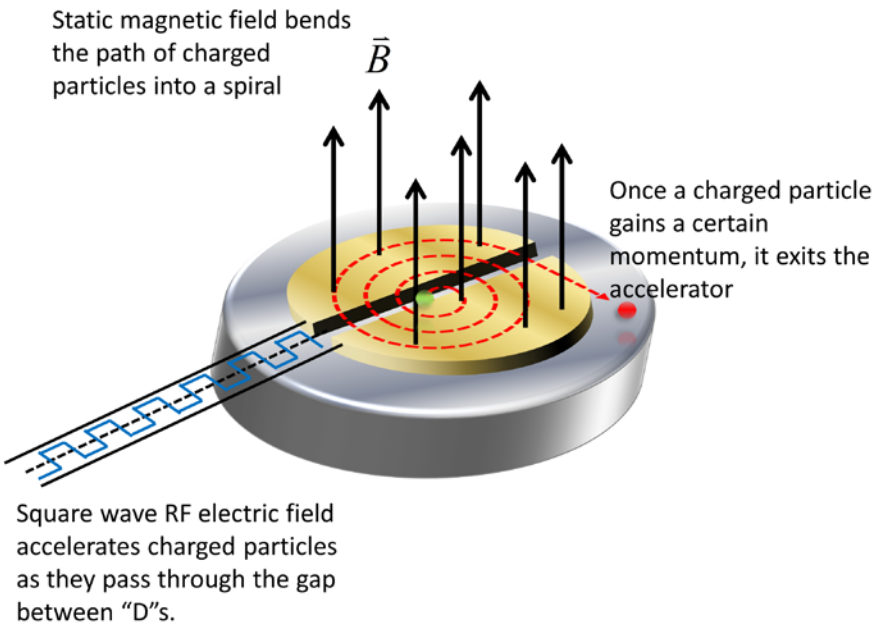

Figure 1.2. Schematic of a cyclotron. The silver metallic plate is a magnet, and there is another magnet with opposite polarity, omitted in this figure. Yellow "D" shaped plates are the electrodes. The square wave RF field is applied across the electrodes. Charged particles (green) are injected near the center of the chamber, and accelerate along the spiral trajectory.

Charged particles are injected near the center of the chamber at the gap between the two dees. An applied RF electric field accelerates the charged particles in the gap between the dees. The particle then passes into the dee where the electric field is zero. With each pass through the gap, the electron gains additional energy. Due to the uniform and static magnetic field in the chamber, particles move in a circular motion with a radius

$$r = \frac{mv}{|q|B} \qquad (1.1),$$

where $m = \gamma m_0$ is the relativistic particle mass, v is the particle velocity, q is the charge of the particle, and B is the magnetic field. The time required for a particle to traverse a semi-circle of radius r is $\tau = \frac{\pi r}{v} = \frac{\pi m}{|q|B}$, invariant as long as the particle is non-relativistic ($m \approx m_0$). Thus, the angular frequency of the RF field is

$$\omega_{rf} = \frac{|q|B}{m} \qquad (1.2).$$

Every time the particle passes through the gap, the velocity and orbit radius increase. Given a magnet with an arbitrary radius, the maximum energy gain is limited by the loss of synchronism between the accelerated particle and the accelerating field due to the relativistic mass increase of the particle.

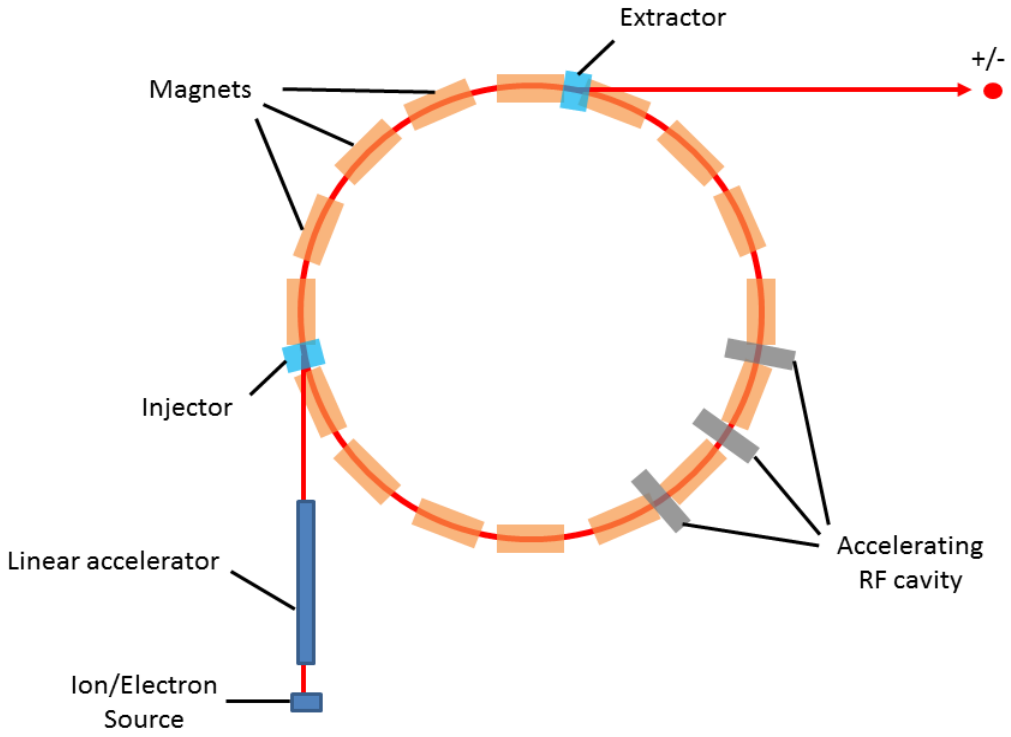

Figure 1.3.Schematic of a synchrotron. The red line is the charged particle trajectory. The velocity of the charged particles is initially boosted by a linear accelerator. The yellow boxes are magnets that bend the particle path. The injector and extractor are electro-magnets that are turned on to inject or extract charged particles from the orbit. Energy gain occurs only in the accelerating RF cavities, marked with gray box.

The synchrotron has been developed for higher energy particle acceleration, because the RF frequency of the accelerating field can be almost invariant once a particle reaches a velocity close to c and travels a certain radius at a constant period. In a synchrotron, the trajectory of the particle is a circle instead of a spiral as in a cyclotron. By using a circular rather than spiral trajectory, a magnetic field is only required along the beam trajectory to confine the particles to the orbit. Figure 1.3 is a schematic of a typical synchrotron. Acceleration occurs over small sections of the orbit by the electric fields in resonant cavities. The angular frequency of the RF field

in the synchrotron is $\omega_{synchrotron} = v / R$, where R is the radius of orbit. In the relativistic regime, it will converge to c / R as the particle velocity, v, approaches c. The magnetic field B is variable to keep the particles in the orbit according to Eq.(1.1) as their momentum increases. An auxiliary accelerator, usually an electrostatic accelerator or a linear accelerator, is used to inject the particles into the synchrotron ring with an initial energy large enough to keep the RF frequency in an operational range.

1.1.2. Relativistic Dynamics

When the energy of a particle approaches its rest mass (e.g. 511keV for electrons, 938.27 MeV for protons), it approaches the speed of light in a vacuum ($c = 2.99792 \times 10^8 m/s$), and the particle can be considered 'relativistic'. When designing a particle accelerator that accelerates a particle to a speed close to *c*, the relativistic effect must be taken into account.

The energy and momentum of a particle are $E = mc^2 = \frac{m_0 c^2}{\sqrt{1 - v^2 / c^2}} = \gamma m_0 c^2$ and $p = mc = \frac{m_0 c}{\sqrt{1 - v^2 / c^2}} = \gamma m_0 c$ respectively, where m_0 is the rest mass, $m = \gamma m_0$ is the relativistic mass, $\gamma = \frac{1}{\sqrt{1 - v^2 / c^2}} = \frac{1}{\sqrt{1 - \beta^2}}$ is the Lorentz factor, v is the velocity, and $\beta = \frac{v}{c}$ is the ratio v to the speed of light, c. These two expressions for energy and momentum can be combined to give $E^2 = (pc)^2 + m_0^2 c^4$. The force on the charged particles from the electric and magnetic field is governed by the Lorentz force,

$$\vec{F} = q\left(\vec{E} + \frac{\vec{v}}{c} \times \vec{B} \right) \qquad (1.3).$$

The equation of motion in relativistic mechanics is

$$\vec{F} = \frac{d\vec{P}}{dt} = m_0 \frac{d\left(\gamma \vec{v}\right)}{dt} = m_0 \gamma \frac{d\vec{v}}{dt} + m_0 \vec{v} \frac{d\gamma}{dt} \qquad (1.4).$$

Eq.(1.3) shows that a force, $\vec{F}$, does not only change the velocity, $\vec{v}$, but also changes γ, depending on $\vec{v}$. The 2nd term on the right hand side of Eq. (1.4), $m_0 \vec{v} \frac{d\gamma}{dt}$, can be further transformed to the time derivative of velocity, $\gamma^3 m_0 \vec{v} \frac{|v|}{c^2} \frac{d|v|}{dt}$. If $\vec{F}$ is perpendicular to $\vec{v}$, Eq.(1.4) is reduced to $\vec{F} = \gamma m_0 \frac{d\vec{v}}{dt}$, whereas if $\vec{F}$ is parallel to $\vec{v}$, it is reduced to $\vec{F} = \gamma^3 m_0 \frac{d\vec{v}}{dt}$. In the relativistic limit ($\gamma >> 1$), only the transverse force $\vec{F} \perp \vec{v}$ can significantly change the velocity of the particle. However, small changes in the axial velocity can still create large changes in momentum and energy.

1.2. Relativistic laser plasma interaction

1.2.1 Background

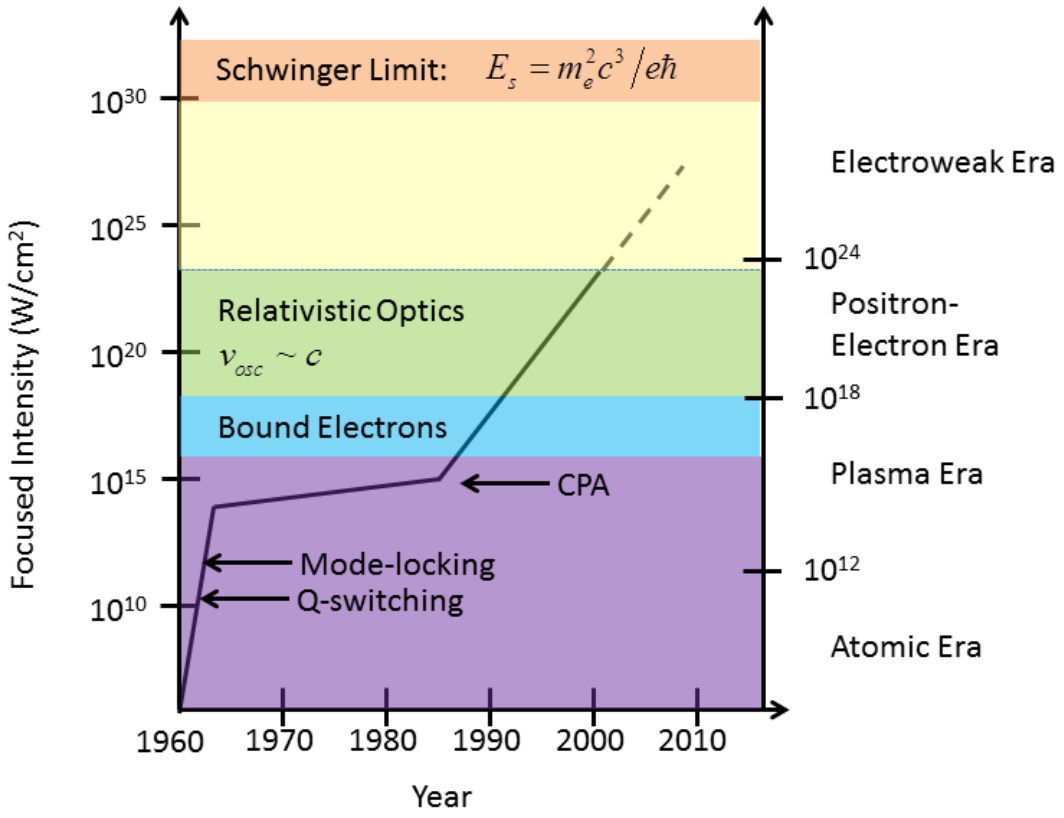

Figure 1.4.History of high intensity laser development and related physical regime at each intensity level.[6]

Many scientific advancements can be attributed to the invention of the laser [7]. Figure 1.4 illustrates the history of high intensity laser developments and the physical phenomena accessible at each intensity level. The way to achieve high peak power has been to reduce the laser pulse duration. The nanosecond pulse length regime was achieved by Q switching [8], and the picosecond and femtosecond laser pulse durations were achieved by mode-locking technologies [9]. The recent

continuous increase in achievable laser intensity has been enabled by Chirped Pulse Amplification (CPA) [10].

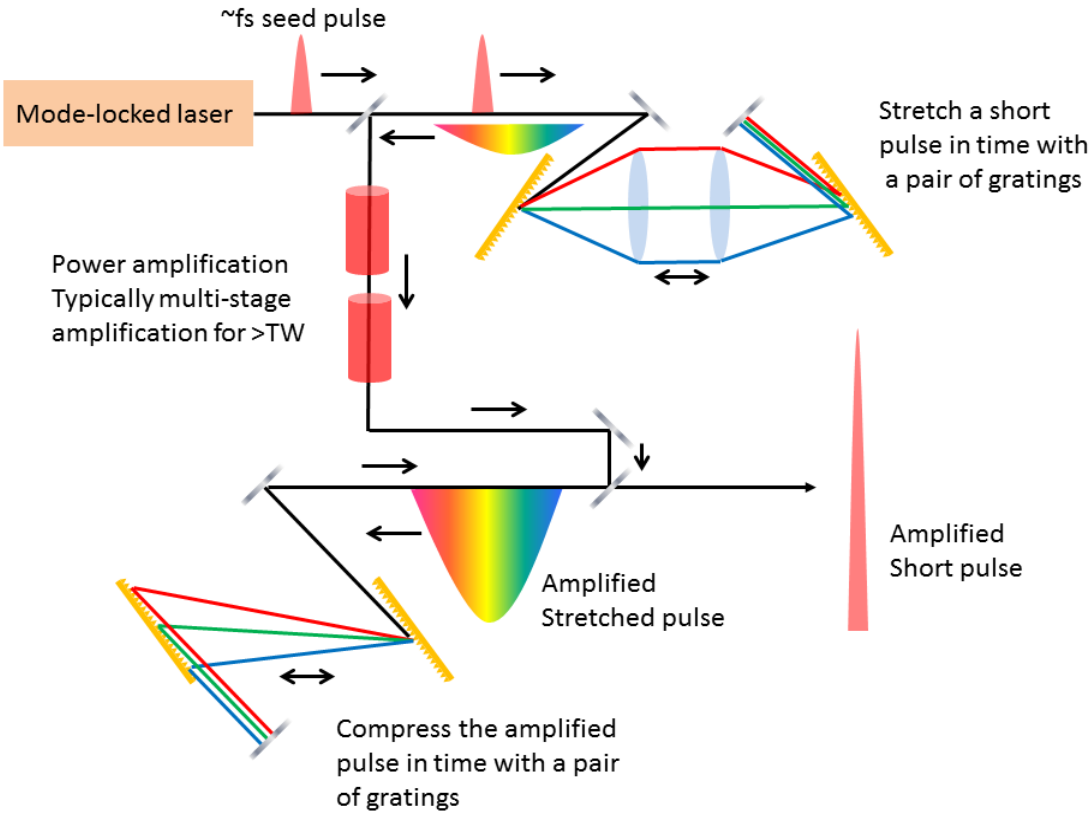

Figure 1.5. Schematic of the chirped pulse amplification (CPA) system. Initially, a short and low power laser pulse is stretched in time by a pair of gratings. Then, it goes through amplification steps. An amplified pulse is compressed back to a short duration by the reverse process of the stretcher.

CPA is designed to amplify femtosecond level laser pulses to extreme peak powers (>10GW). As illustrated in Fig. 1.5, a seed pulse from a mode-locked laser oscillator enters the stretcher, which is composed of a pair of gratings. Since different frequency components travel different path lengths, after spatial beam combination, the output beam of the stretcher is temporally chirped, and the pulse length increases from tens of femtoseconds to hundreds of picoseconds. This temporal stretching enables further amplification of the laser energy, since the peak intensity becomes

less than the damage threshold of the laser optics. The amplification occurs in multiple stages to achieve TW or greater level peak powers. After amplification, the laser pulse undergoes temporal compression by going through the reverse process of stretching. The compressor is also composed of a pair of gratings. For TW level CPA laser systems, Ti:Sapphire has been the most popular gain medium, since it has a large gain spectral bandwidth (650~1100nm) and excellent thermal conductivity (33W/mK). State-of-the-art high energy CPA Ti:Sapphire laser systems can produce laser pulses with 1PW peak power in a 30 fs pulse [11], focusable to intensity of $\sim 10^{21} W \cdot cm^{-2}$. With our lab's 20TW CPA Ti:Sapphire laser system, an intensity $> \sim 10^{19} W \cdot cm^{-2}$ can be reached.

At these intensities, the medium that the laser pulse primarily interacts with is in a plasma state. The ionization of an atom occurs when a bound electron in an atom is freed by the laser field. There are several regimes for laser-driven ionization. First, a single photon with high enough energy ($\hbar\omega$) is absorbed to promote an electron from a bound state to a free continuum. This is called single photon ionization. This occurs when the photon energy, $\hbar\omega$, exceeds the ionization energy, E_{ion}, of the atom or ion.

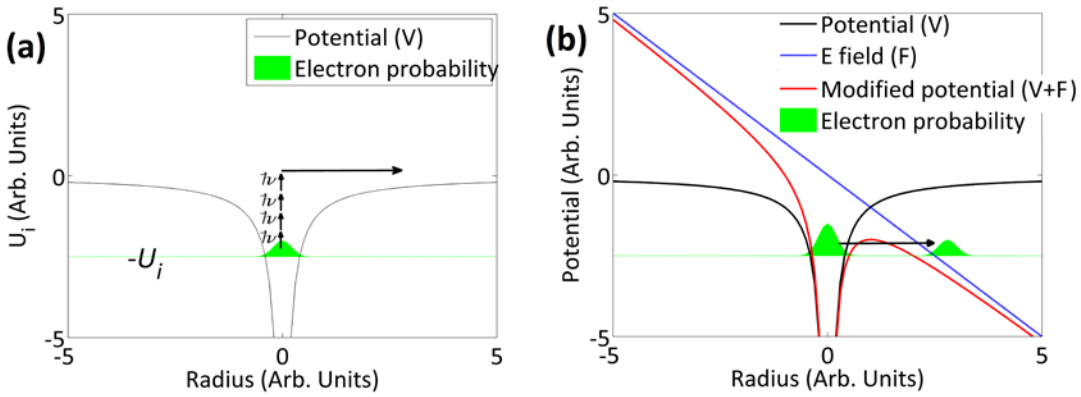

Figure 1.6. (a) Multiphoton ionization process (b) Tunnel ionization process

Even though the photon energy may be less than the ionization energy, multiple photons can promote a bound electron to the free continuum. This is called multi-photon ionization (MPI)[12]. The n-photon ionization rate is $w_n = \sigma_n I_L^n$, where σ_n is the cross section of n-photon absorption and I_L is the laser intensity.

As the intensity increases, the laser field starts to strongly distort the atomic potential. Tunneling ionization (TI) occurs when the laser field modifies the potential enough that a bound electron can tunnel, with some probability, through the potential barrier [13]. With higher laser intensity, the Coulomb potential of an atom can be completely suppressed below the electron bound energy, so that the bound electrons freely escape over the potential barrier. This regime is called over-the-barrier ionization (OTBI) or barrier suppression ionization (BSI). The Keldysh parameter [13], $\gamma_K = \sqrt{U_i / 2U_p}$ delineates the ionization regime, where U_i is the ionization potential energy and U_p is the laser ponderomotive potential energy, given by

$U_p = \frac{e^2 E^2}{4 m_e \omega^2}$. The Keldysh parameter γ_K can also be interpreted as the ratio of the ionization time to the laser optical period. For $\gamma_K >> 1$, the average kinetic energy of electrons in the laser field is much less than the ionization potential energy, and the ionization time is much longer than the laser field period. MPI is the dominant ionization mechanism in this regime. For $\gamma_K < 1$, the averaged kinetic energy of the electrons in the field is comparable to or higher than the ionization energy, and the laser field can be considered static on the atomic time scale while the electron is still bound to the atom. TI is dominant in this regime. For $\gamma_K << 1$, OTBI (BSI) occurs during ionization. The critical intensity for OTBI can be expressed as

$$I_{OTBI} = \frac{c U_i^4}{128 \pi Z^2 e^6} \approx 4 \times 10^9 \left(U_i[eV]\right)^4 Z^{-2}\ W \cdot cm^{-2} \qquad (1.5),$$

where Z is the charge state of the resulting ion [14, 15].

Species	$U_i(eV)$	$I_{OTBI}(W \cdot cm^{-2})$
H	13.60	1.4×10^{14}
He	24.59	1.4×10^{15}
He^+	54.42	8.8×10^{15}
N	14.54	1.8×10^{14}
N^{4+}	97.89	1.5×10^{16}
N^{5+}	552.07	1.0×10^{19}
Ar	15.76	2.5×10^{14}
Ar^{8+}	422.45	1.6×10^{18}

Table 1.1. Examples of the ionization energy and critical intensity for OTBI. [16]

Table 1.1 shows a few examples of the ionization energy and critical intensity for OTBI. For laser intensity $>10^{15} W \cdot cm^{-2}$, the peak of the pulse will interact with plasma, since the ionization occurs at the far leading edge of the laser pulse upon passage through a gas. We note that particle collisions can also result in ionization. In this dissertation, collisional ionization is significant only for femtosecond and picosecond laser interaction with clusters (see chapter 4 and 5).

For the typical frequency and time scale of the short high power laser pulses of this dissertation, the plasma response is almost purely from electrons, neglecting the ion response, owing to the very small electron-ion mass ratio. The liberated electrons are pushed by the electromagnetic field of the laser pulse according to the Lorentz force in Eq. (1.3). The normalized wave vector $\vec{a}_0 = \frac{e\vec{A}}{m_e c^2}$ is the dimensionless amplitude of the laser field, where A is the vector potential of the field. When a_0~1, the electric field drives the electron's quiver momentum to $m_e c$. The $\frac{\vec{v}}{c} \times \vec{B}$ term in the Lorentz force gives rise to the nonlinear trajectory of the electrons with respect to the electric field. The time (optical cycle) averaged nonlinear force from the laser pulse acting on the electron is given by

$$\vec{F}_p = -\frac{e^2}{4m_e\omega^2}\nabla\left|\vec{E}\right|^2 \qquad (1.6)$$

and defined as the 'ponderomotive force', where ω is the angular frequency of the laser field. From Eq. (1.6) we see that the ponderomotive force, F_p, is proportional to ∇I, where I is the laser intensity. This force does not depend on the sign of a particle's charge. Upon the irradiation of a high intensity laser pulse, electrons in

plasma not only undergo fast oscillations in the laser electric field, but are also pushed away from the laser pulse, leaving a density depleted region right behind the laser pulse. The electron density oscillates after being displaced at the natural resonant frequency, or plasma frequency

$$\omega_p = \sqrt{\frac{4\pi n_e e^2}{\gamma m_e}} \qquad (1.7),$$

where n_e is the electron density, γ is the Lorentz factor, and m_e is the rest mass of the electron. The electrostatic field associated with the electron density wave is called the wakefield.

To understand the propagation of an electromagnetic wave in a medium, one has to consider its refractive index. From the Drude model [17], the dielectric function of plasma is $\varepsilon = 1 - \frac{\omega_p^2}{\omega^2}$, and the refractive index of the plasma becomes

$$n = \sqrt{1 - \frac{\omega_p^2}{\omega^2}} \qquad (1.8).$$

The dispersion relation of an electromagnetic wave in plasma is

$$\omega^2 = k^2 c^2 + \omega_p^2 \qquad (1.9).$$

From Eq. (1.9), we find the phase and group velocities of the wave $v_{ph} = \frac{c}{\sqrt{1 - \omega_p^2 / \omega^2}}$ and $v_g = c\sqrt{1 - \omega_p^2 / \omega^2}$ respectively

The nonlinear dynamics of free electrons in the relativistic regime, enabled by the development of high intensity laser pulses, has opened up exploration of many interesting physical phenomena. At relativistic intensities, the effective mass of an electron is increased due to its quiver motion in the electric field. This mass increase

results in a change in the refractive index as the plasma frequency changes as shown in Eq. (1.7). Due to the refractive index change over the transverse intensity profile, self-focusing occurs. Another nonlinear effect often found in the interaction between a relativistic laser pulse and a plasma is wakefield generation, discussed above with the ponderomotive force.

1.2.2. Relativistic Self-focusing

Self-focusing occurs when an intense electromagnetic field alters the refractive index of a medium. In the Kerr effect, the intensity-dependent index of refraction results from the nonlinear motion of atomic bound electrons at laser intensities less than the ionization threshold [18]. For a centrosymmetric medium, such as a monatomic gas, it can be shown that to leading order in the intensity, *I*, the refractive index of a material can be expressed as $n = n_0 + n_2 I$. Relativistic self-focusing (RSF) in plasma is analogous to Kerr induced self-focusing, except here the nonlinearity is provided by the relativistic quiver motion of the electron in its driving field. RSF is induced by the relativistic mass increase of the electron [19]. In a vacuum, a Gaussian beam is considered to be in focus only over the confocal parameter, 2 times the Rayleigh length: $z_R = \pi w_0^2 / \lambda$, where w_0 is the beam waist at focus and λ is the wavelength of the beam. When self-focusing occurs near the focus, the pulse can remain collimated and the high intensity, nonlinear interactions can be extended over many Rayleigh lengths. This continues until the laser energy depletes by driving plasma waves and the peak power becomes less than the critical power for self-focusing, P_{cr}, which we derive below.

The increase in relativistic mass modifies the refractive index of plasma according to Eq. (1.7) and (1.8). The relativistic mass factor can be described in terms of the laser amplitude, a_0, as $\gamma = \sqrt{1+a_0^2}$. For $\omega_p^2 << \omega^2$ and $a_0^2 << 1$, the refractive index of plasma in Eq.(1.8) can be approximated to $n \approx 1 - \frac{\omega_p^2}{2\omega^2} + \frac{\omega_p^2}{4\omega^2} a_0^2$. It can be rewritten in the form of n in the Kerr induced self-focusing expression as

$$n \approx 1 - \frac{\omega_p^2}{2\omega^2} + \frac{e^2\lambda^2\omega_p^2}{2\pi m_e^2 c^5 \omega^2} I = n_0 + n_2 I \qquad (1.10),$$

where $n_0 = 1 - \frac{\omega_p^2}{2\omega^2}$ and $n_2 = \frac{e^2\lambda^2\omega_p^2}{2\pi m_e^2 c^5 \omega^2}$. To maintain the laser focus over extended distances, RSF needs to balance diffraction. The peak power of a laser pulse should exceed the critical power to keep the laser in focus over the Rayleigh length by the RSF. The critical power for RSF is therefore

$$P_{cr} = \frac{m_e c^5 \omega^2}{e^2 \omega_p^2} \approx 17 \left(\frac{\omega}{\omega_p} \right)^2 GW \qquad (1.11).$$

P_{cr} is inversely proportional to the plasma density, n_e [19]. For example, P_{cr} is 4TW for a plasma density of $7 \times 10^{18} cm^{-3}$. Note that the refractive index change due to plasma density perturbation is not considered in Eq. (1.11).

As can be seen from Eq. (1.7) and (1.8), the refractive index also changes due to the density perturbation induced by the relativistic laser intensity. Since the region of depleted electron density has a higher refractive index, the transverse refractive index profile is capable of keeping the laser pulse focused. Density perturbations will be discussed in further detail in section 1.2.3.

Once RSF occurs, this nonlinear process generates a positive feedback loop on the laser pulse: the laser pulse modifies the refractive index, and the refractive index modifies the pulse propagation. Eventually the feedback loop stops when the laser energy is sufficiently depleted. If there is irregularity in the transverse intensity profile, RSF causes the beam profile instability to grow and the laser beam ends up with a fragmented profile due to multiple filamentation across the beam profile.

1.2.3. Wakefield generation

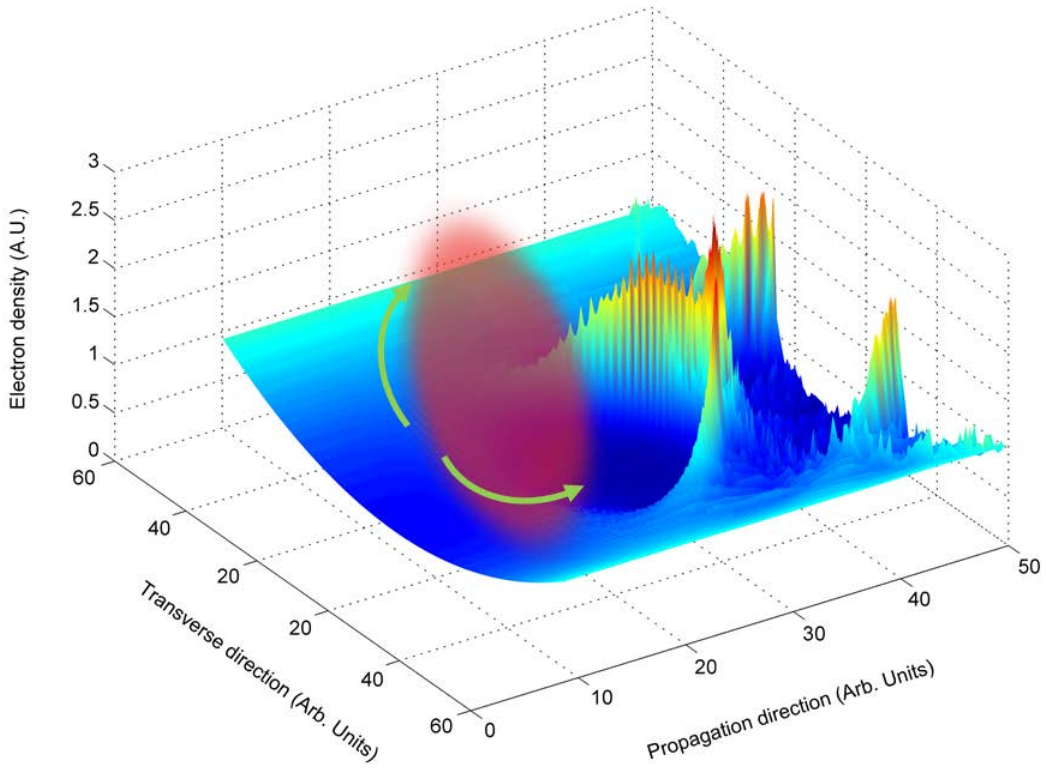

Figure 1.7. Diagram of laser wakefield generation. The red color illustrates the laser energy density. The green arrows show that electrons are pushed away from the laser pulse by the ponderomotive force. The colored surface plot is the electron density of plasma from a Particle-in-Cell simulation. The simulation was done with a typical set-up to drive the plasma wakefield in a plasma channel.

Plasma can support extremely large electrostatic fields associated with plasma waves. The electric field of a linear plasma wave takes a sinusoidal form. From the Poisson equation $\vec{\nabla}\cdot\vec{E} = 4\pi\left(n_0 - n_e\right)$, the maximum amplitude of the electric field can be approximated by substituting $\vec{\nabla}\cdot\vec{E}$ with $\left(\omega_p / c\right)E$ in the Poisson equation, giving the maximum field amplitude as $E_0 = m_e c\omega_p / e$ [20], which is the cold nonrelativistic wave breaking field. However, in the nonlinear plasma wave regime,

the field amplitude can exceed E_0 [21].

The ponderomotive force in Eq. (1.6) can be rewritten in terms of the normalized vector potential, a_0, in the weak field limit ($a_0^2 << 1$)

$$\vec{F}_p = -\left(m_e c^2 / 2\right)\nabla a_0^2 \qquad (1.12).$$

The plasma of interest is considered cold with an electron temperature of a few eV, and collisionless. The plasma density wave perturbed by the ponderomotive force of a laser pulse can then be described by the fluid equations

$$\text{Conservation of mass: } \frac{\partial n}{\partial t} + \vec{\nabla}\cdot\left(n\vec{u}\right) = 0 \qquad (1.13)$$

$$\text{Conservation of momentum: } \frac{\partial\left(n\vec{u}\right)}{\partial t} + \vec{u}\vec{\nabla}\cdot\left(n\vec{u}\right) + \vec{\nabla}p - \vec{f} = 0 \qquad (1.14)$$

$$\text{Equation of state: } p = nRT \qquad (1.15),$$

where n is the density of the flow, $\vec{u}$ is the velocity of flow, p is pressure, and $\vec{f}$ is external force imparted to the fluid. Solving equations (1.13)-(1.15) with perturbation theory, one gets wave equations for the linear wakefield excited by the ponderomotive force in Eq. (1.12),

$$\left(\frac{\partial^2}{\partial t^2} + \omega_p^2\right)\frac{\tilde{n}}{n_0} = \frac{c^2\nabla^2 a^2}{2} \qquad (1.16)$$

$$\left(\frac{\partial^2}{\partial t^2} + \omega_p^2\right)\phi = \frac{\omega_p^2 a^2}{2} \qquad (1.17),$$

where $n = n_0 + \tilde{n}$, $\phi = e\Phi / m_e c^2$ is the normalized electrostatic potential, and $a = e\left|\vec{A}\right| / m_e c^2$ is the normalized vector potential [22]. The solutions for the density perturbation and the electric field, E, of the wake are

$$\frac{\tilde{n}}{n_0} = \frac{c^2}{2\omega_p}\int_0^t dt' \sin\left[\omega_p\left(t-t'\right)\right]\nabla^2 a^2\left(r,t'\right) \qquad (1.18)$$

$$\frac{E}{E_0} = -\frac{c}{2}\int_0^t dt' \sin\left[\omega_p\left(t-t'\right)\right]\nabla a^2\left(r,t'\right) \qquad (1.19)$$

These solutions are valid in the quasi-static approximation, which assumes that the laser pulse evolves negligibly in the time it takes an electron to traverse it. Equations (1.18) and (1.19) imply that the wake generation will be most efficient when the axial size of the laser envelope is approximately the plasma wavelength $\lambda_p = \omega_p / c$.

In the 3D nonlinear regime ($a_0^2 \geq 1$), the analytic calculation becomes extremely complicated, and numerical methods are typically required, because the laser pulse evolves too quickly and the quasi-static approximation is no longer valid. Nevertheless, a nonlinear wakefield can be analytically approached in 1D with the quasi-static approximation. This aspect will not be discussed in this thesis, but a useful discussion can be found in [21]. Further details on numerical methods will be discussed in section 1.5 on particle-in-cell simulations.

1.3. Laser Wakefield Acceleration (LWFA)

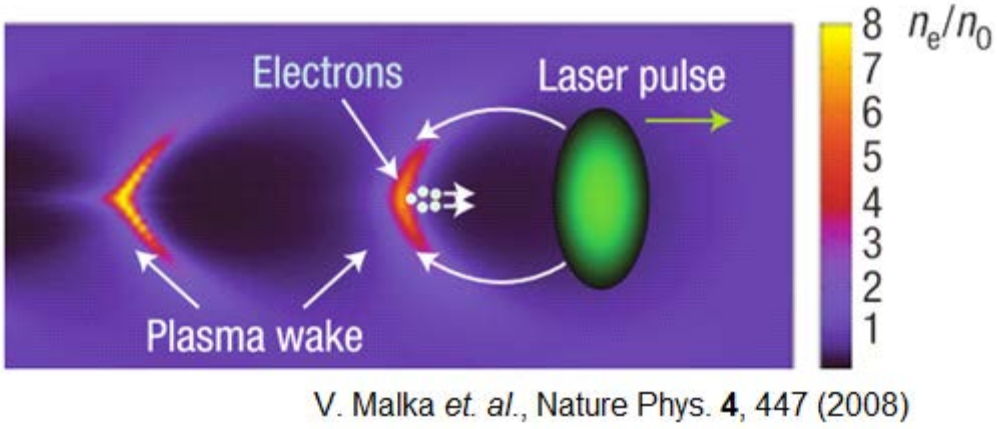

Figure 1.8. Schematic representation of laser wakefield acceleration (LWFA) with self-injection in a bubble regime. Electrons trapped in the wakefield are marked with white dots. The driving laser pulse is represented as green. [23]

A plasma wakefield can be used to accelerate electrons on a centimeter scale with an accelerating field gradient 3 orders higher than RF based accelerators; acceleration to GeV energies is possible in a centimeter. Due to the plasma wave's large accelerating gradient, electrons quickly become relativistic. In turn, the velocities of the accelerated electrons exceed the phase velocity (v_p) of the plasma wave [20]

$$v_p = c\left(1-\frac{\omega_p^2}{\omega^2}\right)^{1/2} \qquad (1.20)$$

The phase velocity of a linear plasma wakefield is equal to the group velocity ($v_{g,L}$) of the driving laser pulse. The accelerated electrons outrun the accelerating phase of the plasma wave, and start to be decelerated. This results in a maximum effective acceleration length or dephasing length

$$L_d = \frac{\lambda_p c}{2\left(c - v_p\right)} \approx \lambda_p \gamma_p^2 \qquad (1.21),$$

assuming $\gamma_p = \omega / \omega_p >> 1$ [24]. The maximum energy gain after a dephasing length is, approximately,

$$W_{\max} = eE_0 L_d \approx 2\pi \gamma_p^2 m_e c^2 \qquad (1.22).$$

In chapter 3, we propose that this energy gain limit due to the dephasing length can be overcome with an axial density modulated plasma waveguide, because periodic plasma density modulation can excite a spatial harmonic of plasma waves with a phase velocity matched to the electron velocity for continuous acceleration over the dephasing length. Generation of density modulated (corrugated) plasma waveguides is discussed in section 1.4.1.

1.3.1. Electron trapping

Self-injection of background electrons to the accelerating phase of the plasma wave occurs when the amplitude of the plasma wave reaches the wave breaking limit, typically requiring driving laser pulses with normalized vector potential $a_0 >> 1$. For laser systems with peak laser power less than a few tens of TW, these intensities are typically reached through the temporal pulse compression in the plasma wave [25] and RSF. However, these nonlinear processes are subject to change resulting from small variations in experimental conditions, thus generating unstable electron beam qualities. In addition, the plasma density has to be high enough to achieve the wave breaking at the early stage of acceleration, which also reduces the dephasing length

and the maximum achievable energy gain.

For these reasons, a few other schemes to control the injection of background electrons into the wake are introduced, involving multiple laser pulses [26-29] or tailored plasma density profiles [30-32]. Recently, ionization injection of high Z dopants was proposed and demonstrated to increase electron beam charge and lower the intensity threshold for electron trapping [33-37]. In previous ionization injection experiments, the concentration of the high Z dopants could not exceed 10% of the total mass density due to the laser pulse refraction by the additional plasma density created by ionization of dopants. To overcome this laser refraction issue due to the extra ionization of dopants, we studied ionization injection from a pre-ionized N^{5+} plasma waveguide, which will be presented in chapter 5.

1.3.2. LWFA in plasma channels

For maximum energy gain in the standard LWFA, the driving laser pulse must stay in focus over the dephasing length. Relativistic self-focusing is often used for this purpose [38, 39]. However, as the maximum energy gain is inversely proportional to the plasma density according to Eq. (1.22), the plasma density needs to be lowered for higher energy gain. In turn, the laser power also has to be increased to meet the increased critical power for RSF in Eq. (1.11) at lower plasma density. Recently, Petawatt-class lasers have been used for LWFA, reporting energy gains >2 GeV in $\sim 10^{17}\, cm^{-3}$ plasmas [40, 41].

Alternatively, plasma waveguides can be used to guide the laser pulse over many Rayleigh lengths for LWFA without the laser self-guiding power threshold [42-

44]. A plasma channel with a roughly parabolic transverse density profile can guide a laser pulse if the increase in density over the spot size w_0 is approximately $\Delta N_e \approx \frac{1}{\pi r_e w_0^2}$, where r_e is the classical electron radius [43]. With a plasma channel, a laser pulse with a relatively modest power can be used for high energy LWFA. It was reported that a 40TW laser pulse is used to generate > 1 GeV electrons by LWFA in plasma channels produced in a capillary discharge waveguide [45].

1.4. Direct Laser Acceleration (DLA)

Though LWFA has a number of advantages, it depends on a nonlinear laser plasma interaction, requiring multi-TW laser systems. Several laser acceleration schemes have been suggested as alternatives for small-scale laser systems, such as the inverse Cherenkov Accelerator [46], the semi-infinite vacuum accelerator [47], and vacuum beat wave accelerator [48, 49]. Yet, these schemes suffer a low acceleration gradient (< 40MV/m) and a short acceleration distance (Rayleigh length). Quasi-phasematched direct laser acceleration (QPM-DLA) in an axial density modulated plasma channel is proposed to provide high acceleration gradients at non-relativistic laser intensity over an extended distance (~cm) [50]. For example, a QPM-DLA acceleration gradient of 10.6MV/cm can be achieved with a 30GW laser pulse. In the QPM-DLA scheme, an electron beam is accelerated by a phase-matched axial spatial harmonic of a co-propagating radially polarized laser pulse guided in a corrugated plasma waveguide. The energy gain in QPM-DLA grows linearly with the length of plasma waveguide as long as the electrons do not outrun the laser pulse.

1.4.1. Generation of corrugated plasma waveguide

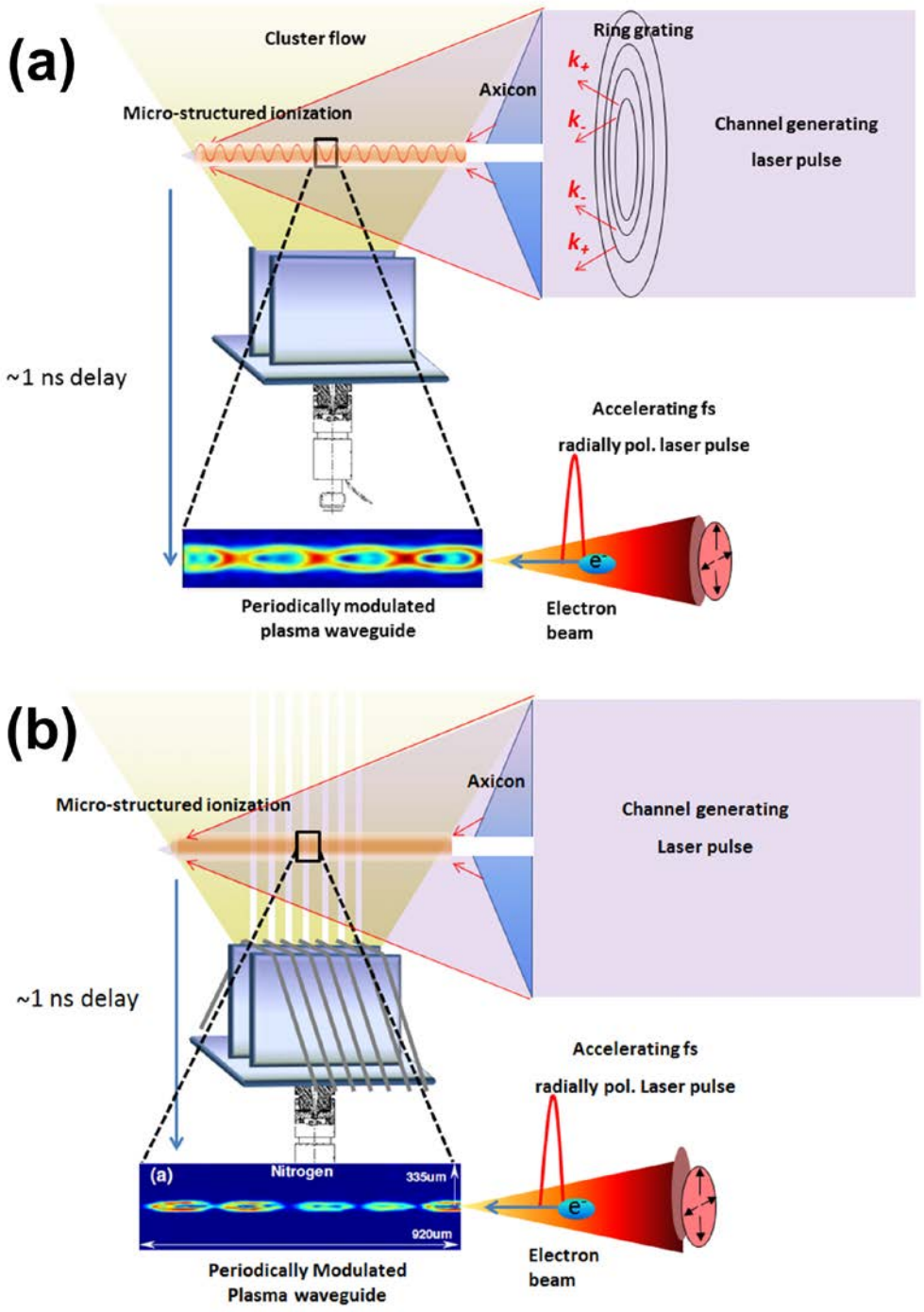

Figure 1.9. Experimental setups to generate a corrugated plasma waveguide using (a) a ring grating to modulate the intensity profile of the channel generating laser pulse and (b) an array of wires to modulate the cluster flow. A schematic of QPM-DLA is also presented.

Corrugated plasma waveguides are the key element for QPM-DLA. They guide the driving laser pulse and also provide an axially periodic density modulation that enables phase matching between the guided EM field and the accelerated electron bunch. Our group has demonstrated generation of plasma waveguides with axial density modulations by two different methods: i) modulation of the intensity profile of the ionizing laser pulse with a transmissive ring grating and ii) modulation of the cluster flow with an array of wires [51, 52]. For both cases, the targets are clusters, solid density atomic aggregates with 1-100nm radii, formed from cooled high pressure gas as it expands into vacuum [53]. Once clusters are formed, a 140ps mode-locked Nd:YAG laser pulse is line focused by an axicon to ionize a column of clusters. Collisional ionization within the solid density clusters at the leading edge of the channel forming pulse creates a highly ionized plasma. This plasma is then efficiently heated through inverse bremsstrahlung over the full duration of the long (140ps) channel forming pulse [54]. Effective ionization/heating of clusters by high power laser interaction and 10Hz repetition rate operation makes gas jet-generated clusters a practical target for plasma waveguide generation [54].

Fig. 1.9(a) illustrates the method of modulating the intensity of the channel generating laser pulse using a ring grating to generate a corrugated plasma waveguide. A ring grating is a transmissive diffraction grating with concentric ring shaped patterns. Interference between the two wavevectors, k_+ and k_-, arising from the ring grating results in radial intensity modulation. Radial intensity modulation transfers into axial intensity modulation upon focusing by an axicon. Local intensity variation in the line focus results in differential heating of the resulting plasma. After

about a nanosecond delay depending on the cluster species, different local expansion speeds of plasma lead to an axial density modulation in a plasma waveguide.

Modulation of the target cluster flow with an array of thin ($\sim 50\mu m$) wires is an alternative way to generate corrugated plasma waveguides. By placing an array of the wires across an elongated cluster jet as described in Fig.1.9(b), we can impart shadows of the wires in the cluster flow as long as the clusters are ballistic with respect to the size of the obstructing wires. A particle flow is considered ballistic when the mean free path of particles is greater than the size of obstruction. With atomic/molecular gases from a supersonic gasjet, shockwaves are launched from the obstructing wires and disrupt the flow. The full transition from non-ballistic to ballistic flow upon $50\mu m$ tungsten wire obstruction is described in chapter 4. In QPM-DLA, a small modulation period ($< 200\mu m$) is desirable to trap and accelerate low energy electrons, because the phase velocity of the accelerating field is slower when the modulation period is smaller, which will be discussed in detail in chapter 2. However, our previous study [52] observed that plasma density between neighboring wires drops when the wire spacing is less than $200\mu m$. In chapter 4, this question is resolved, and we show that density modulation periods as small as $70\mu m$ can be achieved.

Once a corrugated plasma waveguide is formed, a drive laser pulse is guided to accelerate copropagating electrons. A radially polarized laser pulse is used as a drive laser pulse in the scheme, because a radially polarized laser pulse has a maximum longitudinal component on axis.

1.4.2. Quasi-phaematching in a corrugated plasma waveguide

The phase velocity of the laser in a uniform plasma waveguide is strictly superluminal, so that a relativistic electron ($v_e \approx c$) will be 2π out of phase from the initial phase of the laser field after a dephasing length $L_d = \lambda\left(N_0 / N_{cr} + 2\lambda^2 / \pi^2 w_{ch}^2\right)^{-1}$ [50], where λ is the laser wavelength, N_0 is the on axis electron density of the channel, N_{cr} is the critical density of the laser, and w_{ch} is the channel radius. In a uniform plasma waveguide, acceleration of an electron over $L_d / 2$ will be exactly cancelled by deceleration over the next $L_d / 2$, leaving zero net acceleration. However, in a corrugated plasma waveguide, if the density modulation period is set to L_d, then the length of the acceleration phase can be longer than that of the deceleration phase over one dephasing length, depending on the initial relative phase between the accelerating field and an electron. In this case, the electron will gain net energy over one dephasing length. The net energy gain will continue over the repeating dephasing cycles. This picture of net energy gain is analogous to the quasi-phasematching in nonlinear optics [55], since we use a periodic medium to compensate the mismatch between the phase velocity of the accelerating field and the electron velocity. Although the concept of QPM-DLA has been well investigated analytically [56, 57], a study based on PIC simulations is necessary to validate the concept with a more realistic simulation tool and to understand the effect of a nonlinear plasma wave on direct laser field acceleration. Chapter 2 of this dissertation presents our investigation of QPM-DLA using PIC simulations.

1.5. Particle-In-Cell (PIC) code

The majority of plasmas in the universe are collisionless, and the kinetics of the particles are the major part of the dynamics. The plasmas simulated in this thesis are essentially collisionless on the timescales of interest. Maxwell's equations and Newton-Lorentz equations of motion are the main part of the algorithm to simulate collisionless plasmas, leading to the method called "particle-in-cell" (PIC) simulation. The PIC code has become a standard tool in laser plasma physics [58-61]. For the studies in this dissertation, we used a PIC code, TurboWAVE [62]. TurboWAVE is a framework for solving the Maxwell-Lorentz system of equations for charged particle dynamics, which will be discussed in detail later in this section. The model is fully relativistic and fully electromagnetic. TurboWAVE can perform PIC simulations in full 3D space as well as in a 2D cylindrical coordinate system, enabling computationally efficient and physically accurate simulations of cylindrically symmetric problems like QPM-DLA in Chapter 2.

1.5.1. Principles of PIC simulations

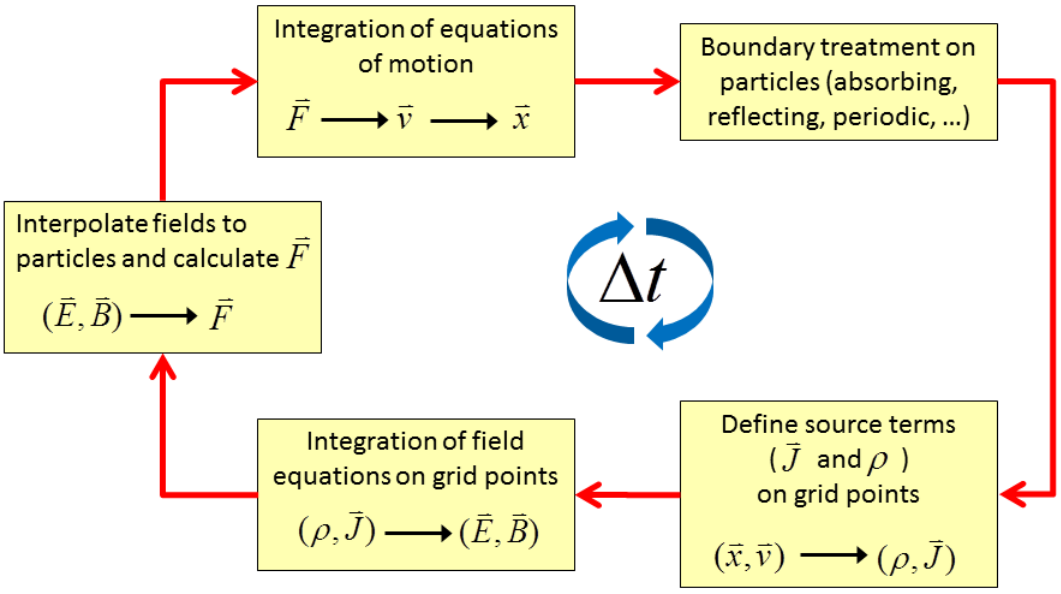

Figure 1.10. Process flow of PIC simulation at each time step (Δt)

The flow of the PIC algorithm is illustrated in Fig. 1.10. Particles in PIC simulations have electrical charge and their trajectories evolve in continuous space but are updated at discrete times. The fields are discretized in both space and time. Starting from the initial condition, the particles (position, momentum) and the fields are calculated and updated sequentially at each discrete time step. The scheme for the time advance is described in Fig. 1.10. The calculation of the particle velocity is offset from the calculation of the particle position and the fields by a half a time step (Δt). This allows the leapfrog integration of Eq. (1.20) and (1.21) using central differencing [58]. The leapfrog integrator performs integration with accuracy to $O\left(\Delta x^2\right)$, whereas the conventional Euler integration has the first order accuracy

$O(\Delta x)$ [58]. The positions of particles at the next time step ($t + \Delta t$) are calculated by using the current (t) fields interpolated from the discrete cells to the continuous current (t) positions of the particles. Equations of motion are used to determine the 3D position, $\vec{x}$, and the 3D velocity, $\vec{v}$, of individual particles, given as

$$\frac{d\vec{x}}{dt} = \vec{v} \tag{1.20}$$

$$\frac{d}{dt}(\gamma m\vec{v}) = \vec{F} \tag{1.21}.$$

Converting these equations into the integral form using the Leapfrog central difference integrator,

$$\vec{x}(t + \Delta t) = \vec{x}(t) + \vec{v}\Delta t \tag{1.22}$$

$$\gamma m\vec{v}\left(t + \frac{\Delta t}{2}\right) = \gamma m\vec{v}\left(t - \frac{\Delta t}{2}\right) + \vec{F}(t)\Delta t \tag{1.23}.$$

It is nearly impossible to track individual physical particles for general plasma physics simulations. However, a statistical sample of particles, i.e. a macroparticle, is enough to capture all physical phenomena of interest, given that the number of macroparticles is large enough for statistics.

To define fields, Maxwell's equations are solved with updated source terms ($\vec{J}$ and ρ) at each time step. At each cell, the source terms and potential are known. The charge, ρ, and potential, Φ, are related by Poisson's equation,

$$\nabla^2\Phi = 4\pi\rho \tag{1.24}.$$

The current and density sources can be calculated using the distribution of the particles and velocities as follows:

$$\rho(r) = \sum_j q_j S\left(r_j - r\right) \tag{1.25}$$

$$\vec{J}(r) = \sum_j q_j \vec{v}_j S\left(r_j - r\right) \tag{1.26},$$

where $S\left(r_i - r\right)$ is a shaping function describing the charge distribution. Once the simulation is initialized by defining the source terms ($\vec{J}$ and ρ) and the potential (Φ), $\vec{E}$ and $\vec{B}$ fields can move forward in time using Ampere's law and Faraday's law in the generalized finite-difference format as follows [64]:

$$\text{Ampere's law: } \vec{\nabla} \times \vec{E} = -\frac{1}{c}\frac{\partial \vec{B}}{\partial t}, \qquad \delta_t B_i = -c\left(\delta_j E_k - \delta_k E_j\right) \tag{1.27}$$

$$\text{Faraday's law : } \vec{\nabla} \times \vec{B} = \frac{1}{c}\frac{\partial \vec{E}}{\partial t} + \frac{4\pi \vec{J}}{c},\ \delta_t E_i = c\left(\delta_j B_k - \delta_k B_j\right) - 4\pi J_i \tag{1.28},$$

where δ is the first order partial derivative respect to the subscripted label according to the Einstein's notation. $\vec{\nabla} \cdot \vec{E} = 4\pi\rho$ and $\vec{\nabla} \cdot \vec{B} = 0$ will remain satisfied over time, once it is satisfied initially. For fast calculation of fields, Fourier transformed forms of Maxwell's equations are often used by replacing $\vec{\nabla}$ with $i\vec{k}$ [63, 64].

For convenience, all the variables in the code, especially in the PIC code used in this dissertation "TurboWAVE" [62], are normalized by density related factors as shown in Table 1.2.

Variables	Real unit	Normalized unit in PIC
Time	t	$\omega_p t$
Length	x	$\left(\omega_p / c\right) x$
Velocity	v	v / c
Electric field	E	$\left(e / m\omega_p c\right) E$
Potential	ϕ	$\left(e / mc^2\right) \phi$
Density (electron/ion)	$n_{e,i}$	$n_{e,i} / n_0$

Table 1.2.Normalization of variables in the PIC code.

1.5.2. Determining simulation parameters

Special care should be taken when simulation parameters are chosen to ensure physically correct results. Most of the PIC simulations are based upon these assumptions: i) space and time are discretized, ii) a macroparticle represents many particles of the same kind, iii) there is no collisional interaction among particles unless a collision scheme such as the Monte Carlo Collision (MCC) scheme is applied [65].

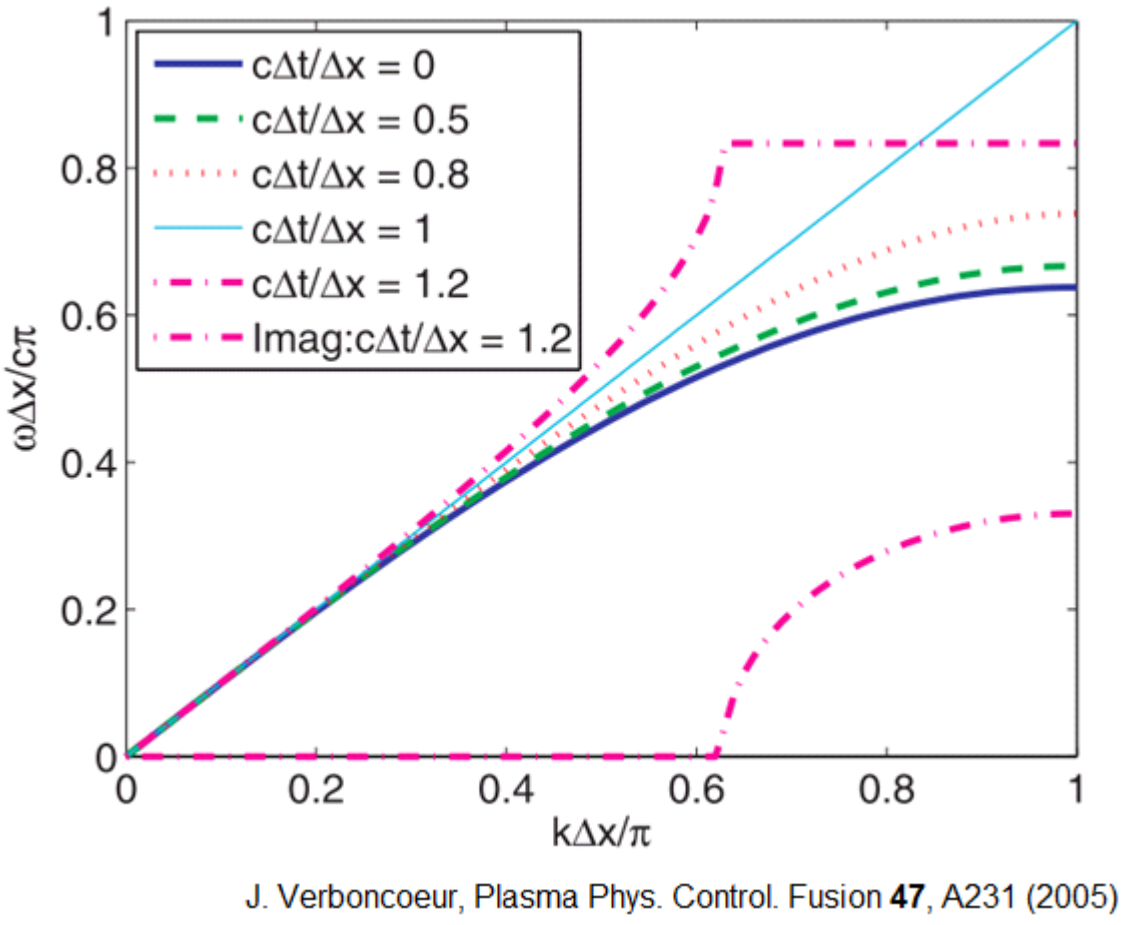

Figure 1.11.Vacuum dispersion curve for a wave equation using leapfrog difference methods

[64]

If the discretization of space and time is too coarse, wave propagation can become unstable in simulations. As mentioned above, the center difference method has better accuracy than forward/backward difference methods. However, the Courant-Levy stability criterion should be met to ensure stable simulations:

$$\Delta t \le \frac{1}{c}\left(\sum_j \frac{1}{\left(\Delta x_j\right)^2} \right)^{-1/2} \qquad (1.30),$$

where Δt is the time step size and Δx_j is the cell size in the j^{th} dimension of space [66]. If this condition is not met, the imaginary part of the dispersion relation increases rapidly, as shown in Fig. 1.11. It is worth noting as illustrated in this figure that the phase error grows if the cell size is bigger, even if the Courant-Levy criterion is met. This indicates that the cell size should be small enough in the longitudinal direction to minimize phase velocity error, especially for simulations over long propagation distances.

An excessively high number of particles in a macroparticle can result in the development of artifacts in the particle density distribution. For that reason, computation time and minimizing errors in the density distribution should be considered when deciding the number of particles that a macroparticle represents.

There are two primary ways to distribute particles on the grids; noisy starts and quiet starts [67]. In the noisy start, particles are distributed in space and velocity from a random number generator. Because macroscopic quantities in nature contain fluctuations, the simulations can more realistically model particle behavior at the

initial phase. However the number of particles is greatly reduced in simulations through the use of macroparticles, and, as a result, the fluctuations in the simulation can be much larger than those appearing in nature. This can lead to unwanted noise growth in the simulations when opposite charges are distributed in space from independent random number generators. On the other hand, in a quiet start, the particles are loaded evenly in space and velocity. A quiet start significantly reduces noise in simulations, so that a quiet start is often a more desirable way to initialize a simulation. However, a quiet start simulation can still face the growth of noise after a sufficiently long time, since all physical systems eventually move towards thermal equilibrium. The noise growth rate can be minimized by employing non-uniform velocity distribution.

1.6. Outline of the Dissertation

This dissertation presents theory and simulation for new laser plasma accelerator schemes with axially modulated plasma waveguides, and investigates the physics issues associated with those schemes. In addition, experiments probing the gas jet dynamics during generation of the density modulated waveguide and generating seed electrons are presented. Chapter 1 gives a brief review of conventional RF based accelerator schemes and the nonlinear interaction of a high intensity laser pulse with plasma. Then it continues to provide background information on LWFA and QPM-DLA. The simulation tool in this thesis, the particle-in-cell (PIC) code, is also introduced.

Chapter 2 presents the results of PIC simulations of quasi-phasematched direct

laser acceleration (QPM-DLA) of electrons in a corrugated plasma waveguide, demonstrating linear acceleration of electrons by the phase-matched laser field in a density modulated plasma channel. Modifications to the acceleration arising from nonlinear plasma waves are also investigated. In addition, simulation results show that a density ramp leading into the plasma waveguide can reduce the threshold energy of injected seed electrons for trapping and acceleration.

The new concept of quasi-phasematched laser wakefield acceleration is introduced in chapter 3. A corrugated plasma waveguide can alter the phase velocities of not only laser fields, as in QPM-DLA, but also of plasma waves. Theoretical analysis and simulations of electron acceleration by quasi-phasematched plasma waves are presented, demonstrating the scheme's feasibility as a new accelerator concept.

The subsequent chapters describe experiments aimed at constructing more efficient plasma acceleration structures for the schemes described in chapters 2 and 3. One method of imparting density modulations in a plasma waveguide is to modulate cluster flow density with an array of periodic wires. In chapter 4, we show how elimination of shock wave generation from the wires is essential for achieving fine modulation periods.

Chapter 5 studies how laser-driven ionization injection promotes LWFA in a pure N^{5+} waveguide, which enables electron acceleration with reduced laser power. Experimental verification of the generation of N^{5+} channels is presented first, and then an analysis of electron acceleration in the N^{5+} channel is provided along with PIC simulation results. These electrons could possibly be used as seed electrons for

the schemes described in chapters 2 and 3.

Finally, Chapter 6 summarizes all the results of the simulations and experiments, and discusses future directions.

Chapter 2: Quasi-Phasematched Direct Laser Acceleration of Electrons in a Corrugated Plasma Channel

2.1 Introduction

As discussed earlier in chapter 1, the absence of laser power threshold for acceleration makes QPM-DLA a perfect candidate for a small size, high repetition rate (~kHz) laser-plasma accelerator. In this chapter, we explore, through theory and PIC simulations, the QPM-DLA of electrons in an axially modulated plasma waveguide. We also investigate density ramping in corrugated plasma waveguides for lowering the required injection energies for the seed electron beam in QPM-DLA.

In the context of QPM-DLA, quasi-phasematching refers to matching the electron velocity to the phase velocity of an individual spatial harmonic comprising an electromagnetic wave propagating in an axially modulated structure. In analogy with quasi-phasematching in nonlinear optics, we use a periodic medium to compensate the difference between the electron velocity and the phase velocity of the accelerating field to transfer energy from the accelerating field to the electron. In nonlinear optics, perfect phase matching requires the phase velocity of the nonlinear source term (the nonlinear polarization) to be equal to that of the generated light, such as the second harmonic; equivalently, the wavevectors of these two waves are equal. In the absence of phase matching, a modulation in the nonlinearity or in the refractive index can be introduced along the propagation axis (axial modulation) such that the wavevector-mismatch (phase velocity mismatch) between the two waves is provided

by the effective wavevector of the structure. This allows net energy transfer from the nonlinear polarization wave to the desired product electromagnetic wave [55]. For direct laser acceleration of electrons, perfect phase matching would require matching the electron velocity to the phase velocity of the accelerating electromagnetic wave. However, because an electron cannot gain energy from an electromagnetic wave in an axially uniform propagation medium or structure, one must introduce an axially periodic structure that compensates the velocity mismatch. The principle of matching the period of the structure to the dephasing length is required in both the nonlinear optics case and the electromagnetic wave + electron beam case.

In the scheme described here, an electron beam co-propagating with a radially polarized laser pulse injected into a corrugated plasma waveguide is accelerated by a phase-matched axial spatial harmonic of the resulting guided electromagnetic field, providing linear energy gain over the interaction length [68]. In order to achieve linear energy gain over an extended interaction length, three things are required: slow electromagnetic waves (providing quasi-phasematching), a channel for guiding the laser pulse (eliminating diffractive spreading of the laser pulse)[69,70], and radial polarization (providing a component of electric field along the propagation axis)[68].

In uniform plasma, the phase velocity of a light wave is greater than the speed of light in vacuum making linear, direct acceleration of charged particles with laser pulses impossible. This is an extension of the Lawson-Woodward theorem [71], which states that the energy gain of an electron accelerated by the linear field of a laser pulse in vacuum over an infinite distance is zero. Linear acceleration can however be achieved through quasi-phasematching of electromagnetic waves to

charged particles. Quasi-phasematching requires a structure whose dispersion allows for "slow-waves" or components of the electromagnetic wave with subluminal phase velocities. Layer *et al*. succeeded in imparting axial density modulations on a miniature plasma channel creating an ideal structure for quasi-phasematching [51, 52]. The longitudinal periodicity of the structure provides dispersion where a single frequency is associated with a spectrum of axial wavenumbers, some associated with subluminal phase velocities. In addition to providing slow wave dispersion, the corrugated plasma channel provides a guiding structure for laser pulses. As a plasma, it eliminates the damage limitation typical of metallic guides or solid-state dielectric guiding structures. Even with slow wave dispersion, a linearly polarized laser pulse cannot accelerate electrons along the axis of the channel without an appropriate field component in the acceleration direction. The axial field associated with a linearly polarized laser pulse is zero on axis. A radially polarized laser pulse, on the other hand, has a longitudinal component whose transverse dependence has a maximum on axis. This longitudinal component is obtained by Gauss' law, giving $(1/r)\partial(rE_r)/\partial r = -\partial E_z/\partial z$ for cylindrical symmetry.

To illustrate the principle of QPM-DLA and find a scaling for energy gain we consider a simple model presented by Palastro *et al.* [56, 57]. The radial component of the laser pulse vector potential in the plasma channel can be expressed in envelope form as follows

$$A_\perp = \hat{A}_r(r,z,t)\exp\left[i(k_0 z - \omega_0 t)\right] + c.c. \qquad (2.1)$$

where k_0 and $\omega_0 = ck_0$ are the central wavenumber and frequency of the laser pulse respectively and $\hat{A}_r$ is the envelope function. Azimuthal symmetry of the laser pulse

is assumed. We consider channel electron densities with $\omega_p << \omega_0$, where $\omega_p^2 = 4\pi e^2 n_e(r,z)/m_e$ is the plasma frequency squared, m_e and e are the electron mass and the electron charge. In this limit, the temporal and spatial variation of $\hat{A}_r$ during propagation are slow compared to ω_0 and k_0 respectively, and the slowly-varying envelope equation can be used to describe the evolution of the laser pulse

$$\left[2ik_0\left(\frac{\partial}{\partial z}+\frac{1}{c}\frac{\partial}{\partial t}\right)+\frac{1}{r}\frac{\partial}{\partial r}r\frac{\partial}{\partial r}-\frac{1}{r^2}\right]\hat{A}_r=\frac{\omega_p^2(r,z)}{c^2}\hat{A}_r. \qquad (2.2)$$

Equation (2.2) includes only the linear plasma response to the vector potential, thus our model is limited to the consideration of non-relativistic vector potentials $a_0 = eA_0/m_e c^2 < 1$, where A_0 is the amplitude of $A_\perp$. We consider the following density profile mimicking the experimental results of Layer *et al.*[51, 52]:

$$n_e(r,z) = n_0\left[1+\Gamma\sin(k_m z)\right]+\frac{1}{2}n_0'' r^2, \qquad (2.3)$$

where Γ is modulation amplitude and n_0'' determines the curvature of the channel.

The lowest order transverse mode solution of Eq. (2.2) is

$$\hat{A}_r(r,z,t) = A_0\frac{r}{w_{ch}}e^{-r^2/w_{ch}^2-(z-v_g t)^2/\sigma_z^2}\sum_n i^n J_n(\psi)e^{-i\psi+i(\delta k+nk_m)z} \qquad (2.4)$$

where σ_z is the axial extent of the laser pulse, $w_{ch}^2 = 2c(2/\omega_{p0}'')^{1/2}$ where $\omega_{p0}''^2 = (e^2/m_e)n_0''$, $J_n(\psi)$ is the nth Bessel function of the first kind, $\psi = \Gamma\omega_{p0}^2/2c^2k_0k_m$, and $\delta k = -k_0^{-1}(\omega_{p0}^2/2c^2 + 4/w_{ch}^2)$. The pulse envelope is a sum of spatial harmonics with $J_n(\psi)$ determining the relative amplitude. For typical experimental parameters, $\psi << 1$ and $J_n(\psi) \sim \psi^n/2^n n!$: the relative amplitude drops

rapidly with increasing harmonic number n. For maximum acceleration we want to consider the $n=1$ spatial harmonic. With Eq. (2.4) we can extract the longitudinal accelerating field of the first spatial harmonic, using $\vec{\nabla}\cdot\vec{A}\approx 0$ for $(\omega_p/\omega_0)^2 << 1$ for which we find

$$\hat{A}_{z,1}(r,z,t)=i\frac{2J_1(\psi)}{k_0 w_{ch}}A_0 e^{-r^2/w_{ch}^2-(z-v_g t)^2/\sigma_z^2-i\psi+i(\delta k+k_m)z}. \qquad (2.5)$$

The corresponding phase velocity for the $n=1$ spatial harmonic is then

$$\frac{v_{p,1}}{c}\approx 1-\frac{k_m}{k_0}+\frac{\omega_{p0}^2}{2\omega_0^2}+\frac{4}{(k_0 w_{ch})^2}, \qquad (2.6)$$

where we have assumed $|k_0|>>|k_m|,|\delta k|$. By an appropriate choice of k_m, we can tune the phase velocity for QPM-DLA. In particular, simple analysis shows that the ideal phase velocity for a relativistic electron beam is $v_{p,1}=c$, or $k_m=-\delta k$ [50].

With the analytic expression for the vector potential in a corrugated waveguide, a scaling law for energy gain of an electron can be derived. A test electron with initial conditions $(r,v_r,z,v_z)=(0,0,z_0,v_{z,0})$ is considered for the scaling law. The initial velocity of the electron, $v_{z,0}$, is taken close to c so that phase matching between the electron and the spatial harmonic is ensured over the interaction distance. Using $\Delta\gamma=-q/m_e c^3\int\vec{v}\cdot\partial_t\vec{A}dt$, we obtain the energy gain for a test particle in a constant laser field:

$$\Delta\gamma\sim 2\Gamma a_0\left(1+\frac{2\lambda_p^2}{\pi^2 w_{ch}^2}\right)^{-1}\left(\frac{z_{\min}}{w_{ch}}\right), \qquad (2.7)$$

where z_{min} is the minimum interaction length. In particular the interaction length can be limited by the length of the channel, the time it takes for the electrons to travel through the laser pulse, or defocusing effects in the beam. The energy gain increases linearly with modulation amplitude, Γ, and laser amplitude, a_0, and is inversely proportional to w_{ch}, a result of larger axial fields in narrower channels.

In this chapter, a study is presented on QPM-DLA using fully self-consistent particle-in-cell (PIC) simulations. The simulations are used to validate the simple model described above, examine the self-consistent electrostatic fields generated by the beam itself, and to conduct preliminary studies on density ramping for lowering the required injection energies in QPM-DLA. This chapter is organized as follows. In section 2.2, we describe the 2D cylindrical PIC simulation, TurboWAVE, and validate the code for QPM-DLA simulations. In section 2.3, we present simulation results of electron acceleration in corrugated waveguides and comparisons to analytic predictions. Section 2.4 includes an analytic model and simulations of reduced energy threshold electron acceleration using a plasma density ramp. Section 2.5 concludes this chapter with a summary on the simulations and future directions of study.

2.2 Code details & verification

In order to account for nonlinear effects, and to more fully describe the dynamics of the accelerated electrons, 2D axisymmetric particle-in-cell (PIC)

simulations are used. In this work we used the code TurboWAVE [62]. General information on TurboWAVE code can be found in section 1.5. of this thesis. For the 2D axisymmetric simulations described in this chapter, the fields are advanced using a straightforward extension of the usual Yee solver [72] to the case of cylindrical coordinates. The sources are deposited using linear weighting, with charge conservation ensured by means of a Poisson solver [58]. Since dynamics on the timescale of the laser period are important, the full relativistic equations of motion are solved.

The simulations are done in a moving frame, which moves at *c*. In the moving frame the coordinates are $\xi = z - ct$ and t, where ξ represents distance in the moving frame. The extent of the simulation window is $80\,\mu m$ in the transverse direction and $100\,\mu m$ in ξ. The number of grid points used in the transverse direction and the ξ direction are 512 and 4096, respectively. The radially polarized laser pulse is initialized as a lowest order associated Laguerre Gaussian mode with a wavelength of 800 nm, longitudinal width of 100 fs in e^{-1}, and transverse radius of $15\,\mu m$ in e^{-1}. The field amplitude is varied. The pulse begins outside the channel and unless otherwise stated the plasma density is ramped up linearly over $20\,\mu m$. After the initial ramp, the electron density is given by the equation:

$$n_e(r,z) = \begin{cases} n_0\left[1+\Gamma\sin\left(k_m z\right)\right]\left(1+\frac{1}{2}n_0'' r^2\right) & r < r_c \\ 0 & r \geq r_c \end{cases}, \qquad (2.8)$$

where $r_c = 70\,\mu m$. The channel has a parabolic density profile in the transverse direction to which the laser pulse is matched and a sinusoidal density oscillation in

the longitudinal direction. The channel terminates at some radius allowing for side loss of electromagnetic energy. Four particles are loaded at each cell to represent electrons consisting a plasma waveguide. The parameters for the density profile are an average density $n_0 = 7 \times 10^{18} cm^{-3}$, a modulation amplitude of $\Gamma = 0.9$, and a modulation period of $356 \mu m$. This choice of parameters sets the phase velocity of the 1st spatial harmonic to c based on the simple theory and are experimentally realizable [50]. Later we will show that electron energy gain is sensitive to the choice of modulation period. The ions evolve on a time scale much longer than the pulse duration and are set to be immobile in the simulation.

We examine the validity of the simple theory and 2D cylindrical PIC code by confirming the presence of spatial harmonics of a laser pulse guided in a corrugated plasma channel. This is done using two methods. The first is a Fourier decomposition of the electromagnetic field. For the Fourier decomposition we consider a small vector potential $a_0 = 0.01$ to ensure linear propagation and a deliberately small density modulation period of $2\pi / k_m = 20 \mu m$. While this is not the optimal period for direct acceleration it is more computationally efficient for examining the spectral structure of the electromagnetic field. In particular the wavenumber resolution in a discrete Fourier transform is given by $2\pi / L$, where L is the length of the moving frame box. If we wish to resolve spectral features due to the modulations, the Nyquist condition must be satisfied: $k_m L >> 2\pi$. In addition, we are required to resolve the central laser wavenumber: $k_0 \Delta\xi << 2\pi$. Combining these two conditions we see that $N_\xi >> k_0 / k_m$, where N_ξ is the number of numerical grid

points in ξ: the larger the modulation period, the more computationally intensive the calculation.

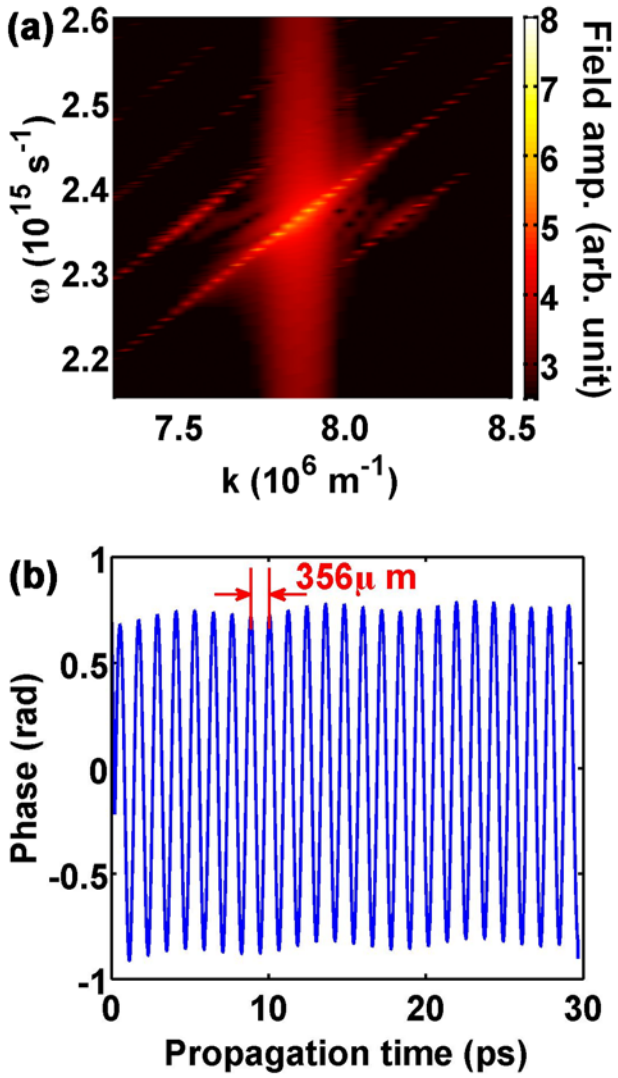

Figure 2.1. (a) Fourier transform of the longitudinal electric field (E_z) in time (t) and space (z) at a laser wavelength $\lambda_L = 800\,nm$, normalized vector potential $a_0 = 0.01$, modulation period $d = 20\,\mu m$, and modulation amplitude $\Gamma = 0.9$. The diagonal lines represent the spatial harmonics. The fundamental spatial harmonic is the central diagonal line. The diagonals to the left and right of the fundamental are +/- 1st spatial harmonics respectively. (b) Phase of the on-axis longitudinal electric field at a fixed ξ point. The period of the phase oscillation corresponds to the density modulation period.

For examining the spectral properties, we Fourier transform the on-axis longitudinal electric field, E_z, from the simulation in both time and space. Figure 2.1(a) shows the magnitude of the Fourier transform on a log scale as a function of ω and k. The fundamental spatial harmonic is the brightest diagonal line in Fig. 2.1(a) surrounded by the $n = \pm 1$ spatial harmonics. The higher order spatial harmonics, $|n| > 1$, are dim in this figure. As expected the amplitude of these modes drops rapidly as n increases. To compare to the simulation, we consider the theoretical ratio of the fundamental and first spatial harmonics $J_1(\psi)/J_0(\psi)$, and the simulated ratio. We consider two different density modulation amplitudes: $\Gamma = 0.9$ and $\Gamma = 0.2$. Table 2.1 shows excellent agreement between the simulation results and the analytical calculation. It also tells us that the modulation of plasma density in a plasma waveguide excites spatial harmonics, and the ratio is linearly proportional to the modulation amplitude.

Modulation Amplitude	Amplitude Ratio (Theory)	Amplitude Ratio (Simulation)
$\Gamma = 0.2$	0.0055	0.0051
$\Gamma = 0.9$	0.025	0.023

Table 2.1. Comparison between the ratios of the fundamental and first spatial harmonics from theory and simulation

The second method for confirming the presence of spatial harmonics is extraction of the electromagnetic field's phase. The phase contains information about the linear response of the media and more specifically the spatial profile of the background electron density. The connection between the first and second approach

is manifest in the relationship: $\sum_n i^n J_n(\psi)\exp[ink_m z] = \exp[i\psi\cos(k_m z)]$. Periodic phase oscillations lead to the presence of spatial harmonics. From Eq. (2.4) we can write the total phase of the laser pulse as $\phi_T(\xi,t) = (k_0 + \delta k)\xi + c\delta kt - \psi\cos[k_m(\xi + ct)]$. For extracting the phase from the simulation we consider a small vector potential $a_0 = 0.1$ to ensure linear propagation and a standard modulation period of $356\mu m$. A benefit of phase extraction is that there are no additional numerical requirements as with the Fourier decomposition. Again we consider the on-axis axial field. The phase is defined by

$$\phi = \arctan\left[\frac{\mathrm{Im} < e^{ik_0\xi} E_z >_t}{\mathrm{Re} < e^{ik_0\xi} E_z >_t}\right] \tag{2.9}$$

where the brackets represent an average over one period of the laser pulse and $\phi \approx \phi_T - k_0\xi$. The averaging removes the variation at the carrier wavenumber leaving only the slowly evolving component. This method is only valid when the variation at k_0 is much faster than any other variation in the laser pulse: $k_0 >> |\delta k|, k_m$. Figure 2.1(b) shows the phase oscillation due to the channel density modulation. As expected, the oscillation period in time corresponds to the modulation period.

2.3 2D Particle-In-Cell simulation results

In this section, we present results of fully self-consistent 2D cylindrical PIC simulations of QPM-DLA. For QPM-DLA the co-propagating electron beam is initialized as a Gaussian in both the transverse and longitudinal directions with a transverse and longitudinal e^{-1} length of $3\mu m$ and $5\mu m$ respectively. Eight particles

per cell are used to represent the co-propagating electron beam. The beam electrons start with identical longitudinal momentum and no transverse momentum. The beam density is varied. Due to the subluminal group velocity of the laser pulse, the laser pulse will move backwards with respect to the electron beam. To maximize the electron acceleration during 1 cm of propagation, the beam is initially located $10\mu m$ behind the peak of the laser pulse.

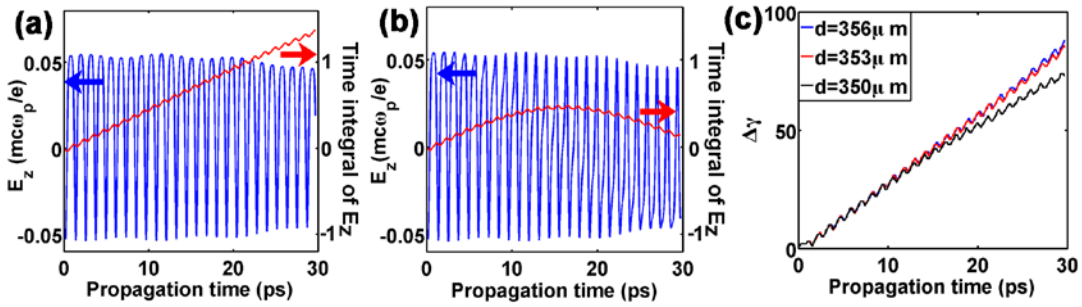

Figure. 2.2. On-axis longitudinal electric field (blue) and time integral of the on-axis longitudinal electric field (red) as a function of acceleration time for a fixed ξ point. In (a) the modulation period matches the dephasing length, $L_d = 356\mu m$, while in (b) the modulation period is $d = 350\mu m$. (c) Self-consistent energy gain as a function of acceleration for three different modulation periods: $350\mu m, 353\mu m$, and $356\mu m$.

We first consider the longitudinal field experienced by an on-axis, highly relativistic test electrons in a laser pulse with $a_0 = 0.1$ over 9 mm. Figure 2.2(a) shows the on-axis longitudinal electric field for a fixed value of ξ in blue. In a plasma channel without modulations the oscillation would be sinusoidal with a period of $L_d = 2\pi/|\delta k|$, which we refer to as the dephasing length. The dephasing length is the distance over which an electron moving at velocity c would see the laser pulse slip by one wavelength in an unmodulated channel. The oscillation here shows the phase evolution of all of the spatial harmonics except $n = 1$ whose phase velocity is

identically c. In general each spatial harmonic will undergo a 2π phase oscillation in a distance $L_d(n) = 2\pi k_m^{-1}(n-1)^{-1}$ for $n \neq 1$, where we have used $k_m = -\delta k$. The predominant mode in Fig. 2.2(a) is the fundamental spatial harmonic, but the presence of the other spatial harmonics is noticeable in the non-sinusoidal shape of the oscillation. The red curve in Fig. 2.2(a) shows the energy gain calculated from $W(\xi,t) = -ce\int_0^t E_z(\xi,t)dt$. By setting the modulation period equal to the dephasing length we have ensured that the $n = 1$ spatial harmonic is stationary in the frame of an electron moving with a velocity near c. The relative phase of the electron and spatial harmonic does not change and the electron undergoes linear energy gain. The oscillations in energy are due to the electron quiver motion from the other spatial harmonics.

In Fig. 2.2(b) the modulation period is chosen to be smaller such that $k_m \neq -\delta k$ and the $n = 1$ spatial harmonic no longer has a phase velocity identical to c. In particular the modulation period is set to $350\mu m$, $6\mu m$ less than L_d. The waveform changes noticeably over 1 cm propagation. Each spatial harmonic now undergoes a 2π phase oscillation in a distance $L_d(n) = 2\pi \mid nk_m + \delta k \mid^{-1}$, which cannot be related by integer multiples for each n. This results in the spatial harmonics dephasing from one another and causing the waveform to change shape. Again, the red line shows the energy gain, and as expected the electron initially gains energy then loses energy as none of the spatial harmonics are stationary in the electron frame. This demonstrates that QPM-DLA is sensitive to the matching between modulation period and the dephasing length. We note that the length of the plasma waveguide can be reduced to account for this sensitivity. For example, if the

modulation period is $350\mu m$ and the plasma waveguide is $0.45\ cm$ (12 ps) electrons will gain energy over the entire interaction length.

Figure 2.2(c) shows self-consistent energy gains over 9mm for an initial energy $\gamma_0 = 200$ and laser pulse amplitude $a_0 = 0.1$ for different modulation periods $d = 350\mu m$, $353\mu m$, and $356\mu m$ in black, red, and blue respectively. The energy gain for $356\mu m$ and $d = 353\mu m$ is almost identical. Even with $d = 350\mu m$ the electron gains more energy than is predicted in Fig. 2.2(b). The discrepancy between Fig. 2.2(b) and 2.2(c) can be explained as follows. In Fig. 2.2(b) the electron is assumed to move at the speed of light while the phase velocity of the $n = 1$ spatial harmonic is slightly subluminal resulting in the dephasing described above. In Fig. 2.2(c) however, the electron is moving slightly below c and remains phased with the spatial harmonic over a longer distance.

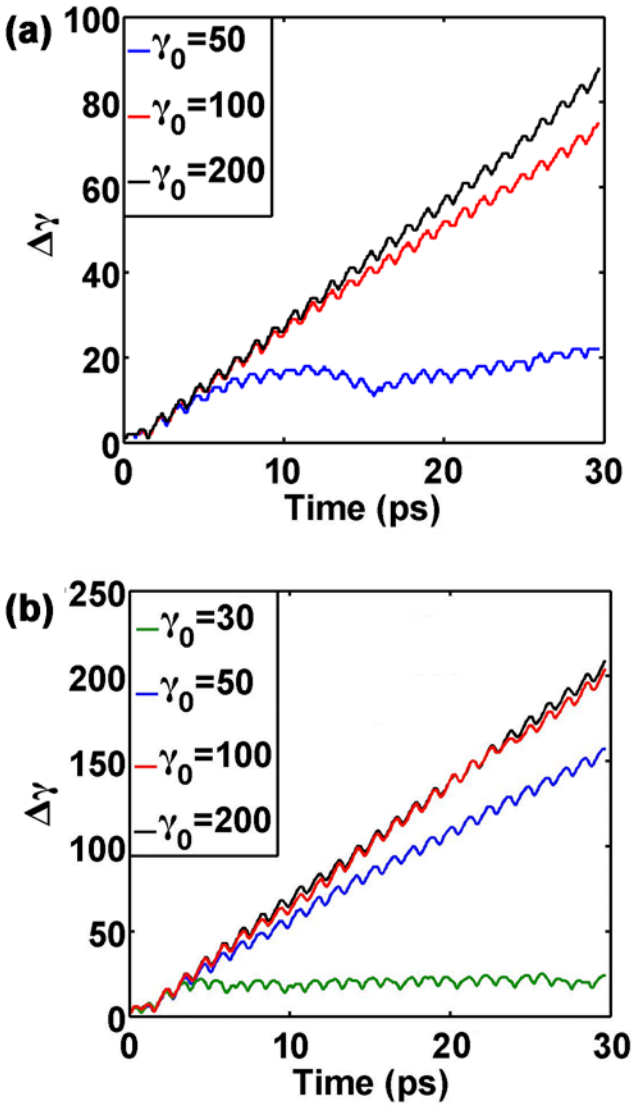

Figure 2.3. Energy gain as a function of acceleration time for different initial electron energies. Here the modulation period is equal to the dephasing length. (a) $\gamma_0 = 50,\ 100,\ and\ 200,$ for $a_0 = 0.1$ (b) $\gamma_0 = 30,\ 50,\ 100,\ and\ 200$ for $a_0 = 0.25$.

Figures 2.3(a) and (b) show simulated energy gains over 9 mm for different initial electron energies at pulse amplitudes of $a_0 = 0.1$ and $a_0 = 0.25$ respectively. The energy gains displayed are those of electrons having the largest energy gain of all the electrons. The energy spectra will be examined below. The red line in both

figures is the result for an initial energy of $\gamma_0 = 100$. Figure 2.3(a) demonstrates energy gain for $\gamma_0 = 100$, but not *linear* energy gain whereas Fig. 2.3(b) shows linear energy gain over the entire 9 mm. This is a result of the threshold energy for trapping in a spatial harmonic

$$\gamma_{th} \approx \left(\frac{k_m w_{ch}}{4\Gamma a_0} \right) \left(\frac{\omega}{\omega_{p,0}} \right)^2 \quad . \tag{2.10}$$

The threshold energy is the minimum energy for electrons to gain energy linearly from the laser field. For $a_0 = 0.1$ and $a_0 = 0.25$ the thresholds are $\gamma_{th} = 183$ and $\gamma_{th} = 73$respectively: $\gamma_0 = 100$ is below the threshold energy for $a_0 = 0.1$, but above for $a_0 = 0.25$. Because it is below threshold the energy gain for $\gamma_0 = 50$ saturates for both $a_0 = 0.1$ and $a_0 = 0.25$. The energy gain of the electrons with initial energy above γ_{th} matches the prediction of the scaling law given in Eq. (2.7). For $a_0 = 0.25$ and an interaction length of 9mm, the scaling law predicts $\Delta\gamma \approx 204$, supported by the simulation results in Fig. 2.3(b).

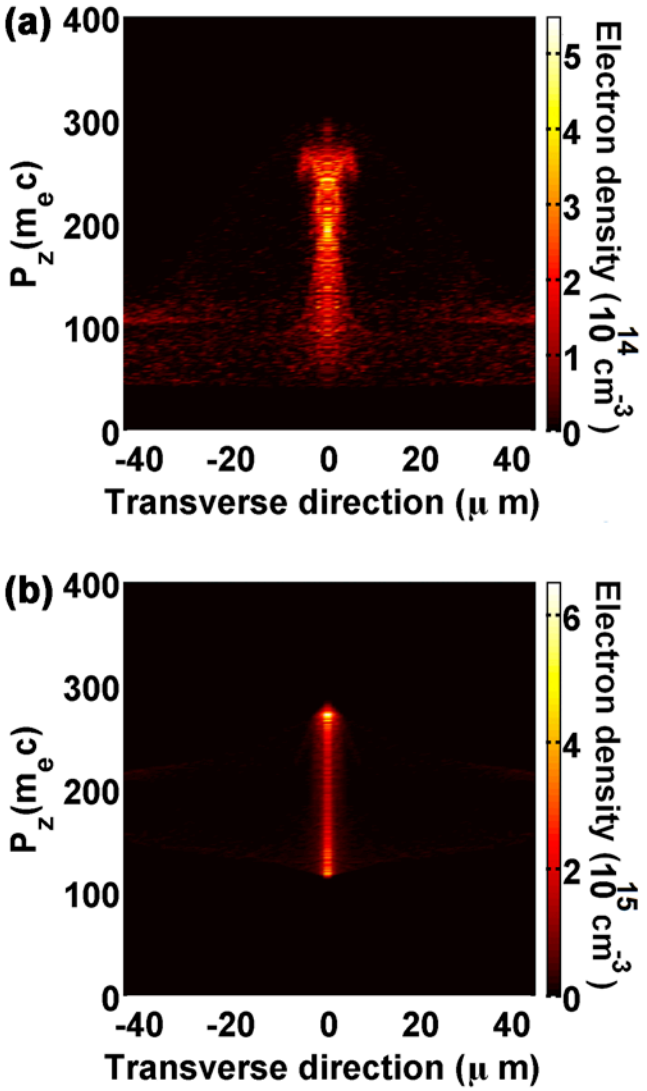

Figure 2.4. Transverse position-longitudinal momentum phase space of the beam electrons after 9 mm acceleration for a beam density, $n_b = 3.5 \times 10^{16}\, cm^{-3}$, (a) $a_0 = 0.25$ and $\gamma_0 = 100$, and (b) $a_0 = 0.1$ and $\gamma_0 = 200$.

To examine the dynamics of the entire beam, we consider phase space densities after 9 mm of interaction for an initial beam density $n_b = 3.5 \times 10^{16}\, cm^{-3}$. Figures 2.4(a) and (b) depict the beam distribution as a function of final longitudinal momentum and transverse position. In Fig. 2.4(a) the laser pulse amplitude is

$a_0 = 0.25$ and the initial electron energy $\gamma_0 = 100$, while in Fig. 2.4(b), $a_0 = 0.1$ and $\gamma_0 = 200$. For both cases, the initial electron energy is above the threshold energy, γ_{th}. Figures 2.4(a) and (b) show that the beam electrons gaining the most energy remain transversely collimated within $5\ \mu m$ of the center. However, electrons that lose or maintain energy scatter significantly for $a_0 = 0.25$. Because electrons are also quasi-phasematched to the transverse fields of the laser pulse, while there is no radial force on axis, electrons slightly off axis can be focused or de-focused depending on their phase. Electrons starting in a defocusing phase will be pushed outward by the phase matched component of the transverse electric field and will not experience significant acceleration. Furthermore, for radii smaller than the spot size, the transverse force increases with radius: as electrons in the defocusing phase move off axis they experience an even larger defocusing force. Of the electrons that start in a focusing phase about half will experience acceleration and half will experience deceleration. This is seen in Figs. 2.4(a) and (b) as electrons that remain collimated on axis but have energies less than $\gamma_0 = 100$ and $\gamma_0 = 200$ respectively. As electrons decelerate they can drop below the threshold energy and begin to phase slip into a defocusing phase with respect to the $n = 1$ spatial harmonic resulting in a scattering of lower energy electrons as seen in Fig. 2.4(a).

In addition to the transverse quasi-phasematched force, there are transverse forces on the beam from the space charge of the beam, the ponderomotive force of the laser pulse on the beam, and the electrostatic potential generated by modification of the background electron density due to the laser pulse and beam. The first two we can rule out: the charge of the beams used in the simulations are 5pC, less than space

charge limit calculated previously, 40pC per bunch [50]. Furthermore, the ponderomotive force on the beam scales as $F_{pm} \propto a_0^2/\gamma$, which because of the inverse proportionality to γ is quite small. We then conclude that the increase in transverse scattering for $a_0 = 0.25$ as opposed to $a_0 = 0.1$ is the combination of two effects: the quasi-phasematched transverse force scales linearly with the pulse amplitude, and the electrostatic forces due to modifications in background plasma scale quadratically with pulse amplitude. The second effect was neglected in previous works [56, 57].

The density perturbation in the background plasma is governed by the combined linearized continuity and momentum equations averaged over the carrier period of the laser pulse:

$$\frac{\partial^2 n_1}{\partial t^2} + \omega_{p,0}^2 n_1 = \frac{1}{4} n_0 c^2 \nabla^2 \left|a_0\right|^2 - \omega_{p,0}^2 n_b \qquad (2.11)$$

where n_0 is the averaged on-axis channel density, $\omega_{p,0}$ is the plasma frequency, a_0 is the normalized laser vector potential, and n_b is the beam density. For very low beam density, using the steady state approximation, and considering a radially polarized pulse the on-axis density perturbation is simply $n_1 \approx \frac{1}{16\pi}(r_e w_{ch}^2)^{-1} a_0^2$, where r_e is the classical electron radius. For $a_0 = 0.1$ and $a_0 = 0.25$ with $w_{ch} = 15\ \mu m$, $n_1 \approx 3.2\times10^{14}\ cm^{-3}$ and $n_1 \approx 2\times10^{15}\ cm^{-3}$ respectively. While this seems small, it actually creates a significant electrostatic force that pushes the beam electrons off axis. Using $\nabla^2\phi_1 = 4\pi e n_1$ and $\vec{F} = e\nabla\phi$ the electrostatic force experienced by the beam electrons is simply $\vec{F}_{es} = \frac{1}{4} m_e c^2 \nabla \left|a_0\right|^2$. The ponderomotive force of the radially

polarized pulse pushes the background electrons towards the center of the channel which deflects off axis beam electrons further off axis. The electrostatic force acting alone creates an unstable equilibrium for small radii, for which a small radial electron velocity will have an early time exponential growth rate of $(2\gamma_0)^{-1/2} a_0 w_{ch}^{-1}$. For $a_0 = 0.25$ and $\gamma_0 = 100$, one e-folding occurs after $0.8\ mm$ while for $a_0 = 0.1$ and $\gamma_0 = 200$ the e-folding distance is $3\ mm$.

The deflection of the beam electrons can be abated by considering the charge of the electron beam. The electron beam pushes the background electrons off axis acting to cancel the ponderomotive force of the laser pulse. From Eq. (2.11) we see that the beam density required to balance the ponderomotive pressure of the laser is $n_b \approx \frac{1}{8\pi}(r_e w_{ch}^2)^{-1} a_0^2$. For $w_{ch} = 15\ \mu m$ and $a_0 = 0.1$, this predicts a balancing density of $n_b \approx 6.3\times10^{14} cm^{-3}$. Figures 2.5(a) and (b) are a comparison of the transverse position, longitudinal momentum phase space densities after 9 mm of interaction for beam densities of $n_b = 7\times10^{10}\ cm^{-3}$ and $n_b = 3.5\times10^{16}\ cm^{-3}$ respectively. The maximum energy gain for both situations is the same, but the higher density beam has better collimation and a more mono-energetic peak.

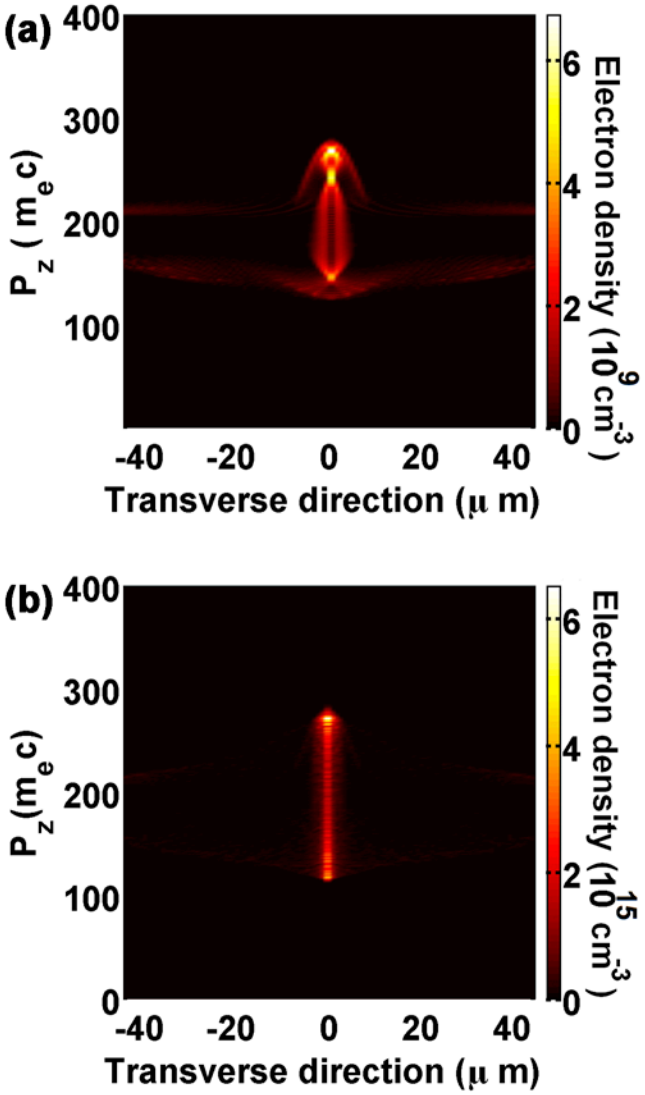

Figure 2.5. Transverse position-longitudinal momentum phase space of the beam electrons after 9 mm acceleration for $a_0 = 0.1$ and $\gamma_0 = 200$ (a) low beam density, $n_b = 7\times10^{10} cm^{-3}$, and (b) high beam density, $n_b = 3.5\times10^{16} cm^{-3}$.

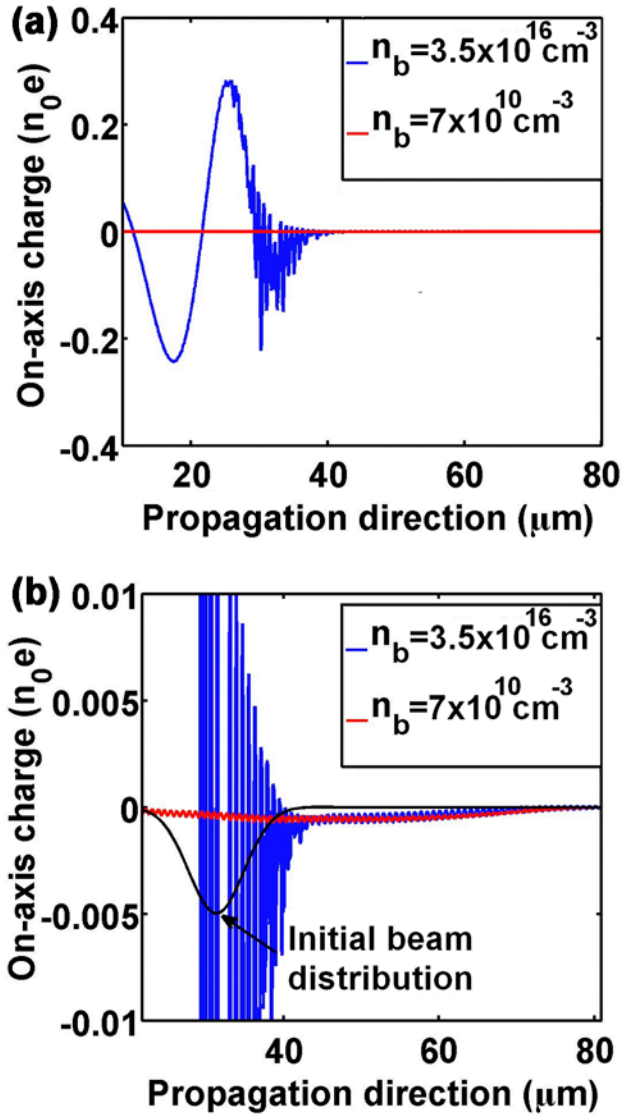

Figure 2.6. On-axis charge density after 4.2 ps of acceleration with $a_0 = 0.1$. (b) vertically magnified image of (a). The blue line is the on-axis charge density for high beam density, $n_b = 3.5 \times 10^{16} cm^{-3}$, and the red line is for low beam density, $n_b = 7 \times 10^{10} cm^{-3}$. The black line in (b) indicates the initial beam electron profile.

Figure 2.6(a) shows the total on axis charge density after 4.2 ps of interaction. The red line is for $n_b = 7 \times 10^{10}\ cm^{-3}$ and the blue line for $n_b = 3.5 \times 10^{16}\ cm^{-3}$. The higher density beam drives a plasma wave in the background plasma whose

associated electric field helps to collimate the beam. The rapid oscillations in the charge density are due to micro-bunching of the beam electrons at the laser wavelength. This is a direct result of the focusing and defocusing phases of the quasi-phasematched transverse field. Figure 2.6(b) is a zoomed in version of (a) and demonstrates the negative charge build-up on axis due to the ponderomotive force of the laser pulse. For the low density beam there is a negative charge buildup overlapping the beam, while for the high density beam there are alternating regions of positive and negative background charge, which on average reduce the deflection of the beam. The electron beam drives out the background electrons, so that positive charge remains. From Fig. 2.5 we see that the accelerating field was not affected by the generation of the plasma wake.

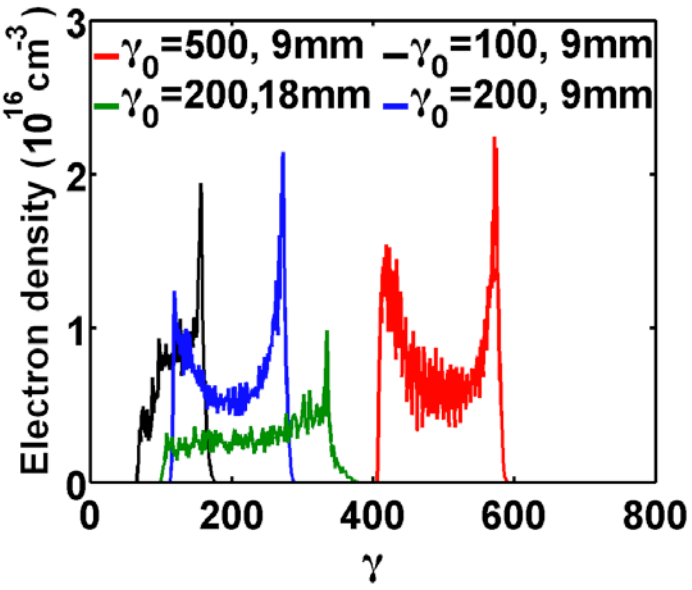

Figure 2.7. Energy spectra of beam electrons for different initial energies: $\gamma_0 = 100,\ 200,\ and\ 500$ after 9mm of acceleration, are the red line, black line, and blue line, respectively, while the green line is $\gamma_0 = 200$ after 18mm acceleration. In all cases the normalized vector potential was $a_0 = 0.1$.

We note that another way to avoid the deflection due to modifications in the background density is to lower the field intensity and propagate over a longer distance. However, lowering the field intensity increases the threshold energy for trapping which may not be ideal.

Figure 2.7 shows the final energy spectrum of the electron beam within the initial radius of the beam for three different initial energies: $\gamma_0 = 100$, $\gamma_0 = 200$, and $\gamma_0 = 500$, accelerated by a laser pulse with $a_0 = 0.1$. The beam electrons are initialized mono-energetically, and the QPM-DLA process maintains a narrow energy spread during acceleration. The relative energy spreads, which we define as $\Delta E / E$ where ΔE is the full width half maximum, for gamma 100, 200, and 500 are 5%, 4%, and 2.8% respectively. Since the phase velocity of the 1st spatial harmonic is set to c, the electrons with higher initial energy will remain in phase with the accelerating field over a longer duration. For example, electrons with a constant energy $\gamma = 100$ will be 450 nm ($\sim \lambda_L / 2$) delayed from an object that moves at c after 9 mm propagation. The dephasing results in more energy spread for the lower initial energy beams.

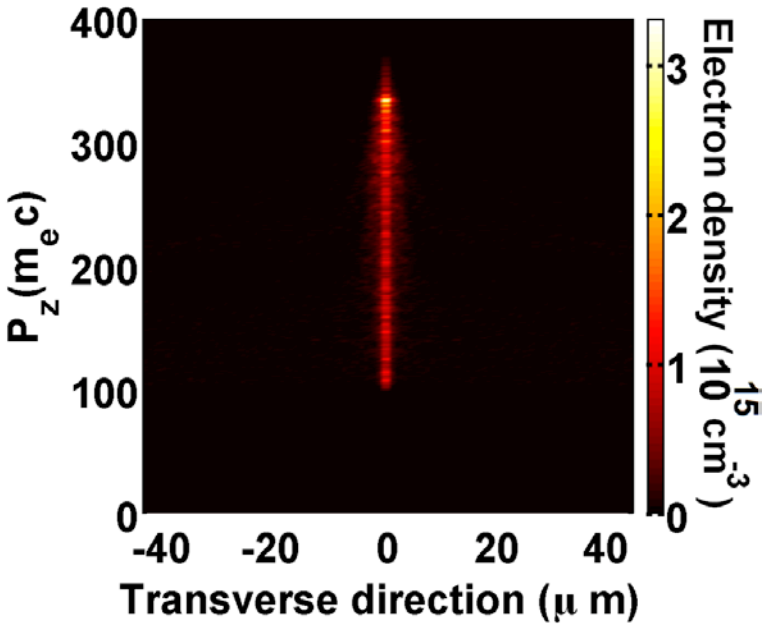

Figure 2.8. Transverse position-longitudinal momentum phase space of the beam electrons after 18mm of acceleration for a beam density, $n_b = 3.5 \times 10^{16} cm^{-3}$, normalized vector potential $a_0 = 0.1$ and initial energy $\gamma_0 = 200$.

The green curve in Fig. 2.7 displays the spectrum when the acceleration occurs over a longer distance: 18 mm for $\gamma_0 = 200$. The energy spread of the peak has dropped from 4% at 9mm to 1.5% at 18 mm, and the energy of the peak has increased. However, the mono-energetic peak no longer occurs at the maximum in the spectrum. Figure 2.8 shows the transverse position, longitudinal momentum phase space density after 18 mm.

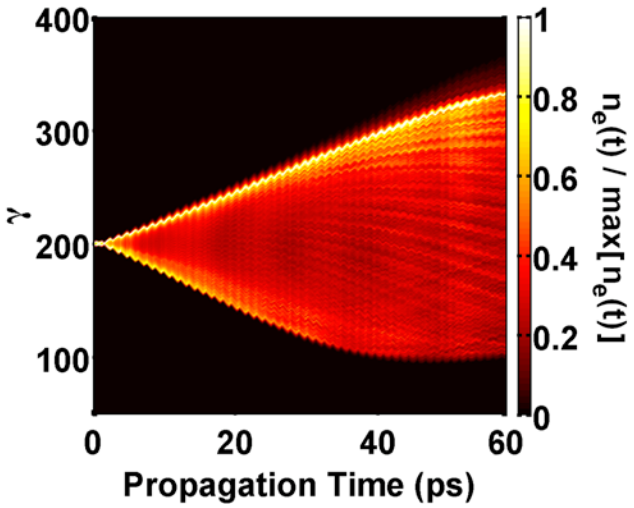

Figure 2.9. Energy spectrum as a function of time for $n_b = 3.5\times10^{16} cm^{-3}$, $a_0 = 0.1$ and $\gamma_0 = 200$. For clarity the spectrum is normalized to its maximum at each time.

The beam electrons remain collimated in the transverse direction and the mono-energetic peak in Fig. 2.8 appears as the bright dot near $\gamma = 330$. The time evolution of the energy spectrum appears in Fig. 2.9. For clarity the spectrum has been normalized by the peak value at each time step. The orange line with narrow width is the mono-energetic peak. It starts as a very narrow peak and slowly broadens until 25ps, and becomes narrow again afterward.

2.4 Low energy electron acceleration

The electron beams simulated thus far have been initialized with relativistic speeds to ensure that the electrons remain phase matched to the $n=1$ spatial harmonic. This is not favorable for small scale, table top laser accelerators because it requires a preliminary accelerator for injection. Thus a method for injecting low energy electrons is critical for the realization of QPM-DLA as a small scale

accelerator. The minimum energy of electrons in QPM-DLA can be calculated via Eq. (2.10). To trap low energy electrons from the beginning and accelerate them over the entire acceleration distance requires field amplitudes for which the interaction between the laser pulse and background plasma becomes nonlinear, potentially destroying the slow wave structure. For example, to trap and accelerate electrons with $\gamma_0 = 20$ requires a laser pulse with a relativistic amplitude, $a_0 = 0.92$. Alternatively, quasi-phasematching to low energy electrons can be achieved by gradually ramping up the phase velocity of the phase matched spatial harmonic over the interaction length. Increasing the phase velocity can be done in several ways: increasing the electron density, increasing the modulation period, or decreasing the channel width. Here we investigate ramping the electron density.

We begin by analytically calculating the density ramp required for a particular initial electron energy. We write the density profile in terms of the plasma frequency as follows:

$$\omega_p^2(r,z) = \omega_{p0}^2 + \omega_{p1}^2(z) + \Gamma\omega_{p0}^2 \sin(k_m z) + \frac{4c^2 r^2}{w_{ch}^4}, \qquad (2.12)$$

where the density ramp is included in the function $\omega_{p1}^2(z)$. The total wave vector for the first spatial harmonic is then $\hat{k} = k_0 + k_m + \delta k - \frac{1}{2}k_0^{-1}k_{p1}^2(z)$. The goal now is to find an expression for $k_{p,1}^2(z)$ such that the energy gain is linear over the interaction length. Using $\Delta\gamma = -q/m_e c^3 \int \vec{v}\cdot\partial_t \vec{A} dt$ the energy gain is

$$\frac{d\gamma}{dz} = k_0 \hat{a}_0 e^{i\int \hat{k} dz - i\omega_0 t}, \qquad (2.13)$$

where we have defined $\hat{a}_0 \equiv 4(k_0 w_{ch})^{-1} J_1(\psi) a_0$. For linear energy gain we require $\int \hat{k} dz - \omega_0 t = 0$, which upon differentiation with respect to z provides $\hat{k} = \omega_0 / \mathrm{v}(z)$. Furthermore, we can integrate Eq. (2.13) to find $\gamma = \gamma_0 + \hat{a}_0 k_0 z$, which allows us to find $\mathrm{v}(z)$. Putting everything together we find the ideal density ramp for a given initial energy is given by

$$k_{p1}^2(z) = 2k_0(k_0 + k_m + \delta k) - 2\left[\frac{(\gamma_0 + \hat{a}_0 k_0 z)^2}{(\gamma_0 + \hat{a}_0 k_0 z)^2 - 1}\right]^{1/2} k_0^2, \quad (2.14)$$

and the total wavevector for the $n = 1$ spatial harmonic is simply

$$k = \left[\frac{(\gamma_0 + \hat{a}_0 k_0 z)^2}{(\gamma_0 + \hat{a}_0 k_0 z)^2 - 1}\right]^{1/2} k_0. \quad (2.15)$$

Care must still be taken to ensure that the total density is not less than zero, for which a sufficient condition is $(1-\Gamma)k_{p0}^2 + k_{p1}^2(z = \frac{3\pi}{2}) > 0$.

Based on the analytical solution for the density ramp, we performed 2D cylindrical PIC simulations to investigate the trapping of low energy electrons by the laser pulse. The simulations were conducted for electrons with initial energies of $\gamma_0 = 20$ and $\gamma_0 = 50$, both of which are below the critical energy for $a_0 = 0.1$. Figure 2.10(a) shows the on-axis channel density for acceleration of electrons with $\gamma_0 = 20$. The value of n_0 is $2.3 \times 10^{19}\ cm^{-3}$ an increase over the value used in the previous simulations, $7 \times 10^{18} cm^{-3}$. Accordingly, the modulation period is reduced to $117 \mu m$ to meet the positivity condition on the density. Note the gradual increase of the averaged density over the propagation distance.

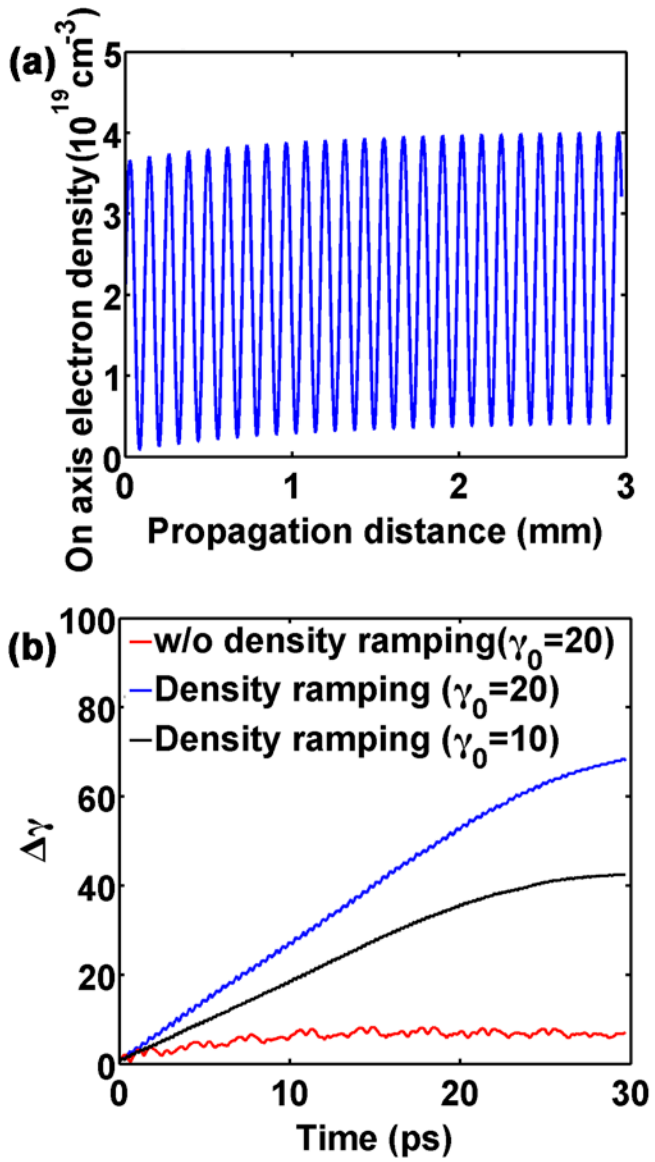

Figure 2.10. (a) On axis electron density for a plasma waveguide with a density ramp. The ramp allows trapping of lower energy electrons in this case $\gamma_0 = 20$ for a normalized vector potential of $a_0 = 0.1$. (b) Energy gain of $\gamma_0 = 20$ electrons with (blue) and without (red) the density ramp pictured in (a). The energy gain of $\gamma_0 = 10$ electrons is black line in (b).

In Fig. 2.10(b), a comparison of the energy gain of electrons with $\gamma_0 = 20$ with (blue) and without (red) the density ramp is displayed. As before, the energy gains displayed are those of electrons having the largest energy gain of all the electrons. The figure demonstrates a clear improvement of trapping electrons with below threshold energy in the presence of a density ramp. The energy gain slows down after 22 ps of interaction, because the electrons have outrun the laser pulse: the increase in average channel density decreased the group velocity of the laser pulse. The energy gain of electrons with $\gamma_0 = 10$ (black) is also displayed in Fig. 2.10(b). For electrons with $\gamma_0 = 10$, the same parameters for the laser and the channel were used except the laser pulse duration was increased to 600 fs, since higher density ramp is required for $\gamma_0 = 10$ than $\gamma_0 = 20$, which makes the group velocity of the laser pulse slower. While more simulations are needed to examine the robustness of the density ramp, these results show that in principle structuring the plasma density can aid in the acceleration of low energy electrons.

2.5 Conclusions

In summary, this work examines QPM-DLA in a corrugated plasma waveguide with fully self-consistent 2D, cylindrical PIC simulations. The PIC code TurboWAVE was validated by verifying the existence of spatial harmonics created by density modulations in the plasma channel. Fourier transforming the laser field yielded axial harmonics whose amplitude ratios matched analytic calculations. The

local phase of the field was extracted and found to follow the density modulations as expected.

The simulations demonstrate linear acceleration of electrons by the phase matched longitudinal electric field. The simulated acceleration gradients were ~ $110\,MeV/cm$ for $a_0 = 0.25$ and ~ $50\,MeV/cm$ for $a_0 = 0.1$, matching well with analytic predictions. Simulations also corroborated that a threshold energy exists for the trapping and linear energy gain of electrons in a spatial harmonic. Energy spectra of accelerated electron exhibited mono-energetic peaks ($\Delta E/E \approx 3 \sim 5\%$) depending on the initial energy of the electron beam and acceleration distance. $\Delta E/E$ remains more less constant over 1.8cm interaction.

The simulations revealed that the ponderomotive force due to the laser field plays a role in deflecting electrons in the accelerating phase, a result neglected in previous work [57]. The ponderomotive force of the transverse field pushes plasma channel electrons towards the axis. The resulting transverse electrostatic field defocuses the electron beam. This effect becomes more deleterious at higher pump intensity due to the increase in ponderomotive force. The defocusing was successfully mitigated by increasing the charge of the electron beam. With higher beam charge, the electron beam pushes the plasma channel electrons off axis counteracting the laser ponderomotive force.

We extended our basic model of QPM-DLA for highly relativistic electrons to the phase-matching of lower energy electrons. An electron density ramp was used to slowly increase the phase velocity of the phase matched spatial harmonic over the interaction length. An analytic expression for an ideal density ramp was determined

and implemented in the PIC simulations. Simulations with the density-ramped modulated waveguides showed trapping of electrons with $\gamma_0 = 20$ at a pump intensity of $a_0 = 0.1$. No electron energy gain was seen without the density ramp. Alternative methods for accelerating low energy electrons include increasing the modulation period or narrowing the channel over the interaction length. These will be topics of future study.

Chapter 3: Quasi-phasematched laser wakefield acceleration

3.1 Introduction

In the last chapter, quasi-phasematching in a corrugated plasma waveguide has been shown to enable continuous acceleration of electrons by the copropagating laser field in a plasma channel, where the net energy gain of electrons would otherwise be impossible due to the superluminal phase velocity of the laser field in plasma. Here, the same methodology is applied to the LWFA for the acceleration of electrons over many dephasing lengths, the distance over which the accelerated electrons outrun the accelerating phase of the wakefield, and which has been considered a fundamental gain limit.

Here we investigate the application of QPM in modulated plasma channels to LWFA (QPM-LWFA).The frequency of the excited plasma wave, and consequently its phase velocity, undergoes oscillations in the modulated plasma. As a result, the plasma wave itself is composed of spatial harmonics. By matching the modulation period to the dephasing length, a relativistic electron can undergo energy gain over several dephasing lengths. Furthermore, QPM-LWFA can operate at much lower pulse energies and provides a guiding structure for the laser pulse, thus loosening the three energy gain limitations associated with standard LWFA: dephasing, depletion, and diffraction.

3.2 Theory

We start by examining the electrostatic fields of ponderomotively driven plasma waves in a corrugated plasma channel. The density profile of the plasma is modeled as $n_e(r,z) = n_0[1+\delta\sin(k_m z)] + \frac{1}{2}n_0'' r^2$, where n_0 is the average on axis density, δ is the modulation amplitude, $k_m = 2\pi/\lambda_m$ is the wavenumber associated with modulations of period λ_m, and n_0'' describes the curvature of the channel. The transverse parabolic density profile provides guiding for a laser pulse with a *exp*(-1) field radius $w_{ch} = (2c)^{1/2}(m_e/2\pi e^2 n_0'')^{1/4}$, where c is the speed of light in vacuum, and m_e and e are the electron rest mass and charge.

To illustrate the concept and to derive a scaling for the energy gain, we consider a weakly relativistic laser pulse propagating along the z-axis with wavelength $\lambda_0 = 2\pi/k_0$ and normalized vector potential, $\mathbf{a} = e\mathbf{A}/m_e c$. As the laser pulse propagates through the plasma, its ponderomotive force drives an electron plasma wave with a phase velocity equal to the group velocity of the laser pulse. Using a separation of time scales based on the disparity between the laser pulse and plasma frequencies, the equation for the wakefield in a non-uniform plasma is found from the fluid and Maxwell's equations:

$$\left[\frac{\partial^2}{\partial\xi^2} + k_p^2(r,z)\right]\mathbf{E} = -\pi e n_e(r,z)\nabla|\mathbf{a}|^2 \qquad (3.1)$$

where $k_p^2 = \omega_p^2/c^2 = 4\pi e^2 n_e/m_e c^2$, and $\xi = z - \mathrm{v}_g t$ is the coordinate in a frame moving with the group velocity, v_g, of the laser pulse. We are interested in the case of $\delta << 1$ such that v_g is essentially constant, namely $\mathrm{v}_g/c \approx 1-(k_p^2/2k_0^2)-(4/k_0^2 w_{ch}^2)$ where $k_{p0}^2 = \omega_{p0}^2/c = 4\pi e^2 n_0/m_e c^2$.

We assume a laser pulse of the form $|\mathbf{a}(\xi,r)|^2 = a_0^2\exp(-2r^2/w_{ch}^2)\sin^2(\pi\xi/c\sigma)$ on the domain $0<\xi<c\sigma$ with temporal full width half maximum (FWHM) $\sigma_{FWHM} = \sigma/2$ matched to the on-axis plasma

period, $\sigma_{FWHM} = \pi / \omega_{p0}$. For $\delta << 1$, the wakefields close to the axis, $r^2 << w_{ch}^2$, and after the laser pulse, $\xi > c\sigma$, are

$$E_z = -\frac{\pi}{8} a_0^2 \sum_n J_n \left[\frac{\delta k_{p0} (\mathrm{v}_g t - z)}{2} \right] \cos\left[k_{p0} \mathrm{v}_g t - (n k_m + k_{p0}) z \right] \qquad (3.2a)$$

$$E_r = -\frac{a_0^2}{2 k_{p0} w_{ch}} \left(\frac{r}{w_{ch}} \right) \sum_n J_n \left[\frac{\delta k_{p0} (\mathrm{v}_g t - z)}{2} \right] \sin\left[k_{p0} \mathrm{v}_g t - (n k_m + k_{p0}) z \right] \qquad (3.2b)$$

where the fields have been normalized to the wave breaking field, $m_e c \omega_{p0} / e$. Equation (3.2) exhibits the decomposition of the wakefields into spatial harmonics whose amplitudes depend on the distance behind the head of the laser pulse, and whose phase velocities depend on the modulation period.

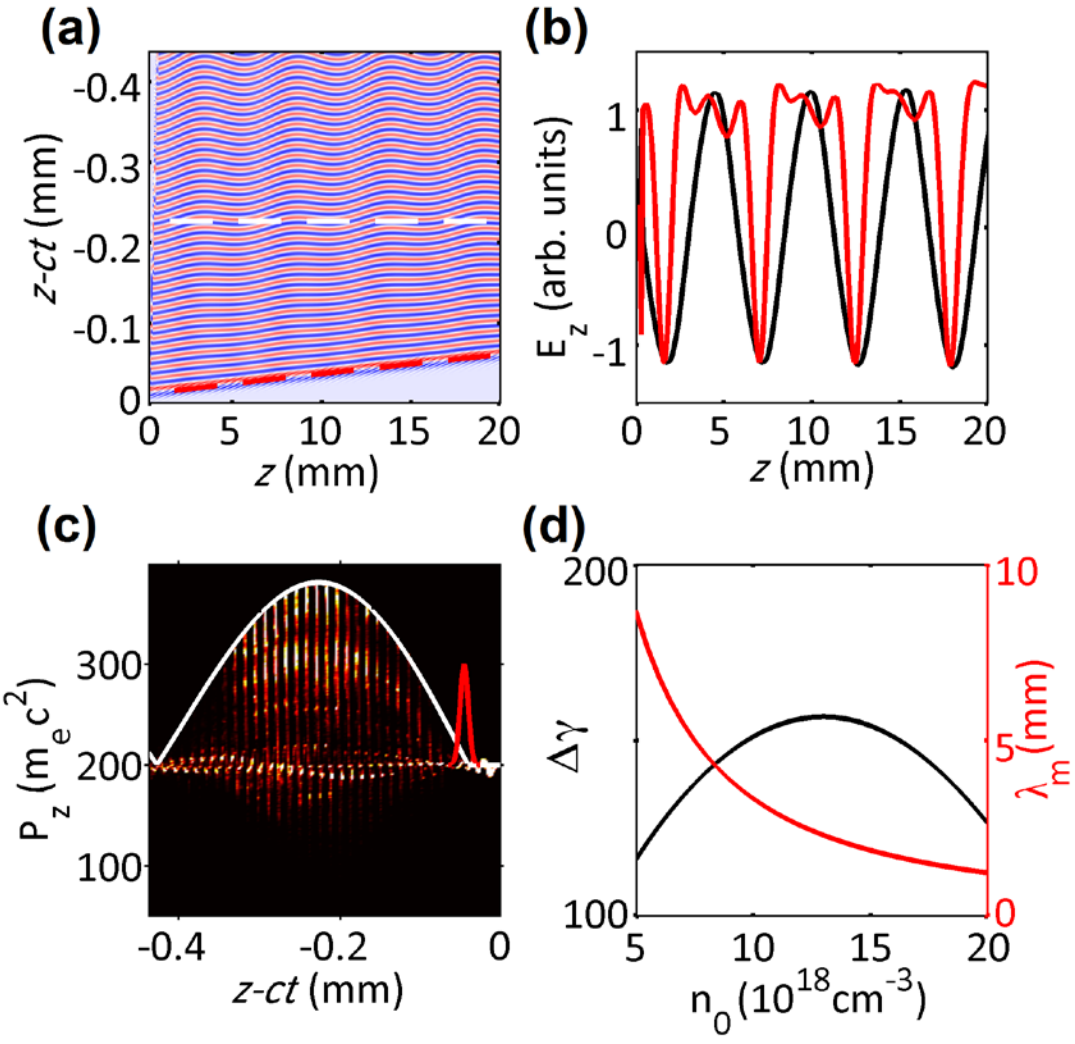

Figure 3.1. (a) On-axis wakefield in a modulated plasma as a function of speed of light frame coordinate, $z-ct$, and axial distance, z. The wavy lines are the plasma wakefield phase fronts, while the red dashed line marks the path of the on-axis peak of the (~10 μm long) laser pulse (b) Axial wakefield experienced by an electron moving with an axial velocity near the speed of light at a position marked by the white dashed line in (a). The red and black lines are the fields experienced in a modulated and uniform plasma channel respectively. (c) Phase space density in the axial momentum-speed of light frame plane after 2 mm of interaction. The white line shows the amplitude of the $n=-1$ spatial harmonic and the red line the envelope of the laser pulse. (d) Predicted energy gain, black, left vertical axis and matched modulation period red, right vertical scale as a function of average on-axis plasma density. Exact parameters are in the text.

Figure 3.1(a) shows the on-axis longitudinal electric field, E_z, of a plasma wave driven by a low-amplitude, $|\mathbf{a}|<<1$, $\lambda_0 = 800\ nm$ laser pulse as a function of $z-ct$ and z in a corrugated plasma channel with $n_0 = 7\times10^{18}\ cm^{-3}$, $\delta = 0.04$,

$w_{ch} = 15\ \mu m$, and $\lambda_m = 5.0\ mm$. The pulse duration and spot are matched to the density and channel curvature respectively. The wavy lines are the plasma wakefield phase fronts, while the red dashed line marks the path of the on-axis peak of the (~10 μm long) laser pulse. The pulse slides back in the speed of light frame because $v_g < c$. In a uniform channel, the phase fronts are parallel to the group velocity trajectory. In a corrugated channel, the pulse passes through oscillating plasma density, causing the wake phases to oscillate with respect to the pulse trajectory.

From Eq. (3.2), the phase velocity, $v_{p,n}$, of the wakefield's n^{th} spatial harmonic is

$$\frac{v_{p,n}}{c} \approx 1 - \frac{k_{p0}^2}{2k_0^2} - \frac{4}{k_0^2 w_{ch}^2} - n\frac{k_m}{k_{p0}}. \qquad (3.3)$$

The phase of the n^{th} spatial harmonic can be made stationary in the speed of light frame by setting the modulation period to $\lambda_m = -2n\lambda_{p0}^3 \lambda_0^{-2}(1 + 8/k_{p0}^2 w_{ch}^2)^{-1}$ where $\lambda_{p0} = 2\pi / k_{p0}$. For the $n = -1$ spatial harmonic, this is equivalent to setting the modulation period equal to the dephasing length, $L_d = 2\lambda_{p0}^3 \lambda_0^{-2}(1 + 8/k_{p0}^2 w_{ch}^2)^{-1}$, of standard LWFA. When $\lambda_m = L_d$ an electron moving near the speed of light along the channel axis experiences a near constant axial acceleration from the $n = -1$ spatial harmonic, while the acceleration of all other spatial harmonics time averages to zero.

The red curve of Fig. 3.1(b) is a lineout along the white dashed curve of Fig. 3.1(a), in which $\lambda_m = L_d$. For comparison, the black curve is a similar lineout for an unmodulated plasma channel. These curves show the longitudinal wakefield acting on an electron moving at nearly *c*. In both cases the dominant axial field oscillates at the plasma period, but the oscillations in the modulated channel clearly contain additional harmonics. While the integral of the axial field over a plasma period is zero in the uniform channel, it is non-zero in the modulated channel, showing that the modulated wakefield performs net work on a relativistic electron even after the electron has traversed a full plasma wavelength.

In Fig. 3.1(c) the phase space of axial momentum, P_z, and speed of light frame coordinate is plotted for a long, uniform beam of test electrons with initial axial

momentum of 100 MeV/c accelerated over 2cm. The results were obtained from 2D particle-in-cell simulations which we discuss further below. The pulse amplitude, wavelength, and FWHM were $a_0 = 0.25$, $\lambda_0 = 800\ nm$, and $\sigma_{FWHM} = 30\ fs$ respectively, and the density parameters were the same as given above. The red curve indicates the location of the laser pulse propagating to the right in the figure and the white curve indicates the normalized amplitude of the $n = -1$ spatial harmonic, J_{-1}. The plot clearly shows that axial momentum gain is proportional to the amplitude of the phase matched spatial harmonic. The spikes in momentum result from bunching of the positively accelerated electrons in each half-period of the plasma wave.

The energy gain of a relativistic electron accelerated by the phase matched harmonic can be found by integrating $d\gamma/dt = -\omega_{p0}(\mathrm{v}_z/c)E_z$, where $\gamma = [1 + \mathbf{P}\cdot\mathbf{P}/m_e^2c^2]^{1/2}$ is the electron's relativistic factor. Using Eq. (3.2a) and setting $\lambda_m = L_d$, we find

$$\Delta\gamma(z) \approx \frac{1}{4}\pi a_0^2 \delta^{-1} \frac{k_{p0}}{k_m}\left[J_0\left(\frac{1}{2}\delta k_m z + \frac{1}{2}\delta k_{p0} z_0\right) - J_0\left(\frac{1}{2}\delta k_{p0} z_0\right)\right], \quad (3.4)$$

where z_0 is the initial axial position of an electron and the pulse is initially peaked at $z = 0$. The energy gain increases with the laser amplitude through the larger wakefields driven by the pulse. As expected, $\Delta\gamma(z) \to 0$ as $\delta \to 0$ or $k_m \to 0$: only the $n = 0$ spatial harmonic is present in this limit. The maximum acceleration will occur for electrons with initial axial positions near the peak of the $n = -1$ spatial harmonic, $\delta k_{p0} z_0 \sim -4$. The value for δ is, however, limited: aside from experimental considerations such as density uniformity, the peak of J_{-1} must occur within the length of the plasma channel, L_{ch}, such that δ can be no smaller than $\delta_{\min} \sim 4/k_{p0}L_{ch}$. For $L_{ch} = 2\ cm$ and $n_0 = 7\times10^{18}\ cm^{-3}$, $\delta_{\min} = 4\times10^{-4}$, much smaller than the value of $\delta = 0.04$ used here.

The energy gain in QPM-LWFA is eventually limited by electrons outrunning the spatial harmonic envelope, the white curve in Fig. 3.1(c), or pulse evolution and depletion. One can show that for $n = -1$ and $\delta >> \delta_{\min}$, the length scale for harmonic

envelope dephasing is $L_{-1} = 0.6\delta^{-1}L_d$ for an electron starting at $z_0 \sim -4/\delta k_{p0}$. For $\delta = 0.04$, $L_{-1} = 15L_d$, an order of magnitude larger than standard LWFA. Based on L_{-1}, the maximum energy gain of QPM-LWFA is $\Delta\gamma_{Q,\max} \approx (1/8)[1 - J_0(2)]a_0^2\delta^{-1}k_{p0}L_d$. Due to the approximate conservation of wave action [73], the pulse depletion length and the length scale for spectral red-shifting-induced pulse shape modifications are nearly equal: $L_{dep} \approx L_d a_0^{-2}$ [22]. By setting $L_{dep} = L_{-1}$, we can estimate the maximum amplitude and energy gain for QPM-LWFA: $a_{0,\max} \approx 2.6\delta^{1/2}$ and $\Delta\gamma_{Q,\max} \approx (7/8)[1 - J_0(2)]k_{p0}L_d$. For $\delta = 0.04$ this gives $a_{0,\max} \approx 0.5$ and $\Delta\gamma_{Q,\max} \approx 170$, using our earlier parameters. For the same parameters in a uniform plasma, the dephasing-limited energy gain of LWFA is $\Delta\gamma_{LWFA} = (\pi/16)a_0^2 k_{p0}L_d \sim 34$. For both QPM-LWFA and LWFA the maximum electron energy gain can be increased by lowering the plasma density. We note that $\Delta\gamma_{Q,\max}$ underpredicts the energy gain observed in Fig. 3.1(c). This is somewhat surprising as the FWHM used for Fig. 3.1(c) is longer than the matched value used for deriving Eq. (3.4). As we will see, an enhancement in energy gain results from the nonlinear compression of the laser pulse.

Figure 3.1(d) displays the modulation period required for phasematched acceleration by the $n = -1$ spatial harmonic and the energy gain after 2 cm as a function of plasma density for $\delta = 0.04$. The energy initially increases because the wakefield amplitude increases with plasma density, and then decreases. The decrease in energy results from the shortening of the maximum acceleration length due to the inverse density dependence $k_{p0}L_{-1} \propto n_0^{-1}$.

Our estimate of the energy gain assumed that the electron's axial velocity was close enough to *c* that it did not undergo sufficient phase-slippage with respect to the $n = -1$ spatial harmonic. A condition on the minimum axial momentum for which this assumption is valid, or trapping condition, can be derived from the Hamiltonian of an

electron interacting with the $n=-1$ spatial harmonic. Using $d\gamma/dt=-\omega_{p0}(\mathrm{v}_z/c)E_z$ and defining $\Phi=k_{p0}\mathrm{v}_g t-(k_{p0}+k_m)z$, the Hamiltonian takes the form

$$H=\frac{1}{8}\pi a_0^2 J_1(2)\sin(\Phi)-\left(\frac{\mathrm{v}_g}{c}\right)(\gamma^2-1)^{1/2}+\left(1-\frac{k_m}{k_{p0}}\right)\gamma, \qquad (3.5)$$

where Φ and γ are the conjugate dynamical variables and the electron is assumed to be located near the peak of the spatial harmonic during the trapping process: $J_1[\delta k_{p0}(\mathrm{v}_g t-z)/2]\sim J_1(2)$. Setting $k_m=2\pi/L_d$ and using the fact that H is a constant of the motion, we find the threshold energy for trapping is $\gamma_{tr,Q}\approx[4J_1(2)E_{\max}]^{-1}$, where $E_{\max}=\pi a_0^2/8$. For $a_0=0.25$, this predicts a trapping threshold of $\gamma_{tr,Q}\approx 18$. For standard LWFA in the linear regime the trapping threshold is given by $\gamma_{tr,S}/\gamma_g\approx(1+\gamma_g E_{\max})-[(1+\gamma_g E_{\max})^2-1]^{1/2}$ where $\gamma_g=(1-\mathrm{v}_g^2/c^2)^{-1/2}$ [74]. With the parameters specified earlier, this predicts $\gamma_{tr,S}\approx 7$. The increased trapping threshold of QPM-LWFA can be overcome with additional density tailoring to modify the plasma wave's phase velocity and other injection techniques [27, 33, 34, 75, 76].

3.3 Particle-In-Cell simulations

Particle-in-cell (PIC) simulations of quasi-phasematched laser wakefield acceleration were performed using TurboWAVE, fully described elsewhere [62]. The fields, particle trajectories, densities and currents were calculated on a 2D planar-Cartesian grid in a window moving at *c*. The window dimensions were $77\ \mu m\times 438\ \mu m$ with 512×16384 cells in the transverse, x, and longitudinal, $z-ct$, directions. The plasma density was ramped up over $200\ \mu m$. After the initial ramp, the plasma density followed $n_e(x,z)=n_0[1+\delta\sin(k_m z)](1+n_0'' x^2/2)$ with $n_0=7\times 10^{18}\ cm^{-3}$, n_0'' set to guide a linearly polarized Gaussian mode with a $1/e$ field radius $w_{ch}=15\ \mu m$, $\delta=0.04$, and $\lambda_m=L_d=5.0\ mm$.

The laser pulse was initialized with linear polarization in the x-direction, a sine-squared temporal profile, and a Gaussian transverse profile, with the same parameters as above. The simulations were conducted for pulse amplitudes of $a_0 = 0.25\,(0.5\ \text{TW})$ $a_0 = 0.375\,(1.1\ \text{TW})$, and $a_0 = 0.5\,(1.9\ \text{TW})$: pulse energies of only $14\ mJ$, $32\ mJ$, and $56\ mJ$. The pulse started with its front edge at the beginning of the plasma. An electron bunch of initial axial momentum $P_z / m_e c = 30$, and transverse and longitudinal Gaussian profiles with 1/*e* radii of $4\ \mu m$ and $8\ \mu m$, was initialized with its center $4 / \delta k_{p0} = 200 \mu m$ behind the peak of the laser pulse. The peak bunch density was $n_b = 3.5 \times 10^{16}\ cm^{-3}$ with a total charge of $11\ pC$, parameters typical of LWFA experiments [77]. We note that because the laser mode is channel guided and the pulse powers are lower than the critical power for self-focusing [19], $P_{cr} = 17(\omega / \omega_{p0})^2 GW = 4.2\ TW$, differences between our 2D simulations and full 3D simulations are minimal.

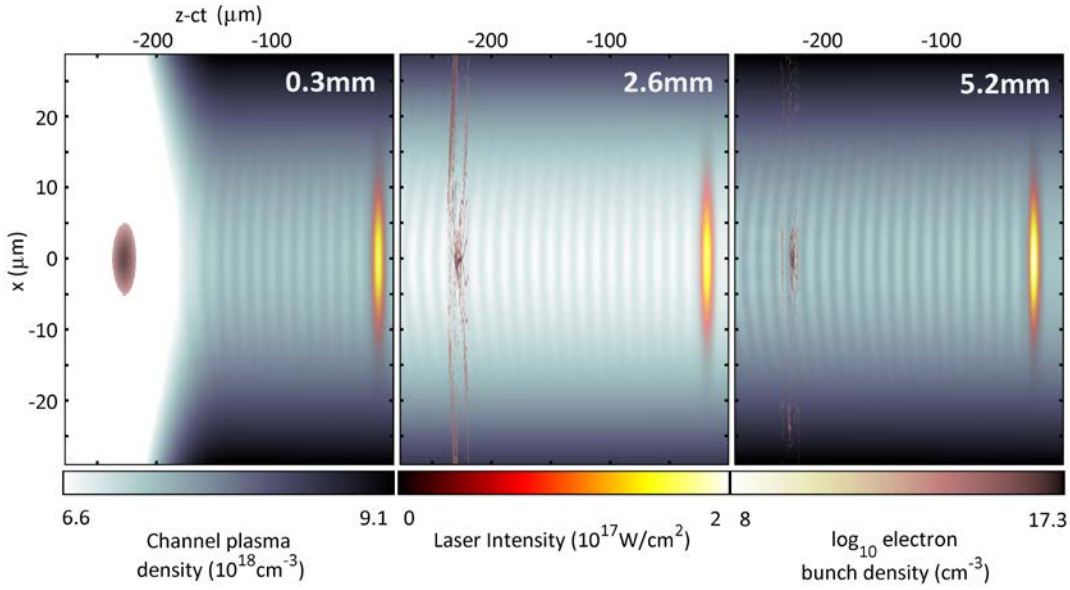

Figure 3.2. Background plasma density, laser pulse intensity, and electron bunch density as a function of transverse position and speed of light frame coordinate at three axial distances: $0.3\ mm$, $2.6\ mm$, and $5.2\ mm$ for $a_0 = 0.25$. The electron plasma wave is noticeable as the ripples in the background plasma density.

Figure 3.2 displays snapshots of background plasma density, laser intensity, and electron bunch density at propagation distances of $0.3\ mm$, $2.6\ mm$, and

5.2 *mm* for the $a_0 = 0.25$ pulse. The laser pulse enters the plasma channel and excites a plasma wave, visible as the density oscillations trailing the pulse. As the bunch electrons enter the channel, they evolve in response to the wakefields. By 2.6 *mm* the bunch electrons have been either laterally deflected or strongly focused. The transverse field of the $n = -1$ spatial harmonic is also quasi-phasematched to the electrons. For off-axis electrons, the quasi-phasematched transverse field provides either focusing or defocusing depending on the electron's initial longitudinal position. Comparing E_z and E_r in Eq. (3.2), we see that there are longitudinal regions of size $\lambda_p / 4$ where electrons are both axially accelerated and focused. Electrons starting in these favorable regions remain on axis and continue to gain energy as they travel behind the laser pulse.

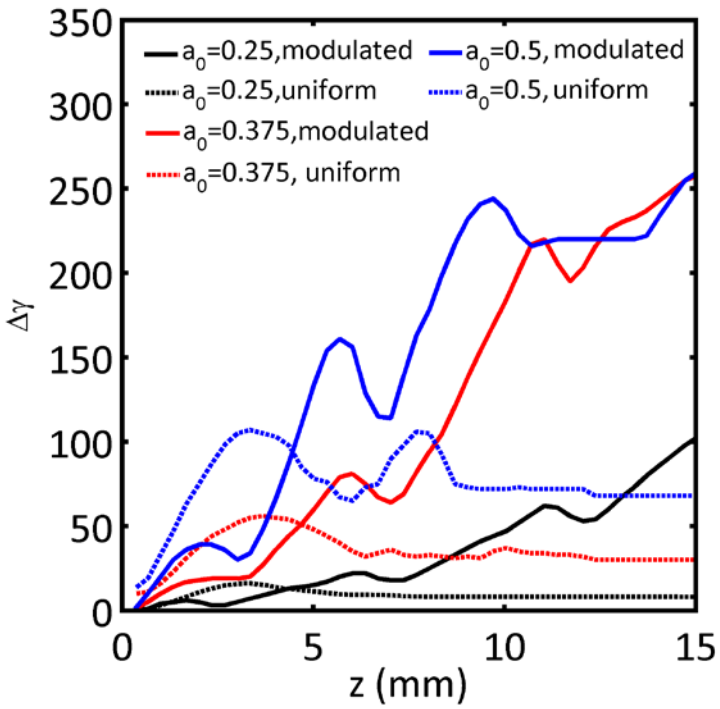

Figure. 3.3. Maximum energy gain as a function of distance for electrons with initial axial momentum $P_z / m_e c = 30$ accelerated in a modulated, solid, and uniform channel, dashed. The black, red, and blue lines are for initial pulse amplitudes of $a_0 = 0.25$, $a_0 = 0.375$, and $a_0 = 0.5$ respectively.

Comparisons of the maximum energy gain resulting from QPM-LWFA and standard LWFA are shown in Fig. 3.3. When the modulation period is matched to the dephasing length, $\lambda_m = L_d$, electrons gain energy over several dephasing lengths. In a uniform channel, the electrons initially gain energy, but then lose energy as they outrun the accelerating phase of the wake. The energy oscillations in the modulated channel result from the partial de-acceleration of electrons as they 'bucket jump' [78] into the next phase of the plasma wave. After $1.5\ cm$, the energy gain reaches $\Delta E \sim 51\ MeV$ for $a_0 = 0.25$, and $\Delta E \sim 130\ MeV$ for $a_0 = 0.375$, but saturates at $\Delta E \sim 130\ MeV$ for $a_0 = 0.5$, consistent with our earlier estimate of $a_{0,\max}$. When $a_0 = 0.5$, nonlinear boring of the plasma density causes the pulse width to oscillate irregularly. As a result, the phase velocity of the plasma wave, and hence the dephasing length become non-stationary. The energy gain saturation can be mitigated by varying the modulation period along the channel or by choosing a pulse profile whose spot size varies in time [79].

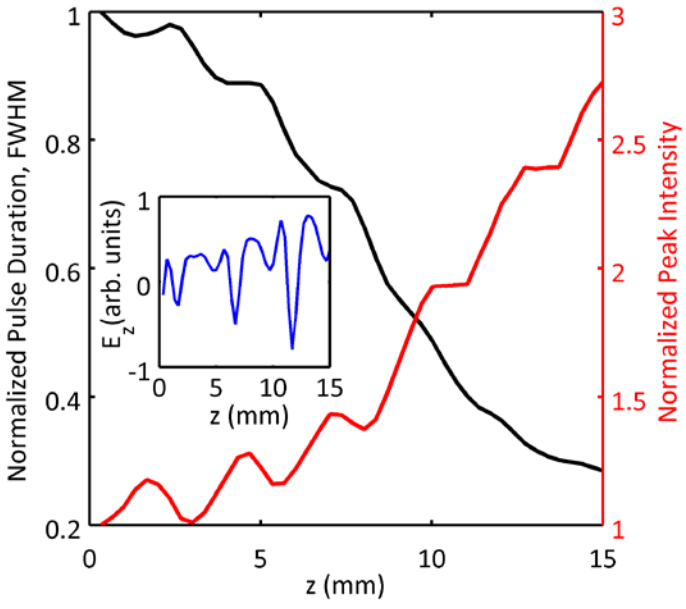

Figure. 3.4. On-axis temporal FWHM black, left vertical axis and peak intensity red, right vertical axis normalized to their initial values as a function of propagation distance. The inset displays the axial wakefield experienced by an electron moving near the speed of light. The wakefield amplitude increases due to the intensity increasing and the pulse duration shortening.

In spite of the simulation pulse duration being longer than the matched duration, the energy gain for $a_0 = 0.25$ is nearly that predicted by Eq. (3.4). The nonlinear evolution of the laser pulse boosts the acceleration by compressing the initial unmatched pulse duration to a duration closer to the matched value $\sigma_{FWHM} \sim \lambda_p / 2$, while, at the same time, increasing the wakefield amplitude through the increase in intensity. The pulse's ponderomotive force forms a local nonlinear gradient with the electron density decreasing from the front of the pulse backwards, causing the front and middle of the pulse to undergo spectral redshifting and slide backwards, forming an optical shock [25]. Figure 3.4 shows the evolution of the pulse's on-axis temporal FWHM and on-axis intensity. Both quantities are normalized to their initial values. The product of FWHM and peak intensity is essentially constant, suggesting that the pulse is not undergoing significant nonlinear focusing or spot oscillations due to unmatched guiding [79]. The inset in Fig. 3.4 displays the growth in axial wakefield experienced by a relativistic electron in the corrugated channel due to pulse compression.

Chapter 4: Shock formation in supersonic cluster jets and its effect on axially modulated laser-produced plasma waveguides

4.1 Introduction

Axially-modulated plasma waveguide are the most essential part for quasi-phasematched direct laser acceleration and laser wakefield acceleration of electrons, as described in Chapter 2 & 3. Our group previously showed that a gas cluster jet is an efficient medium in which to produce laser-generated plasma waveguides [54,80]. We also demonstrated a technique for producing axial modulations in cluster-based plasma waveguides by periodically obstructing the cluster flow using an array of thin wires [52]. This is a simple alternative to demonstrated optical techniques which axially modulate laser intensity at the target [51,81]. However, in the previous study [52], the axial modulation period was limited to > 200 μm due to the onset of an incompletely understood plasma density drop in the region between the wires.

In this chapter, we present a detailed investigation of the origin and mitigation of this density drop by examining jet flow through two wires with variable separation. The density drop is found to be caused by shock waves from supersonic monomer (individual atoms/molecules) dominated gas flow into the wires, which we observe with transverse interferometry and shadowgraphy. As mean cluster size is increased, with an accompanying decrease in monomer concentration, the jet flow becomes more ballistic and the monomer-induced shock amplitude is decreased. By optimizing the cluster jet density and temperature, we have been able to achieve plasma guiding

structures with modulation periods as small as 70 μm and plasma structures as narrow as 45 μm.

4.2 Experimental setup

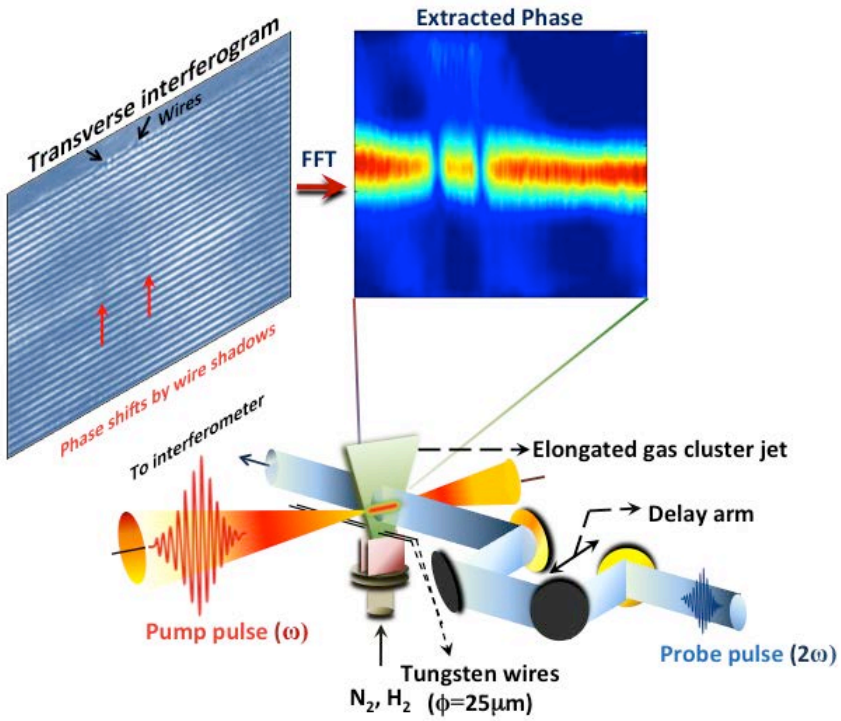

Figure 4.1. Experimental setup: Here are shown two 25 μm diameter wires, one mobile and one stationary, placed across the elongated nozzle of a cryogenically cooled supersonic gas jet. A 200mJ, 35fs Ti:Sapphire laser pulse was focused by an f/25 spherical mirror to ionize the cluster target. A portion of the 800nm laser pulse is split from the main beam, frequency doubled, and used as a transverse interferometry/shadowgraphy probe. Shown are an example raw transverse interferogram, followed by results of a Fourier transform analysis yielding the phase shift imposed by the plasma on the probe.

Figure 4.1 shows the experimental setup. The target is a 15mm by 1mm elongated cluster jet pulsed at 10Hz. To improve cluster formation, the high pressure gas valve was cryogenically cooled to temperatures as low as 93K. Temperature control allows approximate control of the mean cluster size, with larger clusters formed at colder jet temperatures for fixed valve backing pressure. In our experiments, the gas valve was operated to keep the average gas density in the laser interaction zone of the jet constant while varying the mean cluster size. This was accomplished by maintaining the valve backing pressure at 300 psi for temperatures in the range 293 K to 173 K, and 350 psi for 133 K to 93 K. Under these conditions, an increase (decrease) in the cluster size causes a decrease (increase) in the concentration of unclustered atoms/molecules (monomers). The average density in the cluster jet at the peak of the nozzle flow was found by longitudinal interferometry. We found that at 10 Hz jet operation for the range of valve conditions used, the background pressure in our vacuum chamber was proportional to the interferometer-derived density, so we used the background pressure as the proxy for average atom/molecule density in the cluster jet. Monitoring the background pressure allowed straightforward variation of the mean cluster size while keeping the total atom/molecule density at the target approximately constant. The plasma was generated by a 200mJ, 35 fs Ti:Sapphire laser pulse focused at f/25 end-on into the cluster jet. A small portion of the main pulse was split and frequency doubled for use as a transverse interferometric probe pulse. The pump probe time delay was adjustable in the range –1 ns to 3 ns.

A sample interferogram and an extracted phase image are shown in Figure 4.1. The axially-averaged target neutral gas density profile was measured using an interferometric probe directed through the elongated dimension of the gas jet; the result is in good agreement with plasma density measured at short probe delays with respect to the pump, before appreciable plasma hydrodynamic evolution occurs.

The experiments investigated the effects of one wire, two wires, and an array of wires on the gas flow. Figure 4.1 shows the case of two parallel 25 μm diameter Tungsten wires strung across in contact with the nozzle exit. One wire remained stationary and the other wire was attached to an actuator, allowing adjustment of the distance between the wires. The wire separation was measured from phase images of their shadows, as seen in the transverse interferogram in Fig. 4.1.

4.3 Analysis of cluster flow

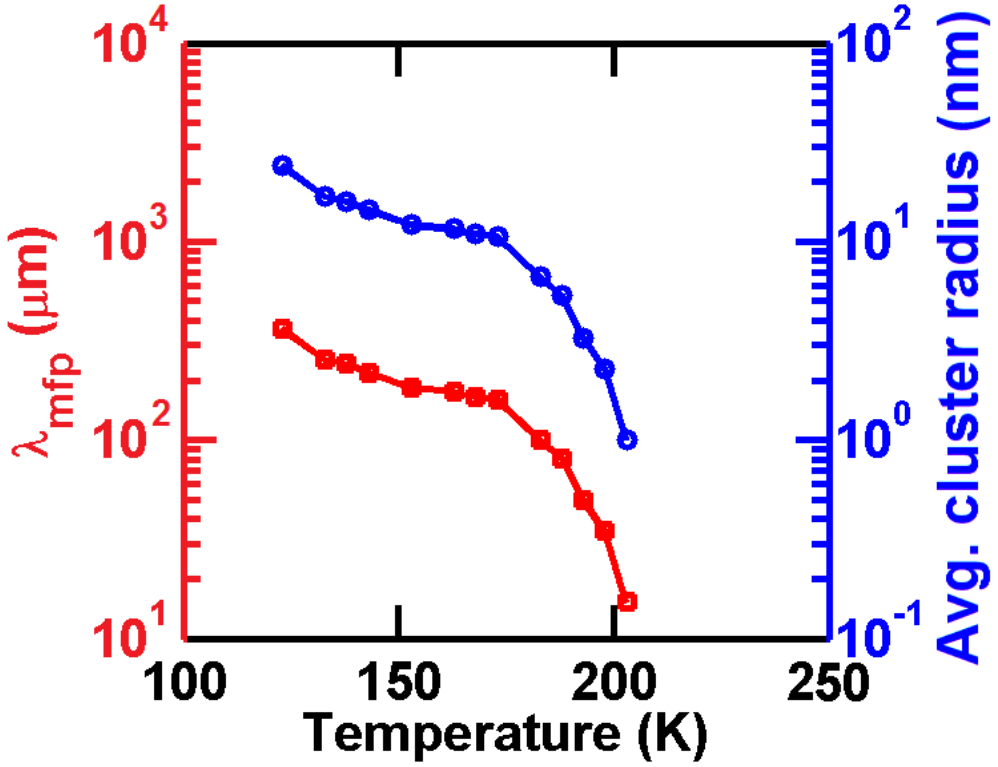

Figure 4.2. Average nitrogen cluster size (radius) and collisional mean free path as a function of valve temperature at a backing pressure of 400 psi.

The atoms or molecules in a gas flow can bond to form nanometer sized particles called clusters when the mutually induced dipole-dipole attractive potential between particles (van der Waals potential) exceeds in magnitude the particle thermal energy. This can occur in supersonic gas jets when high pressure gas expands rapidly into vacuum and cools.

A well-known semi-empirical relation introduced by Hagena is often used to estimate cluster size for flows from cylindrical nozzles as a function of temperature, valve backing pressure, and nozzle geometry [53]. However, this formula does not apply to our case of an elongated gas jet. To measure average cluster size and number

of clusters per unit volume, we developed an all-optical method combining Rayleigh scattering and interferometry [82] and applied it to the elongated jet. The method assumes complete clustering and so is less accurate in the region of higher monomer concentration. However, because the Raleigh scattering part of the measurement strongly favors clusters over monomers, the extracted average cluster size is reasonably accurate, even for significant monomer concentrations up to ~50% [82]. The average cluster radius, for a nitrogen jet backed at 400 psi for a range of valve temperatures, is shown as the blue curve of Fig. 4.2.

The extracted average cluster radius was used to determine a collisional mean free path $\lambda_{mfp} = (N_c \sigma)^{-1}$ for cluster-cluster collisions, where N_c is the density of clusters and σ is the collision cross section. As the inter-cluster potential is very small compared to the cluster kinetic energy, we use $\sigma = \pi a^2$, assuming a hard sphere collision model where a is the average cluster radius. The result is plotted as the red curve of Fig. 2, which shows a quick drop in λ_{mfp} from ~200 μm to < 20 μm as the valve temperature increases from 175K to 200K. Later in the paper, we show that this variation in λ_{mfp} explains the ballistic flow of clusters in the lower temperature gas flow regime and the onset of strong shock waves for higher temperature gas jet flow.

4.4 One- and two- wire experiment

Initially, we used nitrogen gas with varying valve temperature to observe the effect of cluster size and monomer concentration on the gas flow around the wires. By varying the temperature from 293 K to 93 K, we observed the transition from a

normal supersonic gas flow of monomers to the ballistic cluster flow regime. Over this transition, the mean free path of the dominant flow particles goes from much smaller than the spatial scale of any local boundary to much larger. In our case, the local spatial scale is the 25 μm wire diameter. At higher temperatures, the dominant flow particles are monomers, with an interparticle collisional mean free path much smaller than the wire diameter. At lower temperatures, clusters become the dominant flow particle, with infrequent interparticle collisions. The cluster flow is ballistic, and the mean free path is much larger than the wire diameter.

The signature of non-ballistic supersonic gas flow past the wires is generation of shock waves. When an element of collisional fluid collides with the wire, it undergoes local compression. For sub-sonic flows, this pressure disturbance would launch sound waves with a significant component of velocity opposite to the flow direction and with larger magnitude, with some of the waves propagating back to the nozzle orifice. However, for supersonic flow, as is the case here, the pressure disturbance is entrained in the forward fluid flow. The net disturbance propagates as the vector sum of the local sound speed and the supersonic gas flow velocity, giving rise to the refractive index modulations imaged by our interferometric probe beam. Alternatively, and more simply, the wire can be viewed as moving supersonically through a stationary gas, launching angled shock fronts forming a section of a Mach cone. The half-angle of the shock fronts with respect to the flow axis is then given by $\alpha = \sin^{-1}(1/M)$, where $M = v_f/c_s$ is the flow Mach number, c_s is the sound speed, and v_f is the flow speed. Based on the shock angles at different valve temperatures, the Mach number of the flow varies monotonically from $M = 1.2$ at 93K to 1.6 at 293K.

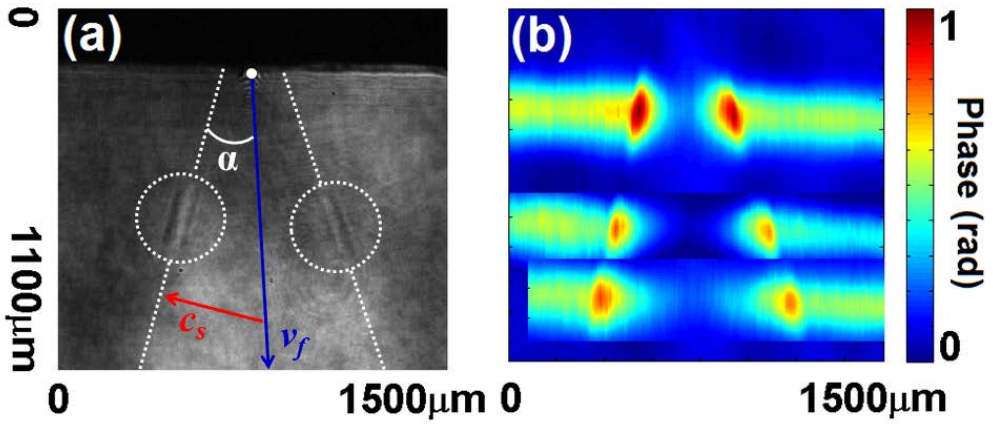

Figure 4.3. (a) Shadowgraph of shocks in nitrogen jet flow above a single 25μm tungsten wire, with probe delay 1ps. The wire (indicated by a white dot) is centered on the shocks. The flow is directed down. The valve temperature and pressure were 293K and 300 psi. The blue and red arrows depict the fluid flow and sound velocities, and the dashed white line highlights the shock location. (b) Sequence of extracted phase images of plasma resulting from femtosecond laser interaction with the gas flow 0.5, 0.9 and 1.1mm above the 25μm wire. The laser enters from the left. The probe delay is 1 ps.

Interaction of the pump pulse with the gas jet with a single wire strung across the nozzle orifice is shown in the shadowgraph in Fig. 4.3.(a) , for the case of the valve operated at room temperature (293 K) and 300 psi. Here, as expected for the case of dominant monomer flow, we observe angled shock fronts which manifest as enhanced plasma density at the shock front locations. To aid visualization, the figure shows arrows depicting the gas velocity (blue) and sound velocity (red), a white dot indicating the wire position, and the angle $\alpha=\sin^{-1}(1/M)$. Figure 4.3.(b) is a series of extracted phase images of plasmas generated at 0.5mm, 0.9mm, and 1.1mm above the single wire, where the laser pulse, entering from the left, intersects and preferentially heats the enhanced density in the increasingly separated local shock fronts, which have a widening region of greatly reduced plasma density between them. The reduced plasma density is evidence that the shocks, which appear to the supersonic flow as a stationary disruptive structure, act to destroy the clusters flowing into them. The

entire region of the flow between the shocks is therefore cleared of clusters and the efficiency of the subsequent laser plasma interaction is reduced there.

The destruction of the clusters can be understood by considering the supersonic flow of the partially clustered gas into an oblique shock. Since the shock width is smaller than the other flow scales in the jet, we can approximate the interaction as a flow through a step change in pressure and density subject to conservation of mass, momentum and energy [83]. Under these conditions, the average fluid density (ρ) and pressure (P) upstream and downstream of the shock are related by $\frac{\rho_1}{\rho_2}=\frac{\gamma-1}{\gamma+1}+\frac{2}{(\gamma+1)M^2\sin^2\beta}$ and $\frac{P_2}{P_1}=\frac{2\gamma M^2\sin^2\beta}{\gamma+1}-\frac{\gamma-1}{\gamma+1}$, where "1" refers to upstream and "2" refers to downstream, M is Mach number, β is the oblique flow angle with respect to the shock front, and γ=7/3 is the specific heat ratio for our flow gas, nitrogen, here treated as an ideal gas. The gas temperature change as a result of flow through the shock front is then given by

$$\frac{T_2}{T_1}=\frac{P_2\rho_1}{P_1\rho_2}=1+\frac{\Delta T}{T}=\left[1+\frac{2\gamma}{\gamma+1}(M^2\sin^2\beta-1)\right]\left[\frac{2+(\gamma-1)M^2\sin^2\beta}{(\gamma+1)M^2\sin^2\beta}\right]. \qquad (4.1)$$

But $\sin\alpha = 1/M$, where α is the angle of the shock from the flow direction at the wire location, and $\beta=\alpha+\delta\alpha$, where $|\delta\alpha/\alpha|<1$. This gives for the gas temperature change through the shock $\frac{\Delta T}{T}=4\delta\alpha\left(\frac{\gamma-1}{\gamma+1}\right)\sqrt{M^2-1}$.

Using γ=7/3, M in the range 1.1–1.6, and $\delta\alpha/\alpha$~0.3 (from the jet flow geometry) gives $\Delta T/T$ in the range ~0.10 to 0.30. In the temperature range where there is a significant enough monomer density to form shocks while clusters are still present, there is strong temperature sensitivity of the cluster concentration. Because

the van der Waals bond energy is typically ~0.02 eV [84] clusters entrained in gas flows at T~200K (~0.02 eV), are vulnerable to decomposition, especially when passing through a shock front where ΔT~70K.

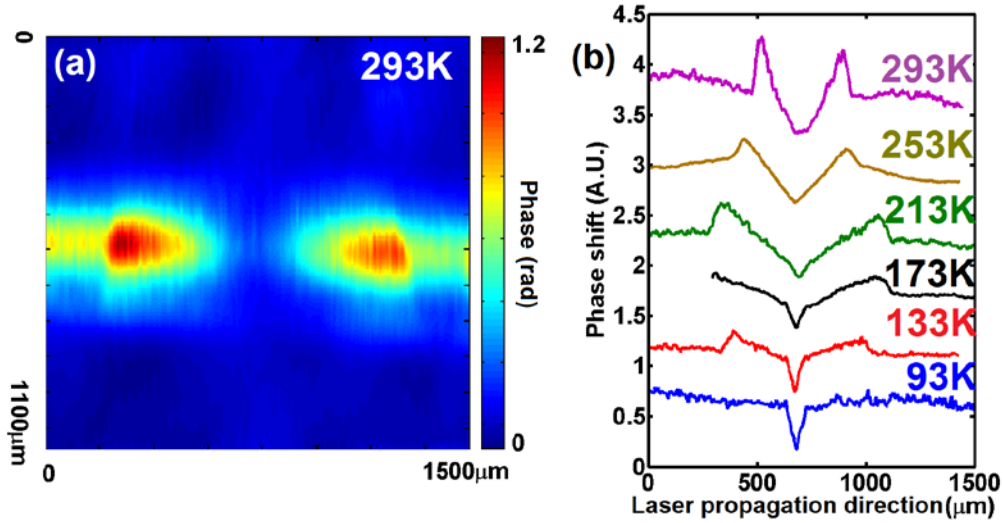

Figure 4.4. (a). Phase image of laser-heated plasma produced in nitrogen gas flow at height 1.1 mm above a single 25 μm wire, for probe delay 1 ps. The bumps are increased electron density from laser heating of shock-enhanced gas density zones. (b) Phase lineouts of single wire plasmas (such as in (a)) for a sequence of valve temperatures.

Figure 4.4.(a) shows a phase image of nitrogen jet plasma generated over a single 25μm wire for the valve at 293K, where the flow is dominated by monomers. The location of the shock fronts is clearly seen. A central lineout of this image is shown in the top curve of Fig. 4.4.(b), and lineouts of single wire images at decreasing valve temperature are shown as the lower curves. The shockwaves are seen as upward pointing bumps in the phase lineouts. As the temperature is decreased, the shockwave bumps disappear, leaving only the shadow of the wire imposed in the flow, seen as an increasingly fine downward pointing bump. At the higher temperatures, the shock wave from a single wire appears to disrupt the entire

flow within its wake, over a transverse extent much larger than the wire diameter. It is only in the strongly clustered (and ballistic) flow regime at low valve temperatures that a true wire shadow emerges.

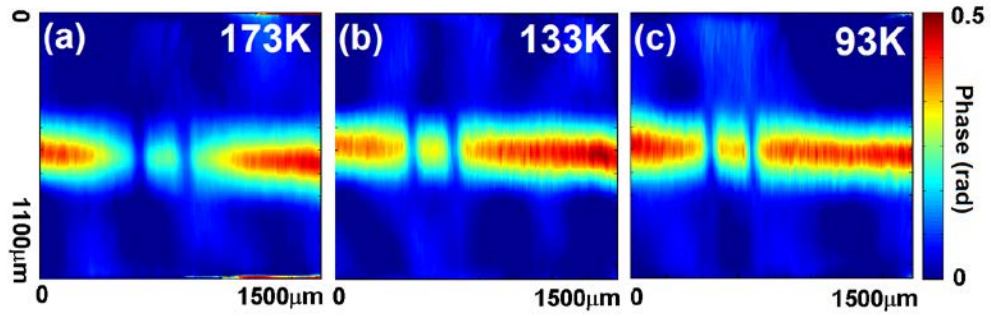

Figure 4.5. Phase images, with probe delay 1 ps, of laser heated flow at height 1.1 mm above two wires separated by 150μm at temperature (a) 173K, (b) 133K, and (c) 93K. Increased clustering occurs at reduced temperature.

The wide shock disruption of the flow past a single wire is the origin, for narrowly spaced wires, of the reduced plasma density from laser heated clusters seen in our earlier experiment [52]. We note from Fig. 4.4.(b) that the shock disruption extends 250 μm on either side of the wire at 133K. This was the valve temperature in the previous study [52], where we found a plasma density drop for wire separations was less than ~200 μm. As discussed earlier, the plasma density drop is caused by shock-induced cluster decomposition, which results in greatly reduced ionization by the laser pulse. Figure 4.5 shows a sequence of phase plots, for decreasing valve temperature, of plasma generated over two wires separated by 150 μm. Consistent with the results of Fig. 4.4, it is seen that the sharpest two-wire shadow with the highest in-between density occurs for the lowest valve temperature, 93K, where the shock-generating monomer concentration is the smallest. Only here is the flow

sufficiently ballistic that cluster flow between the wires is the same as on either side of the wires.

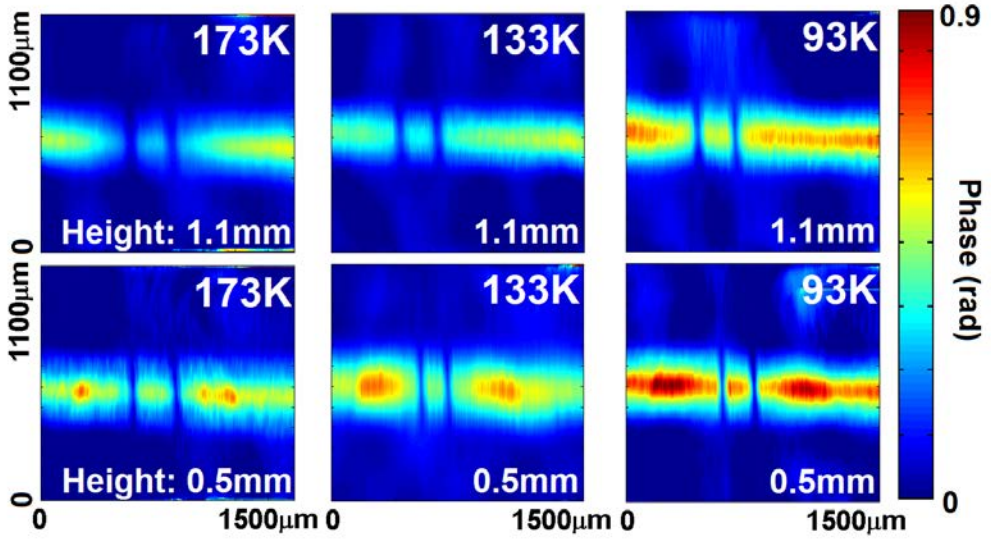

Figure 4.6. Phase images of nitrogen plasma generated at heights 0.5 mm and 1 mm above two wire separated by 200 μm, for valve temperatures 133 K, 173 K, and 93 K. The probe delay is 1 ps.

The results of another test for the transition to ballistic cluster flow are shown in the phase images of Fig. 4.6. Here, plasma was generated at 2 different heights, 0.5 mm and 1.5 mm, above two wires spaced at 200 μm. For highly ballistic flow, one would expect the wire shadows to remain sharp at the higher location with the plasma density maintained between the shadows. This is what is seen for the valve temperature at 93K. As the valve temperature is increased to 133K and then to 173K, the shadows at the higher location become wider and the plasma density between the shadows drops. From the earlier single wire results, we can attribute the density drop between the shadows to cluster dissociation by shocks launched by each wire into the flow region between the wires. This region widens with height above the wires.

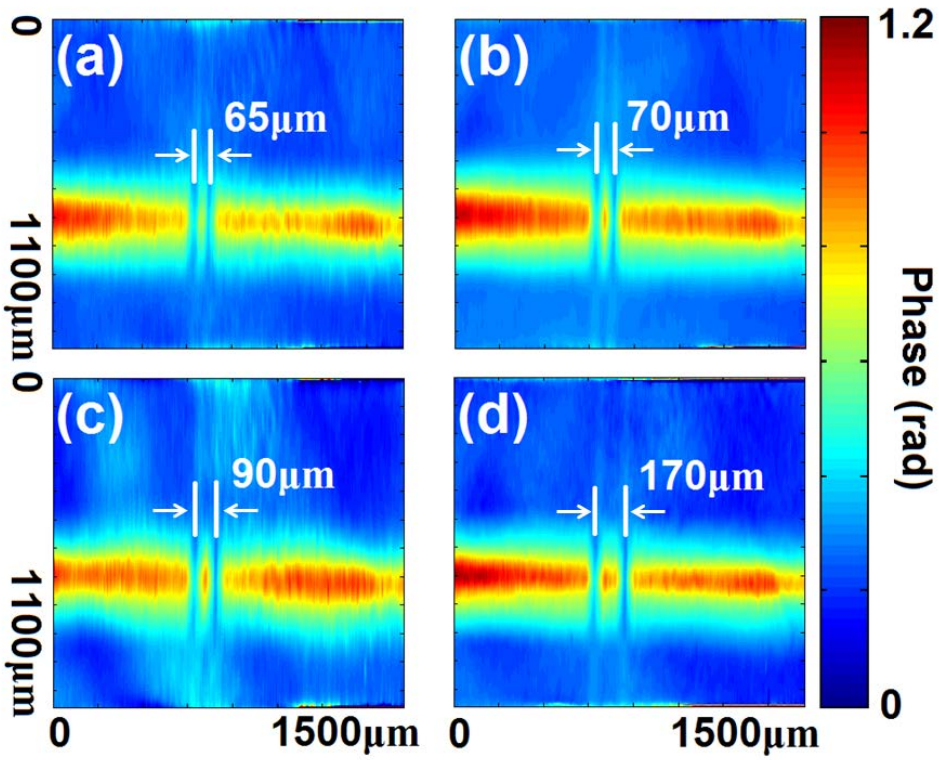

Figure 4.7. Phase images of laser produced plasma in a nitrogen cluster jet flowing past two 25µm tungsten wires separated by (a) 65µm, (b) 70µm, (c) 90µm, and (d) 170µm. In each image the gas jet was at 93K and 250PSI backing pressure. The laser propagation is from the left at height 1.1 mm above the wires. The probe delay is 1 ps.

Figure 4.7 shows extracted phase images of nitrogen plasma with different wire separations for the gas valve at 93K, where we expect ballistic cluster jet flow. This experiment was carried out to determine the minimum wire spacing achievable before the density between the wire shadows begins to drop. This spacing corresponds to the minimum period achievable for a wire-modulated plasma waveguide under our conditions. We found that the density between the wires drops for wire separations less than 70 µm. Below this separation, the wire shadows begin to merge. At 70 µm spacing, the plasma structure width between the wires is ~ 45 µm.

We now look at how the plasma produced from a wire modulated cluster flow evolves in time. The laser-driven ionization process in a cluster is dominantly collisional, due to its solid density [85,86]. The heated clusters are strongly ionized and heated and merge into a locally uniform plasma that expands supersonically into the surrounding cluster/gas medium, forming a plasma waveguide structure with a minimum electron density on axis and an elevated outer wall from the outward propagating shockwave [80,87]. The waveguide generation and evolution is captured with transverse interferometry with varying delay of the probe pulse. The plasma-induced probe phase shift is extracted from the interferogram using fast Fourier transform techniques and the electron density profile is determined by Abel inversion [87], assuming cylindrical symmetry of the plasma channel.

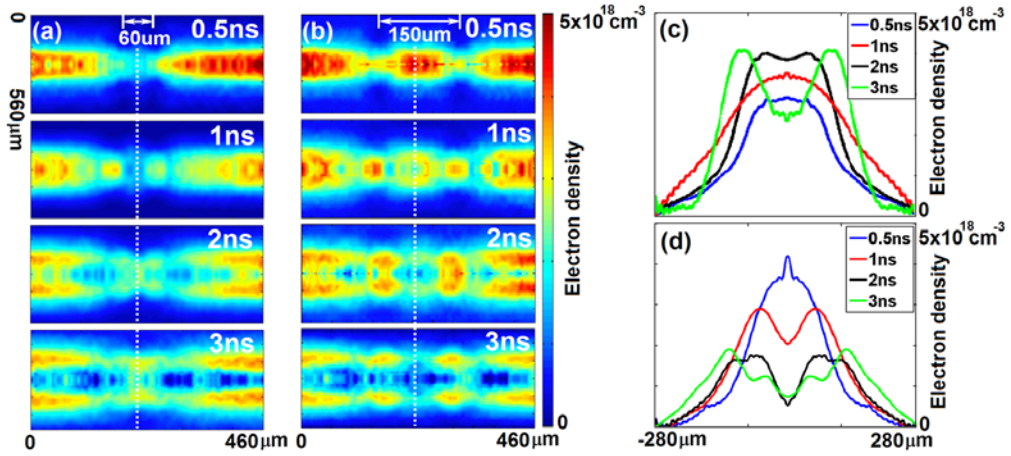

Figure 4.8. Electron density profiles of nitrogen plasma channels produced 1.1 mm above the wires, at probe delays: 0.5ns, 1ns, 2ns, and 3ns, with two wire separations: (a) 60 μm and (b)150 μm. (c) Density profile lineouts of (a) along dotted white line. (d) Density profile lineouts of (b) along dotted white line.

Figure 4.8 shows the time-evolving electron density profiles for 2-wire experiments with wire spacing 60 μm (part (a)) and 150 μm (part (b)). The delays

shown (≥ 0.5 ns) are with respect to plasma generation by the 40 fs pump pulse at *t*=0. Figure 7 shows the situation for *t*=0 ns delay, where there is relatively little cluster density in the region between the narrowly spaced (65μm) wire shadows compared to that for the wider (170 μm) spacing. In Fig. 4.8.(a), by 0.5 ns delay the density of the strongly heated plasma between the shadows drops as it expands into the shadow locations. By 1 ns, the in-between density continues to drop and the density at the shadow locations continues to increase, also supplied by high pressure plasma from outside the shadows. By 2 ns, the plasma begins to fill in the gap between the shadows and by 3 ns, the peak density is located at the shadow gap with an axial scale length of ~60 μm, comparable to the original shadow separation. In Fig. 4.8.(b), as in part (a), the density at first drops in the region between the shadows and increases at the shadow locations. But this trend continues so that by 3 ns, the density is minimum at the in-between region and maximum at the shadow locations. Comparing the evolution shown in Fig. 4.8.(a) and (b), we note that the reduced heating of a narrower in-between plasma in (a) means that this region is more susceptible to filling in from adjacent higher pressure plasma regions, so by 3 ns the in-between region hosts a high plasma density. In Fig. 4.8.(b) the denser and more strongly heated in-between region strongly expands outward into the adjacent regions and its density drops. This reduced density is maintained at 3 ns delay.

In Fig. 4.8, we are also interested in the evolution of the waveguiding structure. For the panels in (a) and (b) for delays >1 ns, a clear on-axis electron density minimum develops, along with a well-defined higher density wall driven by the radially expanding shock wave. Transverse radial lineouts at the location of the

vertical dashed lines are shown in Fig. 4.8.(c) (for 4.8.(a)) and Fig. 4.8.(d) (for 4.8.(b)). In both cases, at appropriate delays, the electron density difference between the central minimum of the electron density profile and the shock wall is ~10^{18} cm^{-3} which is sufficient to guide high intensity pulses [69]. This density difference is even greater at other axial locations in the waveguides.

4.5 Experiments with wire array

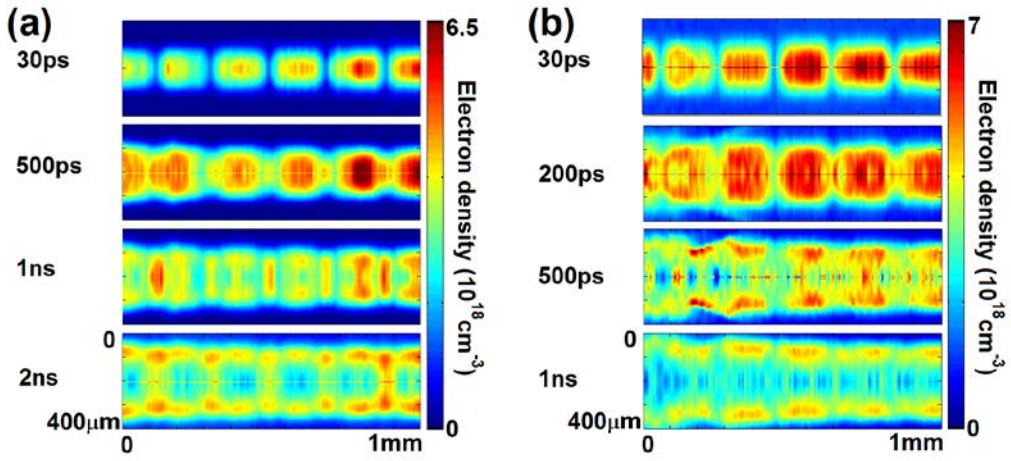

Figure 4.9. Time evolution of electron density profiles of plasma waveguides with 200μm axial modulations in (a) a nitrogen cluster jet at 93K and 250 PSI backing pressure and (b) A 90% hydrogen / 10% argon cluster jet backed at 93K and 300 PSI. The waveguides are generated 1.1 mm above the wires.

Finally, we fabricated 5-wire arrays of 25μm tungsten wire separated by ~200 μm to produce several periods of axial modulation. Figure 4.9.(a) shows time evolution of a plasma waveguide produced in a nitrogen cluster jet at 93K and 250 psi backing pressure, while Fig. 4.9.(b) is for a 90% hydrogen/10% Ar gas mix cluster jet at 93K and 300psi. In both cases, we expect ballistic cluster flow. It is seen that the hydrogen plasma-based waveguide expands significantly faster than the nitrogen

plasma-based guide, owing to the lighter hydrogen ions. It is seen that the sharp wire shadows evident at early pump-probe delays are eventually filled in by the evolving plasma, which expands axially as well as radially.

4.6 Conclusions

Arrays of wires obstructing gas flow offer a simple and robust method for creating index modulations in plasma waveguides. However, shock waves formed off of the wires act to destroy the clusters that flow into them, reducing the efficiency of subsequent laser heating and a strong reduction in plasma density between the wire shadows. We have shown that increasing the cluster size in the gas jet, which occurs along with a reduction in monomer concentration, transitions the supersonic gas to a ballistic flow regime in which shock effects are negligible and guiding structures with sub-100 μm modulation periods may be achieved.

Chapter 5: Laser wakefield acceleration of electrons with ionization injection in a pure N^{5+} plasma channel

5.1 Introduction

Recently, ionization injection of high Z dopants was proposed and demonstrated to increase electron beam charge and lower the intensity threshold for electron trapping in LWFA [33-37]. In this scheme, inner shell electrons of the high Z dopant are ionized near the peak of the drive laser pulse and are trapped in the potential well created by the plasma wave. In previous experiments, the high-Z dopant typically does not exceed ~10% of the total mass density due to laser pulse refraction by the additional plasma density created on axis [36].

In this work, we present an effective LWFA assisted by ionization injection in a pre-formed channel produced in a nitrogen cluster jet. The nitrogen cluster jet has been shown to be an excellent medium for producing plasma channels capable of guiding an intense laser pulse up to several centimeter scale lengths [54]. We show that the interaction of the channel forming pulse with the nitrogen clusters creates a plasma channel formed mainly of N^{5+} ions due to the large ionization potential gap between the L-shell (98 eV) and K-shell (552 eV) electrons in nitrogen. We present evidence that the plasma channel is formed nearly exclusively of helium-like nitrogen ions, which act as a nearly ideal source of electrons for the ionization injection scheme. Additionally, we show that a preformed plasma channel with a guiding structure is able to stabilize the high energy electron production compared to a pre-

formed plasma with a flat density profile. Finally, 3D particle-in-cell (PIC) simulations are also performed to investigate the trapping and acceleration processes in the N^{5+} plasma channel.

5.2 Experimental setup

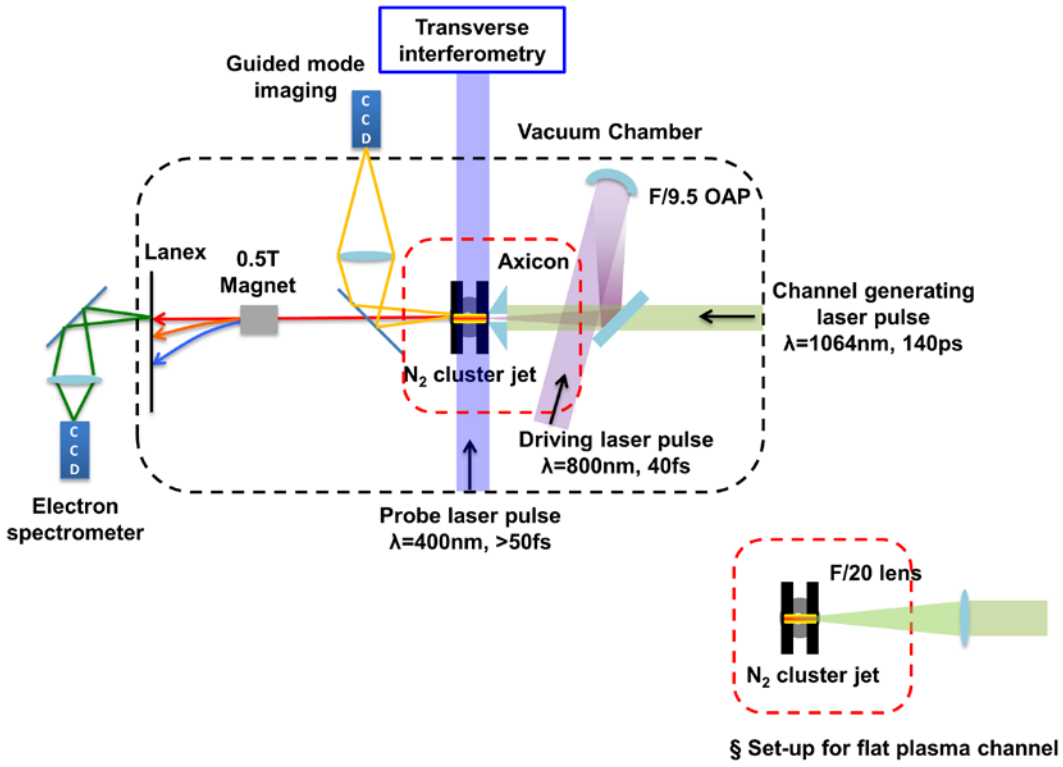

Figure 5.1. A schematic of the experimental setup.

Figure 5.1 shows a schematic of the experimental set-up. The target was a cryogenically cooled cluster jet with a 1.5 mm by 1 cm orifice pulsed at 10Hz. As a high pressure gas expands into vacuum, Van der Waals forces can form aggregates at solid density with typical radii between 1-100nm, controlled by the gas backing pressure, species, valve temperature, and nozzle geometry [53]. In these experiments the supersonic cluster jet was cooled to 100 K and backed with pressures between 200-400psi. Our previous study showed that the monomer contribution in the nitrogen cluster jet drops significantly at these conditions [88]. We control the plasma density by tuning the backing pressure and jet opening time.

The plasma channels were generated by focusing a mode-locked Nd:YAG laser (1064nm, 140ps, up to 500mJ) by an axicon with a base angle , creating a 1.5cm long line focus over the cluster jet. To create a plasma channel with a flat transverse density profile, a 100mJ Nd:YAG laser pulse was focused by a f/20 spherical lens. For these experiments, the target length was set to 1.5mm, about the dephasing length of the $1.1\times10^{19} cm^{-3}$ plasma, by orienting the nozzle perpendicular to the laser propagation direction. Once the plasma waveguide was formed, a Ti:Sapph laser pulse (805nm, 40 fs, up to 400mJ) was injected by a f/9.5 off axis parabolic mirror through a hole in the axicon. The Ti:Sapph and Nd:YAG lasers were synchronized with better than 10ps precision. The injected laser pulse came to a 15 micron FWHM focus, with a peak normalized vector potential a0 = 1.2.

A small portion of the Ti:Sapphire laser pulse was split from the main beam, frequency doubled, and directed transversely across the waveguide to a folded wavefront interferometer and onto a CCD. Phase extraction followed by Abel

inversion allowed reconstruction of the channel density profile assuming cylindrical symmetry of the channel [87]. Adjustment of the timing of the probe pulse with respect to the channel forming and injected pulses allowed density measurements to be made in the neutral gas as well as the plasma channel before and after passage of the guided pulse. Guiding efficiency was monitored by imaging the exit mode of the channel to a CCD as well as an optical spectrometer. Electron beam profiles and energy spectra were measured using an electron spectrometer consisting of a removable 2 inch long 0.5T magnet and a Lanex [89] screen. The screen was placed 15 inches from the cluster jet and 10 inches from the end of the magnet. A thick Aluminum foil was placed before the Lanex screen to shield it from the laser beam, and a green filter was placed in front of the CCD to improve the signal to noise ratio.

5.3 Production of pure N^{5+} channels

Cluster sources have been shown to be very efficient targets for plasma channel formation [54, 80]. Collisional ionization within the solid density clusters at the leading edge of the channel forming pulse creates a much more highly ionized plasma compared to traditional gas jets of similar average density. This highly ionized plasma is then efficiently heated through inverse bremsstrahlung over the full duration of the long (140ps) channel forming pulse [54].

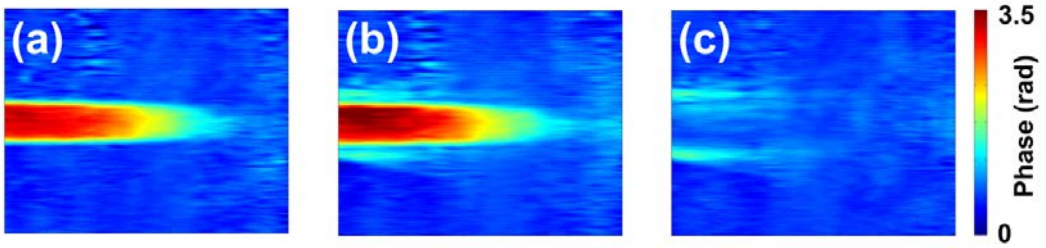

Figure 5.2. (a) Phase map of the rear side of an axicon created plasma waveguide before guiding a 15mJ (0.4TW) TiSa laser pulse. (b) is a phase map of the same area as (a) after guiding a 15mJ TiSa laser pulse. (c) is the difference in phase of (b) from (a).

We experimentally investigate the ionization state of the plasma channel by guiding a 15mJ 40fs (0.4TW) Ti:Sapphire laser pulse in the plasma waveguide. The energy throughput of the plasma waveguide is 80% of the injected pulse energy. The peak intensity of the guided laser pulse at the end of the waveguide is $\sim 1\times10^{17} W/cm^2$, based on the guided mode profile and the injected pulse length. Considering that the over-the-barrier ionization (OTBI) threshold of N^{4+} (98eV) ions is $\sim 1\times10^{16} W/cm^2$, any Li-like nitrogen ions in the channel should be ionized by the guided laser pulse, which would be seen as an increase in the measured channel

density after transmission of the guided pulse. Figure 5.2(a)-(c) show phase profiles near the end of the plasma waveguide. Figure 5.2(a) and (b) are taken before and after guiding the 0.4TW laser pulse, and Fig. 5.2(c) is the phase difference of (b) from (a) showing any extra ionization by the 0.4TW laser pulse. Even though the laser intensity inside the channel should be an order higher than the OTBI threshold of N^{4+} ions, most of the extra ionization occurs outside the plasma waveguide where uncoupled laser energy interacts with unionized clusters. Negligible ionization inside the channel reinforces the hypothesis that the majority ion species of our plasma channel is N^{5+}. Additionally, and as an added check on the ionization state, the measured nitrogen molecule densities were approximately 10 times less than average measured plasma densities, indicating 5× ionization of each nitrogen atom.

5.4 Effect of channel profile on electron beam quality

Once a column of clusters is ionized and heated by the channel forming laser pulse, the plasma expands hydrodynamically, and a radial shockwave is formed at the boundary between the plasma and unionized clusters. After a proper delay, the plasma develops an approximately parabolic density profile with a minimum on axis capable of matched guiding of a high intensity laser. A detailed description of plasma waveguide generation in cluster jets can be found in our previous work [54].

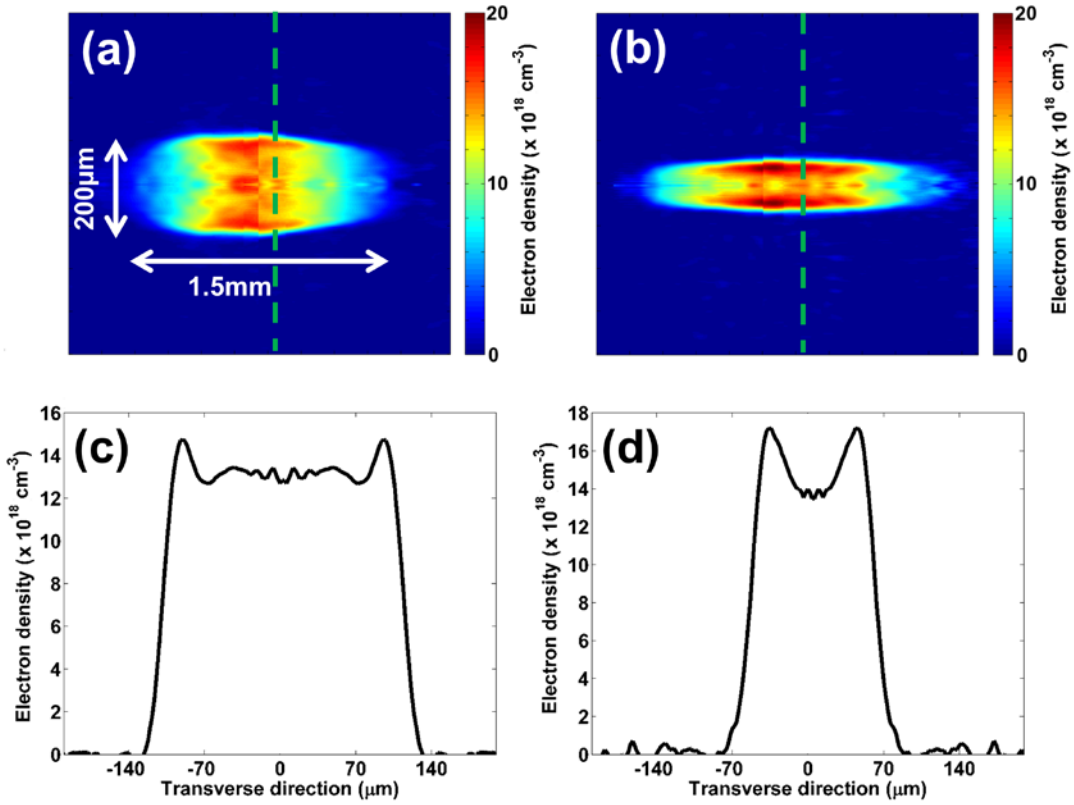

Figure 5.3. (a) Electron density of a plasma channel created by a f/20 lens and 100 mJ pulse after 500ps delay. (c) a line-out of (a) marked as green dashed line. (b) Electron density of a plasma channel created by a 400 mJ pulse focused by an axicon with base angle 28° after 420ps delay. (d) a line-out of the green dashed line in (c).

Figure 5.3 shows the electron density profiles of plasmas created by two different methods; (a) with a 400 mJ pulse focused by an axicon, and (b) with a 100 mJ pulse focused by an f/20 lens. The lens-generated plasma has a plateau in the center whereas the axicon created plasma has a clear density minimum on axis. The axicon created plasma profile shown in Fig. 5.3(d) is suitable to guide a laser pulse with FWHM spot size of $16\mu m$, which is close to our measured spot size. By tuning the backing pressure and jet opening time, the peak on-axis densities for both cases are set to $1.4\times10^{19} cm^{-3}$. The channels have long density ramps along the laser propagation axis which follows the neutral N_2 molecule density profile. The PIC

simulations presented later show that the density down ramp near the back side of the channel helps to trap the ionized inner-shell electrons by expanding the plasma bucket, as has been reported by other groups [30-32]

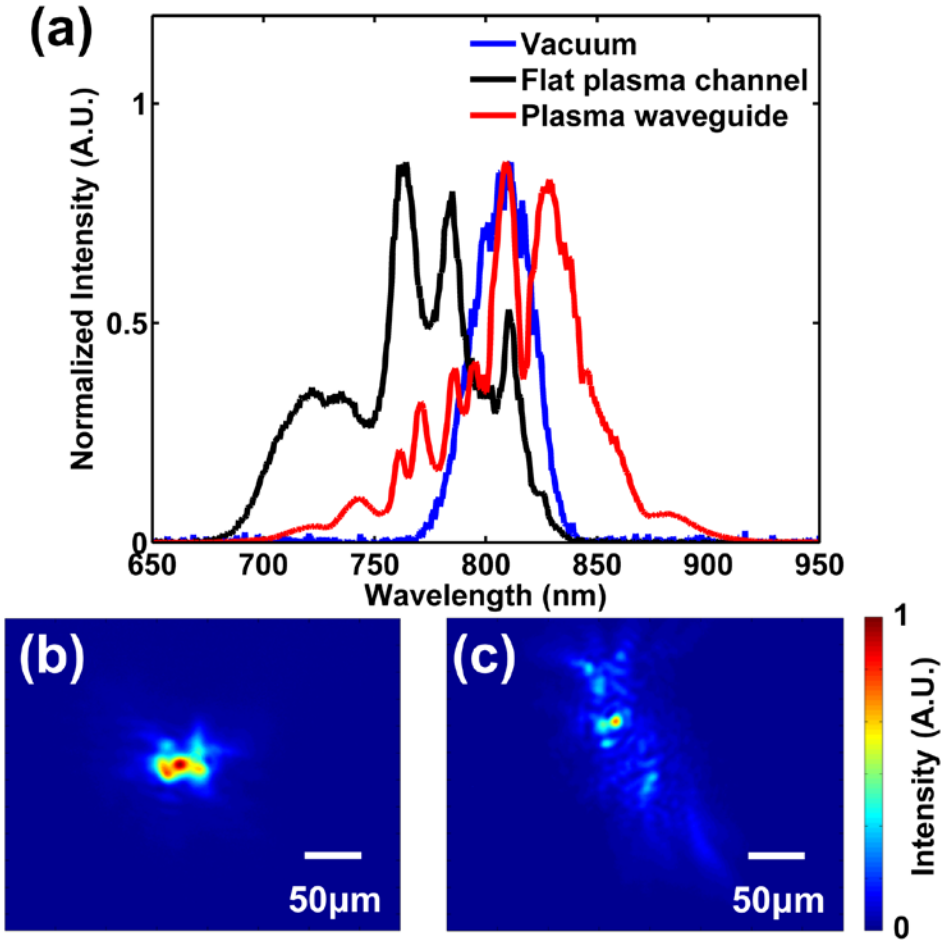

Figure 5.4. (a) Optical spectra of the 10TW laser pulse (vacuum spectrum: blue curve) after interaction in the N^{5+} flat profile channel (black curve) and in the N^{5+} waveguide (red curve). Exit modes of 10TW laser pulses imaged at the end of (b) the plasma channel and (c) the flat density profile in the same color scale.

A 10TW drive laser pulse with a peak intensity of $3.3\times10^{18} W/cm^2$ $(a_0 = 1.2)$ at the focus was injected into both pre-formed plasma density profiles. Figure 5.4(a) shows optical spectra of the drive pulse after exiting the flat and guiding plasma profiles. The drive pulse injected into the guiding profile shows large, symmetric

spectral broadening consistent with driving a large amplitude plasma wave in the self-modulated regime [90]. In contrast, the drive pulse injected into the flat plasma profile is largely blue shifted due to ionization of N^{5+} and N^{6+} ions inside the channel in addition to the ionization of the nitrogen clusters by the diffracting laser energy. Exit mode images of the laser injected into the guiding profile (Fig. 5.4(b)) show much stronger confinement along the propagation axis than mode images of the laser injected into the flat plasma profile (Fig. 5.4(c)). This shows that even though our laser pulse power is larger than the critical power for RSF near the center of the channel $\left(P / P_{cr} \approx 3\right)$ the plasma channel is more effective in confining the laser pulse energy to the propagation axis. This enables the channel-guided pulse to more effectively drive a large amplitude plasma wave suitable for electron acceleration.

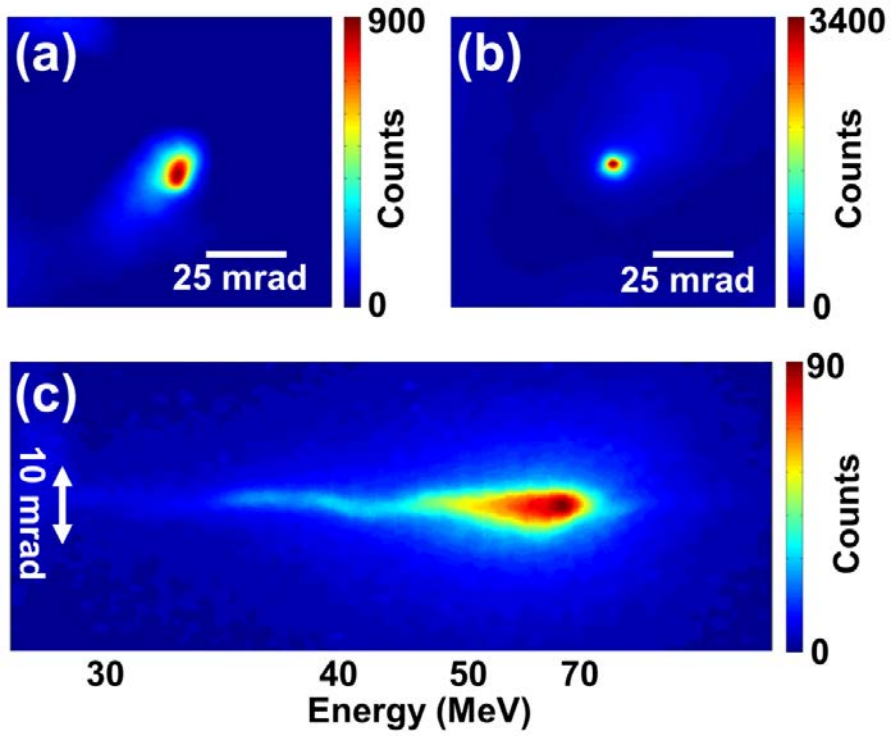

Figure 5.5. Electron signals from the Lanex screen without the deflecting 0.5T magnet generated from (a) the N^{5+} flat density profile and (b) the N^{5+} channel. (c) Energy spectrum an electron beam generated in the N^{5+} channel.

The difference in the wakefield amplitude between the flat and parabolic plasma profiles is also manifested in the quality and stability of the electron beams produced using each profile. Figure 5.5(a) shows an electron beam profile from the flat plasma, and Fig. 5.5(b) shows an electron beam profile from the plasma channel. Total integrated charge in the collimated beams for both cases is ~8 pC. However, the electron beam from the plasma waveguide is more tightly collimated with a 2.8mrad divergence on average compared to 6.6mrad from the flat profile plasma. This supports our conclusion that a stronger wake is driven in the plasma channel compared to the flat plasma profile because in general higher energy electrons are observed to be better collimated given the same injection dynamics [91].

Improved confinement of the laser pulse energy in the plasma channel also improved the electron beam pointing stability over many shots. The electron beams from the plasma waveguide show 12mrad standard deviation of the beam pointing, whereas the pointing stability from the plasma without a guiding structure is ~42mrad. Due to the unstable beam pointing from the flat plasma channel, we were not able to measure the electron energy. However, the electron energy spectrum from the N^{5+} plasma waveguide is measured and shown in Fig. 5.5(c). A quasi-mono-energetic peak was observed at 65MeV on average with the low energy tail extending down to 32MeV. The low energy tail is commonly observed in ionization injection schemes due to continuous injection of ionized electrons throughout the acceleration process [33-37].

5.5 Simulation of wakefield acceleration in a nitrogen plasma channel

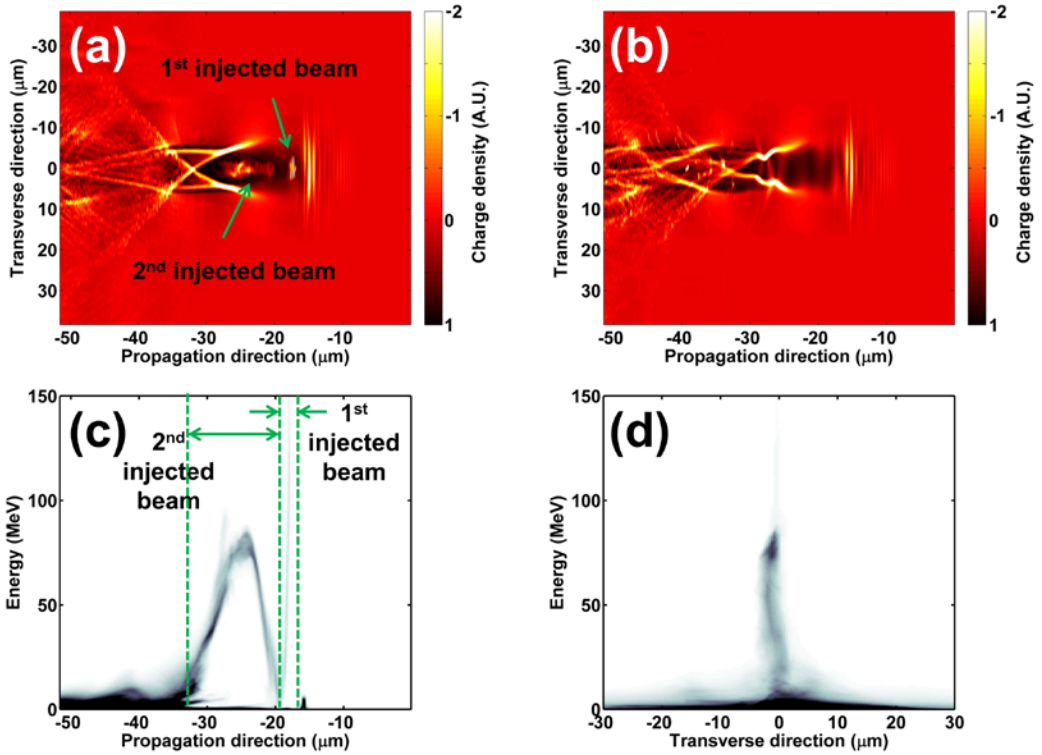

Figure 5.6. Charge density plots in a moving window after 1.4mm propagation in (a) a He-like nitrogen plasma channel showing two trapped electron beams and (b) a pure hydrogen plasma waveguide showing no trapped electrons. Features inside the first wake are untrapped background electrons. (c) Longitudinal (integrated over the transverse directions) and (d) transverse (integrated over the longitudinal direction) phase space plots of the ionized electrons ionized from N^{5+} and N^{6+} in the N^{5+} channel after 1.4mm propagation..

To gain insight into the trapping and acceleration processes in the N5+ plasma channel, we used TurboWAVE [62], which includes an ADK ionization model [92], to conduct 3D Particle-In-Cell (PIC) simulations using experimentally measured laser and channel parameters. Simulations were performed for i) a helium-like nitrogen plasma channel and ii) a pre-ionized hydrogen channel with the same electron density profile as i) to compare the effect of ionization of N^{5+} ions in the channel on accelerated relativistic electron beams. A laser pulse of peak intensity

$3.3\times10^{18}\,W/cm^2$, pulse length of 40fs FWHM, and a $14\mu m$ beam waist was guided in both plasma channels. The simulated channels had an initial $700\mu m$ long linear density ramp with on axis densities rising from $8\times10^{18}cm^{-3}$ to $1.4\times10^{19}cm^{-3}$, followed by a $100\mu m$ plateau region, and then a $700\mu m$ linear down ramp decreasing from $1.4\times10^{19}cm^{-3}$ to $8\times10^{18}cm^{-3}$. At either end of the channel short $50\mu m$ ramps brought the plasma density to vacuum. The total charge was neutralized by distributing N^{5+} or H^{+} ions within the channel.

Electron beams similar to those observed experimentally were produced from the simulated helium-like nitrogen plasma channel. A mono-energetic peak appears at 80MeV with a long low energy tail, as can be seen in the phase space plots Fig. 5.6(c) and (d). We can see the trapped electrons inside the bucket in Fig. 5.6(a), which shows a charge density plot near the end of the N^{5+} channel. In contrast, no collimated, relativistic electron beam was produced from the simulated hydrogen channel of similar shape and density. In Fig. 5.6(b) we show that no significant number of electrons is trapped in the bucket in the hydrogen plasma channel.

Figures 5.6(a) and (c) also show that two spatially separated beams are trapped. The first beam has a lower charge (14pC) and a broad spectrum extending up to 150MeV, whereas the second beam contains much more charge (55pC) and the energy distribution has a mono-energetic peak at 80MeV. From the simulations, we observe that the second beam is trapped at the density down ramp, whereas the first beam is trapped starting from the entrance of the channel. The density down ramp in the channel helps to trap a lot of charge in a short time by expanding the plasma bucket. As a result, the mono-energetic peak appears in the spectrum. Even with the

density down ramp, the plasma wave driven by the laser pulse was not strong enough to self-trap background plasma electrons without the help of the ionization injection, and simulations showed that both beams are composed of K-shell electrons ionized near the peak of the drive laser pulse.

5.6 Conclusions

In conclusion, we have demonstrated the effectiveness of a nitrogen cluster jet as a target for ionization injection assisted laser wakefield acceleration. Plasma channels composed of purely helium-like nitrogen ions are readily formed from the interaction of a 140ps channel forming pulse with large nitrogen clusters. This is due to collisional ionization of the nitrogen atoms within the cluster at the foot of the channel forming pulse and efficient heating of the highly ionized plasma after the clusters have merged. We have shown that a channel guided drive pulse produces electron beams with improved divergence and pointing stability as compared to a drive pulse injected into flat, pre-formed helium-like nitrogen plasmas. Stronger confinement of the drive pulse within the plasma channel leads to larger amplitude, more consistent plasma wakes, resulting in improved electron beam quality. Finally, 3-D PIC simulations showed that ionization of K shell electrons from the abundant helium-like nitrogen ions was essential for trapping and acceleration of a relativistic electron beam within the plasma channel.

Chapter 6: Summary and Future work

6.1. Summary

Two electron acceleration schemes using the quasi-phasematching concept are studied in depth with theory and PIC simulations (Chapters 2 and 3). In Chapter 2, we demonstrated the direct acceleration of electrons by the axial laser field component of a radially polarized laser pulse in a corrugated plasma waveguide. The phase velocity of the on axis accelerating field is matched to the velocity of the accelerated electrons by the axial density modulations in the channel. The ponderomotive force of the radially polarized laser pulse pushes background plasma electrons towards the laser propagation axis, which deflects the accelerated electron beam. This effect can be mitigated with higher accelerated electron beam density, because the space charge of the beam pushes the channel electrons off axis. It was also shown that a ramped density profile in the corrugated plasma can reduce the threshold electron energy for trapping from $\gamma_0 = 170$ to $\gamma_0 = 20$ for a laser pulse with $a_0 = 0.1$.

In Chapter 3, the quasi-phasematching technique, enabled by the corrugated plasma waveguide, is applied to LWFA to extend the acceleration distance beyond the standard dephasing length, which is the distance limit of acceleration in a conventional LWFA. Both theory and PIC simulations show that energy gain can increase significantly over standard LWFA with weakly relativistic laser pulses.

Two different methods were developed to impose density modulation in a plasma waveguide; modulation of the channel- creating laser intensity with a ring grating [51] and modulation of the cluster flow with an array of thin ($<50\mu m$) tungsten wires [52]. In Chapter 4, we examined the dynamics of the supersonic flow of clusters through thin wires. This work showed that high fractional clusterization was essential to reducing the effect of shock waves from the wires on the cluster flow. Individual clusters interact ballistically with the wires, while residual unclustered gas acts like a fluid capable of supporting shock waves. Lastly, in Chapter 5, the laser wakefield acceleration of electrons in a N^{5+} plasma waveguide is demonstrated. We first verified that the plasma guide consists essentially of pure He-like nitrogen ions. We achieved an average 65MeV (with a maximum of 120 eV) quasi-monoenergetic electron beams with injection of 10TW laser pulses into 1.5mm long N^{5+} plasma waveguides. Comparison of electron acceleration between a channel with a transverse electron density profile capable of guiding a laser pulse and a flat profile revealed that the guiding structure is essential to drive stronger wakefields over longer distances, which results in a highly collimated electron beam with stable pointing. 3D PIC simulations showed that ionization injection from N^{5+} and N^{6+} ions is critical to produce high quality electron beams. Ionization injection assisted LWFA can be used as a seed electron source to realize the QPM-DLA and QPM-LWFA schemes described in chapters 2 and 3.

6.2 Future work

Self-consistent PIC simulations of QPM-DLA and QPM-LWFA confirm the feasibility of these schemes to provide effective acceleration with relatively low power laser pulses. To experimentally demonstrate these schemes, it is essential to have a source of seed electrons of energy >~5MeV and a modulated plasma waveguide with tunable periodicity to match the phase velocity of the acceleration field (either the DLA field or the LWFA field) to the electron velocity. A possible seed electron source was discussed in chapter 5. However, more investigation is required to produce more stable electron beams in terms of energy and charge to be used as a seed electron source. For stable generation of higher energy electron beams, ionization injection assisted LWFA in a N^{5+} plasma waveguide should be done in a lower density plasma channel (~ a few 10^{18} cm^{-3}) over a longer distance (>5mm) to minimize nonlinear laser pulse evolution, since the laser pulse evolution is subject to vary significantly with small changes in experimental parameters resulting in unstable electron generation.

While the wire-modulated plasma waveguide is a convenient way to impose axial density modulations, it is difficult to dynamically move the wires to finely control the modulation period . However, a Spatial Light Modulator (SLM), which can programmably modify the intensity profile of a channel generating laser pulse, can be a much more precise and convenient technique to control the density profile of a plasma waveguide. We have recently demonstrated generation of plasma waveguides of variable axial modulation period using an SLM [G. Hine *et al*, in preparation] and we are gearing up to propagate relativistic intensity pulses in these guides.

By integrating a stable seed electron source and a a precisely controlled corrugated plasma waveguide, we will come closer to realization of the quasi-phasematched acceleration schemes described in this dissertation.

Bibliography

[1] S. Humphries Jr., *Principles of Charged Particle Accelerator* (John Wiley & Sons, New York, 1986).

[2] E. Persico, E. Ferrari, and S. E. Segre, *Principles of Particle Accelerators* (W. A. Benjamin, inc., New York, 1968).

[3] G. Ising, "Prinzip einer Methode zur Herstellung von Kanalstrahlen hoher Voltzahl," Arkiv för matematik, astronomi och fysik **18**, 1 (1924).

[4] R. Wideröe, "Über ein neues Prinzip zur Herstellung hoher Spannungen," Arch. für Elektrotechnik, **21** 387 (1928).

[5] G. A. Loew, "Elementary principles of linear accelerators,", SLAC-PUB-3221 (1983)

[6] G. A. Mourou, "Optics in the relativistic regime", Rev. Mod. Phys. **78**, 209 (2006).

[7] A. L. Schawlow and C. H. Townes, "Infrared and Optical Masers", Phys. Rev. **112**, 1940 (1958).

[8] F. J. McClung and R. W. Hellwarth, "Giant optical pulsations from ruby", J. of Appl. Phys. **33**, 828 (1962).

[9] H. A. Haus, "Mode-locking of lasers," IEEE J. of Quant. Elect. **6**, 1173 (2000).

[10] P. Maine, D. Strickland, P. Bado, M. Pessot, and G. Mourou, "Generation of ultrahigh peak power pulses by chirped pulse amplication," IEEE J. of Quant. Elect. **24**, 398 (1988).

[11] J. H. Sung, S. K. Lee, T. J. Yu, T. M. Jeong, and J. Lee, “0.1 Hz 1.0 PW Ti:sapphire laser,” Opt. Lett. **35**, 3021 (2010).

[12] C. Mainfray and C. Manus, “Multiphoton ionization of atoms,” Rep. Prog. Phys. **54**, 1333 (1991).

[13] L .V. Keldysh, “Ionization in the field of a strong electromagnetic wave,” Soviet Phys. JETP **20**, 1307 (1965).

[14] S. Augst, D. Strickland, D. D. Meyerhofer, S. L. Chin, and J. H. Eberly, “Tunneling ionization of noble gases in a high-intensity laser field,” Phys. Rev. Lett. **63**, 2212 (1989).

[15] R. R. Freeman and P. H. Bucksbaum, “Investigation of above-threshold ionization using subpicosecond laser pulse,” J. of Phys. B **24**, 325 (1991).

[16] P. Gibbon, *Short Pulse Laser Interaction with Matter* (Imperial College Press, London, 2005).

[17] P. Drude, “ZurElektronentheorie der metalle," Annalen der Physik **306**, 566 (1900).

[18] R. C. Gray, “The Rev. John Kerr, F.R.S., Inventor of the Kerr Cell,” Nature **136**, 245 (1935).

[19] P. Sprangle, C. Tang, and E. Esarey, “Relativistic Self-Focusing of Short-Pulse Radiation Beams in Plasmas,” IEEE Trans. Plasma Sci., **15**, 145 (1987).

[20] T. Tajima and J. M. Dawson, “Laser Electron Accelerator,” Phys. Rev. Lett. **43**, 267 (1979).

[21] E. Esarey and M. Pilloff, “Trapping and acceleration in nonlinear plasma waves,” Phys. of Plasmas **2**, 1432 (1995).

[22] E. Esarey, C. Schroeder, and W. Leemans, “Physics of laser-driven plasma-based electron accelerators,” Rev. Mod. Phys. **81**, 1229 (2009)

[23] V. Malka, J. Faure, Y. Gauduel, E. Lefebvre, A. Rousse, and K. T. Phuoc, “Principles and applications of compact laser-plasma accelerators,” Nature Phys. **4**, 447 (2008).

[24] P. Sprangle, E. Esarey, A. Ting, and G. Joyce, “Laser wakefield acceleration and relativistic optical guiding,” Appl. Phys. Lett. **53**, 2146 (1988).

[25] J. Schreiber, C. Bellei, S. P. D. Mangles, C. Kamperidis, S. Kneip, S. R. Nagel, C. A. J. Palmer, P. P. Rajeev, M. J. V. Streeter, and Z. Najmudin, “Complete Temporal Characterization of Asymmetric Pulse Compression in a Laser Wakefield,” Phys. Rev. Lett. **105**, 235003 (2010).

[26] E. Esarey, R. Hubbard, and W. Leemans, “Electron injection into plasma wakefields by colliding laser pulses,” Phys. Rev. Lett. **79**, 2682 (1997).

[27] J. Faure, C. Rechatin, A. Norlin, A. Lifschitz, Y. Glinec, and V. Malka, “Controlled injection and acceleration of electrons in plasma wakefields by colliding laser pulses,” Nature **444**, 737 (2006).

[28] T. Clark and H. Milchberg, “Optical mode structure of the plasma waveguide,” Phys. Rev. E. **61**, 1954 (2000).

[29] R. Lehe, A. F. Lifschitz, X. Davoine, C. Thaury, and V. Malka, “Optical Transverse Injection in Laser-Plasma Acceleration,” Phys. Rev. Lett. **111**, 085005 (2013).

[30] C. Geddes, K. Nakamura, and G. Plateau, “Plasma-density-gradient injection of low absolute-momentum-spread electron bunches,” Phys. Rev. Lett. **100**, 215004 (2008).

[31] R. M. G. Trines, R. Bingham, Z. Najmudin, S. Mangles, L. O. Silva, R. Fonseca, and P. Norreys, “Electron trapping and acceleration on a downward density ramp: a two-stage approach,” New J. Phys. **12**, 045027 (2010).

[32] A. J. Gonsalves, K. Nakamura, C. Lin, D. Panasenko, S. Shiraishi, T. Sokollik, C. Benedetti, C. B. Schroeder, C. G. R. Geddes, J. van Tilborg, J. Osterhoff, E. Esarey, C. Toth, and W. P. Leemans, “Tunable laser plasma accelerator based on longitudinal density tailoring,” Nature Phys. **7**, 862 (2011).

[33] A. Pak, K. A. Marsh, S. F. Martins, W. Lu, W. B. Mori, and C. Joshi, “Injection and Trapping of Tunnel-Ionized Electrons into Laser-Produced Wakes,” Phys. Rev. Lett. **104**, 025003 (2010).

[34] C. McGuffey, A. G. R. Thomas, W. Schumaker, T. Matsuoka, V. Chvykov, F. J. Dollar, G. Kalintchenko, V. Yanovsky, a. Maksimchuk, K. Krushelnick, V. Y. Bychenkov, I. V. Glazyrin, and A. V. Karpeev, “Ionization Induced Trapping in a Laser Wakefield Accelerator,” Phys. Rev. Lett. **104**, 025004 (2010).

[35] C. E. Clayton, J. E. Ralph, F. Albert, R. A. Fonseca, S. H. Glenzer, C. Joshi, W. Lu, K. a. Marsh, S. F. Martins, W. B. Mori, A. Pak, F. S. Tsung, B. B. Pollock, J. S. Ross, L. O. Silva, and D. H. Froula, “Self-Guided Laser Wakefield Acceleration beyond 1 GeV Using Ionization-Induced Injection,” Phys. Rev. Lett. **105**, 105003 (2010).

[36] M. Z. Mo, A. Ali, S. Fourmaux, P. Lassonde, J. C. Kieffer, and R. Fedosejevs, "Generation of 500 MeV–1 GeV energy electrons from laser wakefield acceleration via ionization induced injection using CO_2 mixed in He," Appl. Phys. Lett. **102**, 134102 (2013).

[37] Y.-C. Ho, T.-S. Hung, C.-P. Yen, S.-Y. Chen, H.-H. Chu, J.-Y. Lin, J. Wang, and M.-C. Chou, "Enhancement of injection and acceleration of electrons in a laser wakefield accelerator by using an argon-doped hydrogen gas jet and optically preformed plasma waveguide," Phys. Plasmas, **18**, 063102 (2011).

[38] W. Lu, M. Tzoufras, C. Joshi, F. Tsung, W. Mori, J. Vieira, R. Fonseca, and L. Silva, "Generating multi-GeV electron bunches using single stage laser wakefield acceleration in a 3D nonlinear regime," Phys. Rev. Spec. Top.-Accel. Beams **10**, 061301 (2007).

[39] J. E. Ralph, K. A. Marsh, A. E. Pak, W. Lu, C. E. Clayton, F. Fang, W. B. Mori, and C. Joshi, "Self-Guiding of Ultrashort, Relativistically Intense Laser Pulses through Underdense Plasmas in the Blowout Regime," Phys. Rev. Lett. **102**, 175003 (2009)

[40] X. Wang, R. Zgadzaj, N. Fazel, Z. Li, S. a. Yi, X. Zhang, W. Henderson, Y.-Y. Chang, R. Korzekwa, H.-E. Tsai, C.-H. Pai, H. Quevedo, G. Dyer, E. Gaul, M. Martinez, a. C. Bernstein, T. Borger, M. Spinks, M. Donovan, V. Khudik, G. Shvets, T. Ditmire, and M. C. Downer, "Quasi-monoenergetic laser-plasma acceleration of electrons to 2 GeV," Nature Commun. **4**, 1988 (2013).

[41] H. T. Kim, K. H. Pae, H. J. Cha, I. J. Kim, T. J. Yu, J. H. Sung, S. K. Lee, T. M. Jeong, and J. Lee, "Enhancement of electron energy to the multi-GeV regime by a

dual-stage laser-wakefield accelerator pumped by petawatt laser pulses.," Phys. Rev. Lett. **111**, 165002 (2013).

[42] C. Geddes, C. Toth, and J. Van Tilborg, "High-quality electron beams from a laser wakefield accelerator using plasma-channel guiding," Nature **431**, 538 (2004).

[43] C. G. Durfee and H. M. Milchberg, "Light Pipe for High Intensity Laser Pulses," Phys. Rev. Lett. **71**, 2049 (1993).

[44] F. S. Tsung, Ritesh Narang, W. B. Mori, C. Joshi, R. A. Fonseca, and L. O. Silva, "Near-GeV-Energy Laser-Wakefield Acceleration of Self-Injected Electrons in a Centimeter-Scale Plasma Channel," Phys. Rev. Lett. **93**, 185002 (2004).

[45] W. P. Leemans, B. Nagler, A. J. Gonsalves, C. Tóth, K. Nakamura, C. G. R. Geddes, E. Esarey, C. B. Schroeder, and S. M. Hooker, "GeV electron beams from a centimetre-scale accelerator," Nature Phys. **2**, 696 (2006).

[46] W. D. Kimura, G. H. Kim, R. D. Romea, L. C. Steinhauer, I. V. Pogorelsky, K. P. Kusche, R.C. Fernow, X. Wang, and Y. Liu, "Laser Acceleration of Relativistic Electrons Using the Inverse Cherenkov Effect," Phys. Rev. Lett. **74**, 546 (1995).

[47] T. Plettner, R. L. Byer, E. Colby, B. Cowan, C. M. S. Sears, J. E. Spencer, and R. H. Siemann, "Visible-Laser Acceleration of Relativistic Electrons in a Semi-Infinite Vacuum," Phys. Rev. Lett. **95**, 134801 (2005).

[48] E. Esarey, P. Sprangle, and J. Krall, "Laser acceleration of electrons in vacuum," Phys. Rev. E **52**, 5443 (1995).

[49] B. Hafizi, A. Ting, E. Esarey, P. Sprangle, and J. Krall, "Vacuum beat wave acceleration," Phys. Rev. E **55**, 5924 (1997).

[50] A. G. York, H. M. Milchberg, J. P. Palastro, and T. M. Antonsen, "Direct Acceleration of Electrons in a Corrugated Plasma Waveguide," Phys. Rev. Lett. **100**, 195001 (2008).

[51] B. D. Layer, A. York, T. M. Antonsen, S. Varma, Y.-H. Chen, and H. M. Milchberg, "Ultrahigh-Intensity Optical Slow-Wave Structure," Phys. Rev. Lett. **99**, 035001 (2007).

[52] B. D. Layer, A. G. York, S. Varma, Y.-H. Chen, and H. M. Milchberg, "Periodic index-modulated plasma waveguide," Opt. Express **17**, 4263 (2009).

[53] O. F. Hagena and W. Obert, "Cluster Formation in Expanding Supersonic Jets: Effect of Pressure, Temperature, Nozzle Size and Test Gas," J. Chem. Phys. **56**, 1793 (1972).

[54] H. Sheng, K. Kim, V. Kumarappan, B. Layer, and H. Milchberg, "Plasma waveguides efficiently generated by Bessel beams in elongated cluster gas jets," Phys. Rev. E **72**, 036411 (2005).

[55] M. M. Fejer, G. A. Magel, D. H. Jundt, and R. L. Byer, "Quasi-phase-matched second harmonic generation: tuning and tolerances," IEEE J. of Quant. Elect. **28**, 2631 (1992).

[56] J. P. Palastro, T. M. Antonsen, S. Morshed, A. G. York, H. M. Milchberg, " Pulse propagation and electron acceleration in a corrugated plasma channel," Phys. Rev. E **77**, 036405 (2008).

[57] J. P. Palastro, T. M. Antonsen, “Interaction of an ultrashort laser pulse and relativistic electron beam in a corrugated plasma channel,“ Phys. Rev. E **80**, 016409 (2009).

[58] C. K.Birdsall and A. B. Langdon, *Plasma Physics via Computer Simulation* (McGraw-Hill, New York, 1985).

[59] O. Buneman, “Dissipation of currents in ionized media,” Phys. Rev, **115**, 503 (1959).

[60] J. M. Dawson, “One-dimensional plasma model,” Phys. of Fluids **5**, 445 (1962).

[61] R. W. Hockney and J. W. Eastwood, *Computer Simulation Using Particles* (McGraw-Hill, New York, 1981).

[62] D. F. Gordon, “Improved Ponderomotive Guiding Center Algorithm,” IEEE Trans. Plasma Sci., **35**, 1486 (2007).

[63] J. M. Dawson, “Particle simulation of plasmas,” Rev. Mod. Phys. **55**, 403 (1983).

[64] J. Verboncoeur, “Particle simulation of plasmas: review and advances,” Plasma Phys. and Control. Fusion **47**, A231 (2005).

[65] V. Vahedi and M. Surendra, “Monte Carlo collision model for particle-in-cell method: Application to argon and oxygen discharges,” Comp. Phys. Comm. **87**, 179 (1995).

[66] R.Courant,K.Friedrichs, and H. Lewy, “Über die partiellen Differenzengleichungen der Mathematischen Physik,” Mathematische Annalen **100**, 32 (1928).

[67] J. Denavit, “Numerical Simulations of Plasmas with Periodic Smoothing in Phase Space,” J. of Comp. Phys. **9**, 75 (1972).

[68] P. Serafim, P. Sprangle, and B. Hafizi, “Optical guiding of a radially polarized laser beam for inverse Cherenkov acceleration in a plasma channel,” IEEE Trans. Plasma Sci. **28**, 1155 (2000).

[69] H. M. Milchberg, T. R. Clark, C. G. Durfee III, T. M. Antonsen Jr., and P. Mora, “Development and applications of a plasma waveguide for intense laser pulses,” Phys. Plasmas **3**, 2149 (1996).

[70] H. M. Milchberg, C. G. Durfee III, and T. J McIlrath, “High-Order Frequency Conversion in the Plasma Waveguide,” Phys. Rev. Lett **75**, 2494 (1995).

[71] J. D. Lawson, “Lasers and Accelerators,” IEEE Trans. Nucl. Sci. **26**, 4217 (1979); P. M. Woodward, “A method of calculating the field over a plane,” J. Inst. Electr. Eng. **93**, 1554 (1947).

[72] K. S. Yee, “Numerical Solution of Initial Boundary Value Problems Involving Maxwell's Equations in Isotropic Media,” IEEE Trans. Ant. Prop. **14**, 302 (1966).

[73] W. Zhu, J. P. Palastro and T. M. Antonsen, “Pulsed mid-infrared radiation from spectral broadening in laser wakefield simulations,” Phys. Plasmas **20**, 073103 (2013).

[74] C. B. Schroeder, E. Esarey, B. A. Shadwick and W. P. Leemans, “Trapping, dark current, and wave breaking in nonlinear plasma waves,” Phys. Plasmas **13**, 033103 (2006).

[75] S. J. Yoon, J. P. Palastro, D. Gordon, T. M. Antonsen, and H. M. Milchberg, "Quasi-phase-matched acceleration of electrons in a corrugated plasma channel," Phys. Rev. ST Accel. Beams **15**, 081305 (2012).

[76] P. Sprangle, J. R. Peñano, B. Hafizi, R. F. Hubbard, A. Ting, D. F. Gordon, A. Zigler and T. M. Antonsen Jr., "GeV acceleration in tapered plasma channels," Phys. Plasmas **9**, 2364 (2002).

[77] D.H. Froula, C. E. Clayton, T. Döppner, K. A. Marsh, C. P. J. Barty, L. Divol, R. A. Fonseca, S. H. Glenzer, C. Joshi, W. Lu, S. F. Martins, P. Michel, W. B. Mori, J. P. Palastro, B. B. Pollock, A. Pak, J. E. Ralph, J. S. Ross, C. W. Siders, L. O. Silva, and T. Wang, "Measurements of the Critical Power for Self-Injection of Electrons in a Laser Wakefield Accelerator," Phys. Rev. Lett. **103**, 215006 (2009).

[78] A. Ting, D. Gordon, M. Helle, D. Kaganovich, P. Sprangle, and B. Hafizi, "Plasma Density Tapering for Laser Wakefield Acceleration of Electrons and Protons," AIP Conf. Proc. **1299**, 203 (2010).

[79] C. Benedetti, C. B. Schroeder, E. Esarey and W. P. Leemans., "Quasi-matched propagation of ultra-short, intense laser pulses in plasma channels," Phys. Plasmas **19**, 053101 (2012).

[80] V. Kumarappan, K.Y. Kim, and H.M. Milchberg, "Guiding of Intense Laser Pulses in Plasma Waveguides Produced from Efficient, Femtosecond End-Pumped Heating of Clustered Gases," Phys. Rev. Lett. **94**, 205004 (2005).

[81] T.-S. Hung, Y.-C, Ho, Y.-L. Chang, S.-J. Wong, H.-H. Chu, J.-Y. Lin, J. Wang, and S.-Y. Chen, "Programmably structured plasma waveguide for development of table-top and photon and particle sources," Phys. Plasma **19**, 063109 (2012).

[82] K. Y. Kim, V. Kumarappan, and H. M. Milchberg, "Measurement of the average size and density of clusters in a gas jet," Appl. Phys. Lett. **83**, 3210 (2003).

[83] Ya. B. Zel'dovich, Yu. P. Raizer, *Physics of Shock Waves and High-Temperature Hydrodynamic Phenomena* (Dover Publications, New York,, 2002).

[84] R. S. Berry, S. A. Rice, and J. Ross, *Physical Chemistry* (Oxford Univ. Press, Oxford, 2000).

[85] H. M. Milchberg, S. J. McNaught, and E. Parra, "Plasma Hydrodynamics of the intense laser-cluster interaction," Phys. Rev. E. **64**, 056402 (2001).

[86] T. Ditmire, T. Donnelly, A. M. Rubenchick, R. W. Falcone, and M.D. Perry, "Interaction of intense laser pulse with atomic clusters," Phys. Rev. A **53**, 3379 (1996).

[87] T. R. Clark and H. M. Milchberg. "Time- and Space-Resolved Density Evolution of the Plasma Waveguide," Phys. Rev. Lett. **78**, 2373 (1997).

[88] S. Yoon, A. Goers, G. Hine, and J. Magill, "Shock formation in supersonic cluster jets and its effect on axially modulated laser-produced plasma waveguides," Opt. Exp. **21**, 15878 (2013).

[89] A. Buck, K. Zeil, A. Popp, K. Schmid, A. Jochmann, S. D. Kraft, B. Hidding, T. Kudyakov, C. M. S. Sears, L. Veisz, S. Karsch, J. Pawelke, R. Sauerbrey, T. Cowan, F. Krausz, and U. Schramm, "Absolute charge calibration of scintillating screens for relativistic electron detection.," Rev. Sci. Instrum. **81**, 033301 (2010).

[90] S. Shiraishi, C. Benedetti, A. J. Gonsalves, K. Nakamura, B. H. Shaw, T. Sokollik, J. van Tilborg, C. G. R. Geddes, C. B. Schroeder, C. Tóth, E. Esarey, and W. P. Leemans, “Laser red shifting based characterization of wakefield excitation in a laser-plasma accelerator,” Phys. Plasmas **20**, 063103 (2013).

[91] V. Malka, S. Fritzler, E. Lefebvre, M.-M. Aleonard, F. Burgy, J.-P. Chambaret, J.-F. Chemin, K. Krushelnick, G. Malka, S. P. D. Mangles, Z. Najmudin, M. Pittman, J.-P. Rousseau, J.-N. Scheurer, B. Walton, and a E. Dangor, “Electron acceleration by a wake field forced by an intense ultrashort laser pulse.,” Science **298**, 1596 (2002).

[92] M. V Ammosov, N. B. Delone, and V. P. Krainov, “Tunnel ionization of complex atoms and of atomic ions in an alternating electromagnetic field,” Sov. Physi. JETP **64**, 1191 (1986).

[93] G. Hine, A. Goers, S. J. Yoon, J. Elle, and H. M. Milchberg, in prepagation